Insights into Low-Dimensional Many-Body Localised Systems

Christian Putra Chen

The Department of Physics, Lancaster University

The School of Chemistry, the University of Manchester

A dissertation submitted for the degree of Doctor of Philosophy

at Lancaster University and the University of Manchester

Lancaster University

MANCHESTER 1824
The University of Manchester

December 2021

"In all chaos there is a cosmos,

in all disorder a secret order."

— *Carl Gustav Jung*

Foreword

This thesis describes work carried out between April 2017 and March 2022 in the Condensed Matter Theory group at the Department of Physics, Lancaster University, in association with the Graphene NOWNANO Centre for Doctoral Training based in the University of Manchester, under the supervision of Prof. Henning Schomerus. The following sections of this thesis are included in work that has been published, is submitted or to be submitted:

Chapter 2: C. P. Chen and H. Schomerus, "Fock-space geometry and strong correlations in many-body localised systems", Phys. Rev. B **104**, 205411 (2021).

Chapter 3: C. P. Chen, M. Szyniszewski and H. Schomerus, "Many-body localisation of zero modes", Phys. Rev. Research **2**, 023118 (2020).

Chapter 4: C. P. Chen, "Approximating Entanglement Transitions with Random-Matrix Models" (unpublished). Inspired particularly by the random-matrix model proposed in [1].

This thesis is my own work and contains nothing which is the outcome of work done in collaboration with others, except as specified in the text and Acknowledgements. This thesis has not been submitted in substantially the same form for the award of a higher degree elsewhere. All the relevant permissions have been obtained concerning reuse of material from previously published work. This thesis does not exceed the word limit of 80 000 words.

Christian Putra Chen

Lancaster, March 2022

Abstract

We study the strange nature of low-dimensional quantum systems in the presence of disorder, with a particular focus on a broad class of closed quantum system that fails to equilibrate under its own dynamics; so-called many-body localised systems. These systems comprise particles that are subject to disorder—usually introduced via an inhomogeneous magnetic field—which localise in real space as disorder passes a critical threshold. The transition into this localised regime is characterised by the spontaneous emergence of an extensive set of local conserved quantities, leading to the notion of emergent integrability.

It is precisely the nature of these conserved quantities that we tackle first. The emergence of these conserved quantities is mathematically undeniable; however, there still lies the question of what form these conserved quantities take, and moreover, how should they be constructed? In the literature, attempts to construct conserved quantities via perturbative methods are common; and rightfully so, as it is natural to attempt to extend the notion of single-particle Anderson localisation—which has been analytically solved—to the many-body regime. This involves "dressing" the single-particle operators of the non-interacting case with extra terms, thus creating a complete single-quasiparticle basis of the interacting system. Despite the convenience, however, such perturbative constructions depend upon assumptions that are not necessarily guaranteed. We attack these assumptions directly, and show—both analytically and numerically—that conserved quantities are distinctly nonperturbative in a paradigmatic model of many-body localisation.

Next, we consider the effect of global symmetries on the nature of many-body localisation; in particular, chiral symmetry. By definition, chiral symmetry produces a eigenspectrum that is symmetrical about zero, thus "pairing" each eigenstate with another of mirrored eigenenergy; however, that is only true if there exists an even number of eigenstates—what of an odd number? It is this question that motivates our use of spin-1 particles, as their odd number of spin-degrees of freedom produce a many-body

Hilbert space that is, by necessity, odd-dimensioned. The joint constraints of chiral symmetry and an odd number of eigenstates produce at least one state that is pinned to zero eigenenergy—a zero mode robust to all parameter variation. We explore the phenomenology of this zero mode in the context of many-body localisation, and find that it possesses fragmented correlations that clearly distinguish it from nonzero modes that localise in a more typical fashion.

Finally, we conclude this work with an initial study into the nature of entanglement transitions in general, via the consideration of new, more-recent models. A well-known consequence of the emergent integrability central to many-body localised systems is a stark shift in the entanglement of eigenstates. Whereas, in the ergodic regime, entanglement spreads ballistically and scales extensively with the volume of the system—a so-called volume law—the localised regime is characterised by entanglement that spreads logarithmically, with a subextensive area-law scaling. This area-law scaling is not unique to many-body localised systems, as we also see it emerge in quantum circuit models with "brick-layer" structure. We compare these two different types of entanglement transition directly using entropy-like quantities, and attempt to map their behaviour onto random-matrix models (that are more easily understood from an analytical standpoint).

Acknowledgements

This work would have proved impossible without the support of many people. Chief amongst them is my supervisor Henning Schomerus, who I would like to especially thank for sharing his immense knowledge and experience with me over the course of the last few years. His advice always proved invaluable, and his understanding and patience throughout my recovery from surgery—and more recently, during the pandemic—were blessings that I am deeply grateful for. His guidance was, without a doubt, crucial to the success of this work.

I would also like to thank my fellow colleague Marcin Szyniszewski—who has now moved on from Lancaster—for our endless discussions about physics, and for his extreme willingness to share the specifics of his knowledge with me; I could not have asked for a better collaborator for my first publication. Thanks to Jens Bardarson and Fabian Heidrich-Meisner for brief, albeit valuable, discussions, and also the entire condensed matter theory group at the Physics Department of Lancaster University. Finally, I must also offer the warmest thanks to my guiding light, Saffron Baldoza, my parents, as well as my dearest friends Ally Thomsen, Chris Pain, and David Anthony for always being there for me, and reminding me that this was all worth it.

This research was funded by UK Engineering and Physical Sciences Research Council (EPSRC) via Grant Nos. EP/P010180/1 and EP/L01548X/1. Computer time was provided by Lancaster University's High-End Computing facility.

Table of Contents

Introduction

Many-body localisation is a curious phenomenon that occurs in a broad class of closed many-body quantum systems. These systems start failing to equilibrate under their own dynamics as a consequence of increasing disorder past a threshold point [2–7]. It is an extension of Anderson localisation [8] into interacting systems, and thus shares many of its unique properties—properties such as zero direct-current conductivity, a discrete local eigenspectrum [6, 9–11], and eigenstates with a so-called area-law entanglement [5, 6]. All of these properties can be thought of as specific instances of a general phenomenon: localised systems exhibit some memory of their initial conditions, which are preserved in local observables at long—theoretically infinite—times. So what are the key differences between the noninteracting and interacting case? Whereas the noninteracting case trivially has no spreading of entanglement, alongside zero dephasing and dissipation, the introduction of interactions produces, instead, a logarithmic spreading of entanglement and finite dephasing (zero dissipation remains). Overall, both forms of localisation share many similarities, and starkly differ from the, more common, thermal regime with its definitive erasure of initial conditions [2, 4, 12].

Anderson localisation has been well-studied since the mid-20th century; however, research on many-body localisation has had a comparatively recent debut. This is a direct result of the vast, exponential increase in computational power we have been privy to in the last few decades, which was necessary to match the exponentially increasing complexity of many-body quantum systems when interactions become finite. These unique properties ultimately stem from a violation of the eigenstate thermalisation hypothesis [13, 14]—a quantum analogue to the thermalisation we see in the majority of classical interacting systems. This violation implies a lack of thermalisation, which means that these systems fail to equilibrate under their own dynamics, even in the limit of infinite temperature. It is perhaps of little surprise, then, that this nonequilibrity would render null the naive

assumptions that one would usually be tempted to make.

In particular, we should note a theoretically rich consequence of the many-body localisation transition—namely, the spontaneous emergence of a complete set of extensive, conserved quantities [15–21]. Such conserved quantities can be thought of as constants of motion which encapsulate the full dynamical behaviour of a system, and lead to the notion of emergent integrability [15–18]. It is not hard to see why construction of these quantities is highly sought after, but there still lies the question of how to obtain them in practice. Since they are easily constructed in the noninteracting case of Anderson localisation, it is quite natural to utilise perturbation theory to adiabatically extend them into the regime of finite interactions. However, what seems natural does not always align with reality, and we should check our assumptions thoroughly. This is the key premise of chapter 2, which yields solution via the consideration of Brueckner orbitals [22–24]—a never-before utilised technique in the context of many-body localisation (despite its prevalence in quantum chemistry).

Next, we consider that the aforementioned set of conserved quantities map bijectively onto a set of single-particle orbitals which are accessible via numerical methods. How exactly should we define these orbitals? In the case of fermionic many-body systems, we have the well-studied one-particle density matrix [25–35]—the eigenstates form an orthogonal basis of so-called natural orbitals, from which we can (in theory) construct the many-body eigenstates of our full system. The truth of this statement is linked directly to the validity of perturbative methods in constructing the conserved quantities, and thus is also addressed in chapter 2. However, the issue of what to do with non-fermionic systems still remains. Thankfully, one can map any spin-1/2 system directly onto a system of spinless fermions via Jordan-Wigner transformation; but what of higher-spin systems—is there an analogue to the one-particle density matrix in this context? This question is addressed, amongst other things, in chapter 3.

It is also of interest to consider the effects of global symmetries on the nature of many-body localisation; in particular, chapter 3 considers the effect of chiral symmetry on a system of spin-1 particles. The reason we consider spin-1—and not spin-1/2—particles is due to the joint effect of chiral symmetry combined with an odd-dimensioned Hilbert space. In combination, these two properties necessarily produce at least one eigenenergy that is pinned to zero, regardless of parameter variation. This allows us to explore

the nature of many-body localisation in the context of zero modes; a largely unstudied premise until recently. We characterise the nature of the transition—both numerically and analytically—through the use of density-matrix-like correlators that aim to provide a single-particle basis for systems of arbitrary spin.

To close this work, we explore the general nature of ergodicity and area-law transitions in chapter 4. We do this by comparing dynamical behaviour across four different disordered models: the random-field Heisenberg model [36, 37], a random quantum circuit model [38–41], and two variants of random matrix models (structured and unstructured) [1]. We focus on the relation between two quantities in particular—the well-established bipartite entanglement entropy, and the useful (but less-often considered) tripartite mutual information. A convenient property of these two quantities is that they are of comparable magnitude in all four models, and thus we do not need to enact any form of scaling to compare them. These comparisons are primarily motivated by the question: can we accurately approximate the dynamical properties of well-studied models with random matrix models? This is an instructive question due to our analytical knowledge of random matrix models, which may aid our understanding of entanglement transitions in general.

Finally, it would also be remiss to not make a special mention of the recent debate over the existence of a true many-body localised phase at all. This has been a lurking proposition in the field; but has only very recently come to great attention, with the publication of several notable papers on the topic. For example, there have been claims that chaos could destroy many-body localisation in the thermodynamic limit [9]; but careful analysis of [42] suggests that finite-size effects may prevent these arguments from being viable—and in the same vein—it has also been argued that so-called *avalanche instabilities* would be invisible in the system sizes accessible to us numerically [43]. There are also indications that the many-body localisation phase transition may indeed exist, but only at much higher disorder values than previously thought typical [44]—or perhaps that many-body localisation could, at least partially, belong to the Berezinskii-Kosterlitz-Thouless (BKT) universality class [45]; thus meaning that we have a slowly diverging correlation length, which usually implies that the transition is very hard to pinpoint. However, despite this active debate, the many-body localised regime, even if not a "true" phase transition, still has undeniably robust dynamical properties which are very much worth exploring.

Chapter 1

Theoretical Background

1.1 The Paradox of Quantum Thermalisation

When we say that a system thermalises, what do we precisely mean by that? For classical systems, the concept is very clearly defined; it means that a system gradually, over finite time, approaches its most entropically stable state—thermal equilibrium. In classical thermodynamics (and statistical mechanics in general), we make use of various statistical ensembles depending on what kind of system is involved; one such ensemble being the *microcanonical ensemble*. This ensemble is a specific statistical ensemble which is utilised to describe the mechanics of classical systems, with known total energy, which are assumed to be in thermal equilibrium. This ensemble hinges on the idea that all microstates with the same total energy are equally probable for systems in thermal equilibrium, and allows one to calculate an ensemble average by simply averaging over all accessible microstates—i.e. microstates with the correct total energy E. In practice, mathematically speaking, this can be done by assuming all states within a width W of a given energy E are equally likely, and then taking the limit of $W \to 0$. However, the validity of the microcanonical ensemble relies on the assumption of *ergodicity*: the idea that all accessible microstates are equally probable over arbitrarily long periods of time [46]. While the assumption of ergodicity is reasonable in classical equilibrium mechanics, due to the dynamical chaos inevitably present during equilibration, the assumption is not so reasonable when considering a quantum system; especially closed quantum systems. This is because—due to the strictly linear time evolution of the Schrödinger equation $i\hbar\frac{\mathrm{d}}{\mathrm{d}t}\left|\psi(t)\right\rangle = H\left|\psi(t)\right\rangle$—the unitary time evolution of any given quantum state lacks the presence of any clear dy-

namical chaos. From this fact, one would naively assume that thermalisation of closed quantum systems is therefore impossible; however, more recent experiments in the laboratory, involving ultracold atomic gases, have managed to reasonably approximate such "impossible" closed quantum systems. These experiments highlight that, in reality, these systems do indeed thermalise in some sense [47, 48] via a process we refer to as *quantum thermalisation*.

In an open thermalising system, the majority of information relating to initial conditions is quickly lost over time as it approaches thermal equilibrium—although, certain quantities, such as temperature and chemical potential (alongside many others), do remain realistically observable for arbitrarily long periods of time. This is because an open system thermalises via the exchange of extensive quantities, such as energy or number of particles, between the system itself and some external reservoir[1] it is coupled to. This process continues until, eventually, the system achieves a stable thermal equilibrium. The quantum description of this involves the conceptual introduction of *information*, which can be abstractly thought of as being encoded within *patterns* of observable quantities. It is therefore an umbrella term, as the exchange of any quantity, physical or potential, necessitates an exchange of information. In the context of open quantum systems, the external reservoir acts as a detector of sorts, performing random chaotic measurements on the system, and thus leading to the transfer of information from system to environment—the system loses its finite degrees of freedom to the reservoir's, essentially infinite, degrees of freedom. However, this loss of information would be impossible in a closed quantum system since, by definition, the unitary time evolution of a quantum state cannot erase information—all information regarding the initial conditions of a closed quantum system must be forever preserved within the system itself. This is the origin of the perceived paradox of quantum thermalisation; however, it is not actually a paradox, since it can be resolved without the true erasure of quantum information. In actuality, the information is not being erased, but rather, it is being "hidden". In an interacting closed quantum system, the movement of information occurs when entanglement spreads throughout the system; after long times, most of this information becomes inaccessible, since the recovery of said information would require the measurement of *global operators*, and only *local operators* can be feasibly measured and analysed. This is the process of *quantum decoher-*

[1] For thermalising systems, the terms "reservoir" and "heat bath" are typically used interchangeably.

ence. To understand why the measurement of global operators is a difficult procedure, we must first define what global and local operators are, along with a basis on which these operators can act.

States within a closed quantum system can be represented using the *density matrix* formalism—these matrices are essentially probability operators which inform us of information held within the eigenstate of a system, and take the form $\rho = \sum_j p_j \left|\psi_j\right\rangle\!\left\langle\psi_j\right|$, where p_j represents the probability of the system being prepared in state $|\psi_j\rangle$. We will henceforth refer to such operators as *density operators*. They can be considered an extension of wavefunctions and eigenstates, in that they can not only capture the dynamics of *pure states*, but also *mixed states*—states that are either prepared with unknown initial conditions, or that are subject to interentanglement with other states. If we work in the Schrödinger representation—in which quantum states evolve in time and operators are constant in time—for a given Hamiltonian H, the unitary time evolution of a density operator's initial state $\rho(0)$ is described by

$$\rho(t) = \exp\left(-i\frac{Ht}{\hbar}\right)\rho(0)\exp\left(i\frac{Ht}{\hbar}\right), \tag{1.1}$$

subject to

$$[H, \rho] = i\hbar\frac{\mathrm{d}\rho}{\mathrm{d}t}, \tag{1.2}$$

along with the basis-invariant quantity

$$\mathrm{Tr}\,(\rho) = 1. \tag{1.3}$$

Additionally, this means that all other operators $\hat{O}$ are time-independent, and produce corresponding observables O. The expectation value of such observables, at a given time t, is given by

$$\langle\hat{O}\rangle_t = \mathrm{Tr}\left\{\hat{O}\rho(t)\right\}. \tag{1.4}$$

We must also be careful when constructing these density matrices, since we must ensure that the resulting matrix is *positive semi-definite* and obeys Eq. (1.3).

Since we are considering an interacting many-body system, the dimensionality of our state space will grow exponentially with the size of the system for even small spin-degrees of freedom. Therefore, to simplify things, we will consider a system composed of N two-state subsystems which will be referred to as *spins* for the remainder of this chapter. These spin systems need not necessarily be composed of physical spin-1/2's, and are called

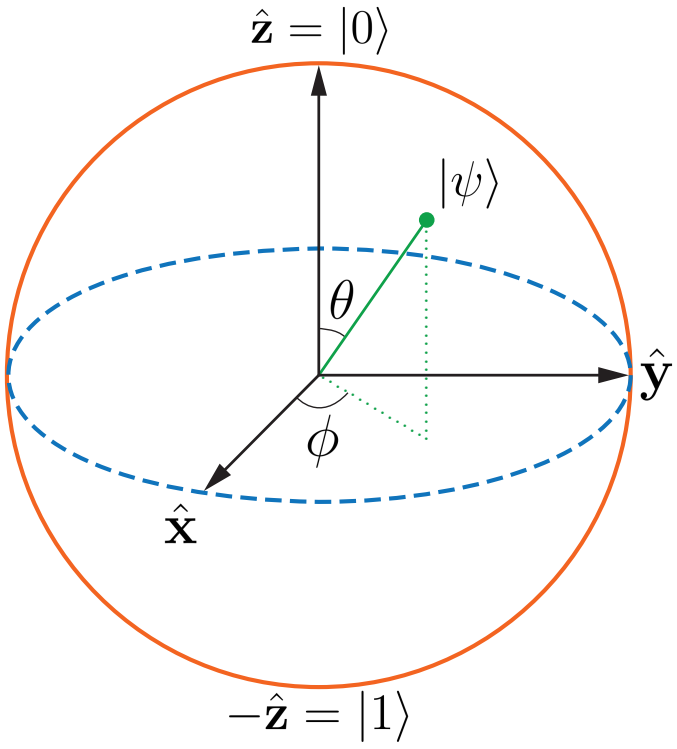

Figure 1.1: Diagram depicting the Bloch sphere for a two-state quantum system.

spins simply out of convenience. Each spin is treated as a zero-dimensional point in real space and local pure state space—each consisting of two states and all of their complex linear combinations—and can exist in one, two, or three spatial dimensions. The local pure-state space of each of these spins consists of two states and all of their complex linear combinations, which can be represented quite simply on a *Bloch sphere* (see Fig. 1.1). Since each of these spins is a two-state system, we represent each one as a two-dimensional *spinor*. Any spinor, representing a spin i, is subject to transformation by any linearly independent group of two-dimensional matrices—in particular, a convenient choice is the group of determinant-1 unitary matrices SU(2), the generators of which are the set of Pauli matrices $\{\sigma_i^x, \sigma_i^y, \sigma_i^z\}$. We henceforth denote the union of the Pauli matrices with the identity operator $\sigma_i^0 \equiv \mathbb{1}$ as the set $\{\sigma_i^a\}$. By construction, any two-dimensional Hermitian matrix can be represented as a linear combination of the $\{\sigma_i^a\}$, thus we can conveniently represent a complete basis of many-body operators (of the full system) as outer-product states of the form

$$\hat{K}_{a_1,a_2,\ldots,a_N} = \bigotimes_{i=1}^{N} \sigma_i^{a_i}; \tag{1.5}$$

the structure of which immediately implies that the full system possesses 4^N linearly

independent operators $\hat{K}_{a_1,a_2,\ldots,a_N}$, corresponding to the number of unique permutations of the set $\{a_1, a_2, \ldots, a_N\}$ given that $a_i \in \{0, x, y, z\}$. In the general case, where we consider the introduction of local spins $\{i\}$ with local Hilbert space dimension $q_i > 2$, we can surmise that each spin contributes a factor of q_i^2 to the number of operators [2].

The form of operator $\hat{K}$, as defined in Eq. (1.5), determines its classification: global, local, or "k-local". A k-local operator is one where k of the individual σ_i^a terms in Eq. (1.5) are not identity operators, and as such, only acts non-trivially on k of the N spins. If we map each of the 2^N many-body basis states onto the 2^N vertices of an N-dimensional hypercube, then we can interpret these k-local operators as representative of hoppings of length k on this hypercube—they connect vertices with $k-2$ intermediate vertices. Global and local operators are simply the most extreme limiting cases of a k-local operator—$\hat{K}$ is a global operator when k is of order N, whereas $\hat{K}$ is a local operator when k is of order one *and* the few nonidentity Pauli operators act on spins with real-space separation of order one.

Since most of the σ_i^a terms in a local operator are identity operators, and thus act trivially on the spins in our system, measuring such an operator is relatively feasible. However, conversely, we can also see why measuring a global operator—by which we retrieve all extensive conserved quantities, such as total energy or number of particles—is incredibly non-trivial, since most of the σ_i^a terms in a global operator are Pauli operators, and thus act non-trivially on the spins in our system. It is therefore reasonable to say that information "hidden" in these global operators can essentially be treated as "lost" due to quantum thermalisation—retrieving this information becomes increasingly more demanding as the many-body operators become less local.

1.2 Modelling Quantum Thermalisation

In the previous section, we explained why thermalisation in a closed quantum system is not necessarily paradoxical, provided we expand our definition of information loss. However, what exactly are the mechanics behind quantum thermalisation? The process of thermal equilibration in classical systems generically involves the exchange of extensive quantities between a system and the reservoir it is coupled to; however, there is no external reservoir to couple to in the case of a closed quantum system. We can, however, produce a model

that imitates this system-reservoir coupling. We begin by partitioning our system into two subsystems—subsystem A, the smaller of the two, and subsystem B, the environment-like complement. By modelling our system in this way, we can treat subsystem A as if it were a system coupled to an external reservoir B, thus implying that our system can, in a sense, act as its own reservoir (see Fig. 1.2). Considering the exchange of extensive quantities between subsystems A and B allows us to define a "self-temperature" for our closed system, which we will henceforth refer to simply as temperature T for brevity. The choice of subsystem A is arbitrary, and as such, the exact size or location (regardless of which space we work in) does not matter too much, as long as the degrees of freedom within A can be described by k-local operators with finite k. We also require the number of degrees of freedom in subsystem A to be negligible compared to B, but we can resolve this by adding more degrees of freedom to B in a specific way, which we now discuss.

For convenience, let us consider the case where subsystem A is a compact region in real space. In this case, the addition of degrees of freedom to our system will result in an increase in the volume of B. If we add degrees of freedom to our system that are arbitrarily far from subsystem A, we can ensure that the volume of B will increase without limit—all while also ensuring that the physical properties of A, such as its volume, remain unaltered. In addition, if we change our system's Hamiltonian in said locations—that is, arbitrarily far from A—where the degrees of freedom are being added, we can also ensure that, as we take the thermodynamic limit, we are not directly altering the thermodynamic properties of A. By repeatedly adding of degrees of freedom, while simultaneously taking the thermodynamic limit, we iteratively produce a series of larger and larger systems, each with their own Hamiltonians. We continue this process indefinitely, so that the number of degrees of freedom increases without limit (see Fig. 1.2(b)). For the initial state $\rho(t = 0)$ of each system in this iterative sequence, we need to ensure that the equilibrium expectation value of the total energy $\langle H \rangle_T$, at temperature T, is such that the energy density of the system is fixed at its equilibrium value. Note that, although we fix the energy density, the extensive energy within the system can be distributed freely. We can express the density operator of subsystem A as a *reduced density matrix* ρ_A, which is expressed as a partial trace over the full system ρ_{AB}, and takes the form

$$\rho_A(t) = \mathrm{Tr}_B\{\rho_{AB}(t)\}, \tag{1.6}$$

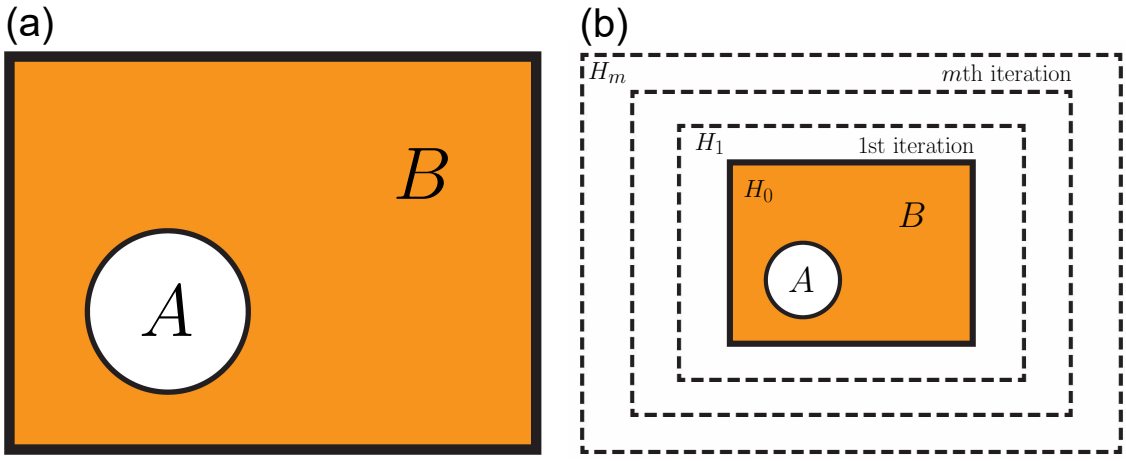

Figure 1.2: A diagram illustrating a closed quantum system partitioned into a subsystem A, and its larger, environment-like, complement B. The mechanics of quantum thermalisation are underpinned by a closed quantum system's ability to, in a sense, couple to itself and act as its own reservoir. Panel (a) depicts the initial setup, and panel (b) illustrates the iterative process of taking the infinite size limit $m \to \infty$ by adding degrees of freedom to the system, while simultaneously taking the thermodynamic limit. Each iteration of this process produces a new system (shown by the dotted lines), with a new Hamiltonian H_m. By necessity, the interactions in the Hamiltonian must "connect" all of its degrees of freedom.

where the partial trace $\mathrm{Tr}_B\{...\}$ is explicitly defined as

$$\mathrm{Tr}_B\{\rho_A \otimes \rho_B\} \equiv \rho_A \,\mathrm{Tr}\{\rho_B\}, \tag{1.7}$$

provided that ρ_{AB} can be expressed as the outer product of its subsystems ρ_A and ρ_B. If ρ_{AB} cannot be written as such an outer product, as is the case for mixed states, we can explicate the partial trace via a Schmidt decomposition, which we explain thoroughly in section 3.4.1. For the same subsystem A, that is expressed in Eq. (1.6), we can also write down an operator that is valid only for systems in equilibrium—the Boltzmann density operator

$$\rho_A^{(\mathrm{eq})}(T) = \mathrm{Tr}_B\left\{\frac{1}{Z(T)}\exp\left(-\frac{H}{k_B T}\right)\right\}, \tag{1.8}$$

where $Z(T)$ is the partition function at temperature T, and k_B is the Boltzmann constant. If a given quantum system does indeed thermalise, then as we take the large system and high temperature limit simultaneously, the reduced density matrix given by quantum statistical mechanics (1.6), and equilibrium thermodynamics (1.8), should be consistent

with each other, such that $\rho_A(t) = \rho_A^{(\mathrm{eq})}(T)$ for all possible choices of subsystem A. This is the basic idea behind the concept of quantum thermalisation; however, we have implicitly assumed that all systems, in our iterative application of the thermodynamic limit, have initial states that are prepared in, or near, equilibrium. What if we were to consider an initial state far from equilibrium? In this case, we would need to look at its unitary time evolution to confirm or deny the prospect of thermal equilibrium in the long-time limit.

1.3 The Eigenstate Thermalisation Hypothesis

For systems that successfully thermalise under their own dynamics, we can say that the *many-body eigenstates* of their Hamiltonians will generically obey a set of ideas known as the *eigenstate thermalisation hypothesis* (ETH). The purpose of the ETH is to explain when, and why, a quantum-mechanical system in isolation can be accurately described using the more traditional laws of statistical mechanics. It is especially useful for explaining how systems prepared in far-from-equilibrium initial states can evolve in time, via unitary time evolution, to a final state that resembles thermal equilibrium. The phrase "eigenstate thermalisation", in this context, was coined by Mark Srednicki in 1994 [14], after similar ideas had been introduced by Josh Deutsch in 1991 [13].

The primary purpose of the ETH is to explain the phenomenon of thermalisation in closed quantum systems—in a sense, it attempts to extend the notion of the microcanonical ensemble towards a more canonical description, where concepts such as thermalisation are rendered more explicitly. The ETH motivates the introduction of a new type of quantum statistical ensemble—a so-called *single-eigenstate ensemble*, which gets its name from the fact that each such ensemble consists of a single eigenstate of a given system's Hamiltonian. This ensemble can be thought of as an extreme limiting case of the more traditional microcanonical ensemble, where the range of eigenenergies has been decreased such that it contains only one eigenstate. The usefulness of such an ensemble becomes more clear when one considers a system that violates the ETH; however, we should first explain what the ETH is, and it is useful to do so via the formalism of density matrices that was introduced in section 1.1.

If we initialise our system—represented by a density matrix denoted ρ—in a pure state that is also one of the eigenstates of the Hamiltonian, then the time evolution of the system

is simply

$$\rho(t) = \rho(0) \tag{1.9}$$

for all times t [2]. Therefore, if there is thermalisation of initial states, then this implies that all the eigenstates of the Hamiltonian are "thermal". We should now define a complete set of basis states for our system—the eigenstates of the Hamiltonian H, which obey the relation

$$H\left|\psi_n\right\rangle = E_n\left|\psi_n\right\rangle \tag{1.10}$$

where E_n is the eigenenergy associated with eigenstate $|\psi_n\rangle$. Since we work in the energy eigenbasis, we can state $E_n = \langle H\rangle_{T_n}$, where $\langle H\rangle_{T_n}$ is the thermal equilibrium energy at temperature T_n—obtained from a weighted average over a range of eigenenergies. By representing our system as a density matrix ρ, and using the eigenbasis defined in Eq. (1.10), our system will have the following dynamical properties: the diagonal matrix elements $\rho_{nn} = \langle\psi_n|\rho|\psi_n\rangle$ will be constant, and the off-diagonal matrix elements $\rho_{nm} = \langle\psi_n|\,\rho\,|\psi_m\rangle$ will precess in the complex plane at a constant rate given by

$$\rho_{nm} = \rho(0)\exp\left[\frac{i(E_m - E_n)t}{\hbar}\right]. \tag{1.11}$$

If the entire system is in a particular energy eigenstate $|\psi_n\rangle$, then its density matrix can be written as $\rho_n = |\psi_n\rangle\langle\psi_n|$, thus allowing us to write the density matrix of subsystem A as $\rho_A^{(n)} = \mathrm{Tr}_B\{|\psi_n\rangle\langle\psi_n|\}$, as previously explained in Eq. (1.6). The ETH makes the following assertion: if the thermodynamic limit has been taken, then the system is in thermal equilibrium. This can be expressed as

$$\rho_A^{(n)} = \rho_A^{(eq)}(T_n). \tag{1.12}$$

One consequence of this is that the entanglement entropy between A and B in a particular eigenstate, given by

$$S_{AB} = -k_B\,\mathrm{Tr}_A\left\{\rho_A^{(n)}\log\rho_A^{(n)}\right\}, \tag{1.13}$$

will be equal to the thermodynamic entropy of subsystem A. Eq. (1.12) establishes consistency between the different techniques used to calculate the properties of thermalisation in different circumstances. The entanglement entropy, shown in Eq. (1.13), exhibits *volume-law* scaling for eigenstates with nonzero temperature T_n. This means that, if the d-dimensional system is attributed with a length L, then the entanglement entropy will

scale as L^d. In addition to the earlier statement, encompassed by Eq. (1.12), the ETH also requires that the difference between the matrix elements of any subsystem operators $\rho_A^{(n)}$, that belong to distinct eigenstates, becomes exponentially small when the thermodynamic limit is taken [48]. This ensures that any temporal fluctuations in such an operator will vanish, in accordance with what is expected from a system in thermal equilibrium. If all of the assertions of the ETH are true for *all* of the eigenstates of a system, then we say that the system successfully thermalises; however, it seems there is some evidence to suggest that a system can be classified as thermal as long as *almost all* of its eigenstates obey the ETH [14]. A useful diagnostic for checking if the ETH is true or false in a given system is to consider the form of a given few-body (i.e. local) quantum-mechanical observable $\hat{A}$, with matrix representation $A_{nm} = \langle\psi_n|\hat{A}|\psi_m\rangle$ in the energy eigenbasis. If A is diagonal in the energy eigenbasis, then all of its subsystems are in thermal equilibrium, and thus its eigenstates obey the ETH.

In order to apply the ETH to a system with far-from-equilibrium eigenstates, we must first define what the structure of these states should be. The matrix A, for a generic out-of-equilibrium state, will have a specific off-diagonal structure, in which the off-diagonal elements A_{nm} will possess a so-called "coherence pattern" between eigenstates with different eigenenergies. The structure of this coherence pattern can be described by the following two conditions imposed on the structure of the matrix:

1. The diagonal matrix elements A_{nn} will vary smoothly as a function of energy, with the difference between adjacent eigenstates $A_{n+1,n+1} - A_{n,n}$, becoming exponentially small for larger systems.

2. The off diagonal elements A_{nm} will be much smaller than the diagonal matrix elements A_{nn}, and should themselves be exponentially small for larger systems [47].

However, the more general requirements for this coherence pattern are manifested in the following properties of the matrix: the diagonal terms A_{nn} will be time-independent, while the off-diagonal terms A_{nm} will precess, according to Eq. (1.11), such that the phases of these off-diagonal elements will become "scrambled" by unitary time evolution. Thus, their contributions to local observables will possess random phases which will cancel. This is a process referred to as *dephasing*, and is essentially equivalent to equilibration, provided we work in the energy eigenbasis. Therefore, if we consider a finite system with no degeneracy

in its energy eigenvalues, then it will possess a discrete, nondegenerate energy spectrum, and the rate of precession, as shown in Eq. (1.11), will always vary in time—i.e. any initial conditions that manifested themselves in off-diagonal elements will change with time, and thus are not "stored" by the system, implying thermalisation. This allows us to label the full set of eigenstates in ascending order, with respect to their energy eigenvalues, which may be convenient for analysis. This assumption is not wildly unreasonable, as most realistic physical systems will have sufficient disorder and interaction strength as to make almost all degeneracies vanish [49].

We now know what the ETH is, and what it tries to accomplish; however, it is important to remember that the ETH is a *hypothesis*, and thus it is not necessarily unfailing in all cases. The best we can say is that it appears to be true for many classes of system; however, even for systems where it appears to hold true, thoroughly testing whether or not it actually does is a difficult process numerically speaking. This is because testing its validity generally requires exact diagonalisation[2] of the Hamiltonian and extrapolation to the thermodynamic limit, which has a high computational "cost" for systems with many degrees of freedom. Models that showcase both agreement and violation of the ETH will be covered explicitly in later chapters. For now, however, we move onto an important point of discussion: a phenomenological description of localised systems, which belong to a broad class of system that violates the ETH.

1.4 Many-body Localisation in a Phenomenological Model

Initially, the study of localisation was restricted to near-ground-state regimes or noninteracting particles in a random potential; however, there is now more-recent focus on the study of interacting *many-body localised* (MBL) systems in highly excited states far from the ground state. These higher-energy localised systems possess an energy density that corresponds to nonzero temperature; in theory, such localised systems can maintain their robust nonequilibrium nature for arbitrarily high temperatures—even temperatures approaching infinity [5]. Since the recent focus is on said "high-temperature" MBL systems, that is what we will focus on in this chapter. Although phenomenologically similar to *single-particle localisation* (SPL)[3] in many ways, MBL has a key difference—whereas

[2] By which we simply mean diagonalisation that acquires accurate eigenvalues and eigenvectors.
[3] See [50] for a detailed review, and see [8] for the original paper by P. W. Anderson.

Thermal phase	Single-particle localised	Many-body localised
Memory of initial conditions 'hidden' in the global operators at long times	Some memory of local initial conditions preserved in local observables at long times	Some memory of local initial conditions preserved in local observables at long times
ETH true	ETH false	ETH false
May have non-zero DC conductivity	Zero DC conductivity	Zero DC conductivity
Continuous local spectrum	Discrete local spectrum	Discrete local spectrum
Eigenstates with volume-law entanglement	Eigenstates with area-law entanglement	Eigenstates with area-law entanglement
Power-law spreading of entanglement from non-entangled initial condition	No spreading of entanglement	Logarithmic spreading of entanglement from non-entangled initial condition
Dephasing and dissipation	No dephasing, no dissipation	Dephasing but no dissipation

Figure 1.3: A table comparing the key differences between the ergodic thermal phase and both variants of localised phase.

SPL deals with the concept of a noninteracting localised system, MBL introduces interactions into the fray. This results in differing properties, including, but not limited to, the logarithmic spreading of entanglement and the dephasing of spins, amongst others (see Fig. 1.3). Both of the aforementioned phenomena are absent in SPL, but all MBL systems that we know of exhibit them. In order to understand why these properties exist in MBL systems, we proceed with a model that can capture this strange phenomenology.

For simplicity, let us assume we have a system composed of N local two-state systems. The two degrees of freedom in these two-state systems will be labelled by the set of Pauli operators $\{\sigma_i^a\}$ (where $a \in \{x, y, z\}$), and will be referred to as *p-bits*, where "p" stands for "physical". These p-bits could be physical spin-1/2's, but this is an arbitrary choice as they could just as easily be modelled in an alternative way (which we exploit in later chapters). We now define a Hamiltonian involving these p-bits, which we assume to have *quenched disorder*—referring to the disorder of an out-of-equilibrium state, such as a *spin glass* [51], with strictly short-range interactions. If we introduce high levels of disorder into our system—generally onsite disorder via some inhomogeneous random field—then such a Hamiltonian could potentially transition into a *fully many-body localised* (FMBL) regime where all of its many-body eigenstates violate the ETH, and are thus localised by definition. In this FMBL regime, we can now introduce localised two-state systems—argued in [52], [15], [16] (amongst others), and explicated further in chapter 2—which are

analogous to the introduction of pseudoparticles, henceforth referred to as *pseudospins*. The two degrees of freedom in these localised two-state systems will be labelled by a set of *localised Pauli operators* $\{\tau_i^a\}$ (where $a \in \{x, y, z\}$)—we will refer to these as *l-bits*, where "l" stands for "localised". Using these l-bits, we can construct a phenomenological Hamiltonian in the FMBL regime

$$H = E_0 + \sum_i h_i \tau_i^z + \sum_{i,j} J_{ij} \tau_i^z \tau_j^z + \sum_{n=1}^{\infty} \sum_{i,j,\{k\}} K_{i\{k\}j}^{(n)} \tau_i^z \left(\prod_{m=1}^{n} \tau_{k_m}^z \right) \tau_j^z, \tag{1.14}$$

where E_0 is a constant energy offset, h_i represents the on-site potential at l-bit i, J_{ij} represents the direct interaction between two l-bits, i and j, and $K_{i\{k\}j}^{(n)}$ represents the indirect interaction between two l-bits, i and j—due to the many-body interactions of $(n+2)$ l-bits—which are represented by the $\{\tau_k^z\}$ in the sum. It is important to note that each interaction term in this many-body sum is counted only once. E_0 exists simply to ensure that the trace of the Hamiltonian vanishes, and as such, does not affect the dynamics of the l-bit system whatsoever. Also note that all of the $\{\tau_i^z\}$ are mutually commuting with each other, and with the Hamiltonian; in other words, the eigenstates of the Hamiltonian are simultaneous eigenstates of all of the $\{\tau_i^z\}$, leading to completely nonentangled l-bits [15].

Although we are considering FMBL systems in the case of Eq. (1.14), this does not necessarily have to be true in general. It has been argued that there may exist a *mobility edge* within some MBL systems at some system-specific extensive energy [53]. It was suggested that eigenstates would be thermal if their energy density was above the mobility edge, and would be localised if their energy density was below it; however, it has been suggested this mobility edge could possibly be "inverted" by considering a model where the single-particle level spacing increases with energy [54]. The consequences of this "inversion" would be that eigenstates would only become localised *above* a certain critical energy, as opposed to below. In principle, there is nothing forbidding a model with multiple mobility edges, although this has currently not been explored too deeply as of yet. Modelling an MBL system that has a mobility edge is significantly harder than modelling an FMBL system; this is partially due to the fact that there can exist rare regions where the energy density of a localised eigenstate lies arbitrarily close to the mobility edge—a new type of *Griffiths singularity* [15]. The treatment of these rare regions, along with the exact nature of the transition that occurs at the mobility edge, remains an open problem.

By looking at the structure of Eq. (1.14), we can intuit some of the properties it should have, which in turn determine the phenomenological properties of the localised regime. As mentioned previously, the many-body eigenstates of a Hamiltonian in the localised regime violate the ETH, thus forbidding any transport of conserved quantities. This leads us to deduce that there should exist a set of localised conserved "charges"[4] $\{\tau_i^z\}$, which remain invariant under the dynamics of the system—these charges can be thought of as constants of motion. Since the l-bits are localised in real space, they can be written as a sum of p-bit operator products $\prod_i \sigma_i^a$ (where $a \in \{x, y, z\}$), where each of these p-bit operators σ_i^a describe p-bits that are all on nearby sites i, and are thus localised around a particular region in real space.

With the way we have constructed these l-bits, each many-body term in Eq. (1.14) has a weight which typically falls off exponentially with the distance to the farthest p-bit operator σ_i^a in the product. This is due to the exponentially decreasing values of the interaction strengths, J_{ij} and $K^{(n)}_{i\{k\}j}$, as one moves away from the aforementioned localised region of p-bits. This produces exponentially decreasing "tails", in their real-space distributions, which stretch off to infinity, mimicking an extremely narrow Gaussian distribution. Due to the finite coupling strength between them, these tails mediate the long-range interaction between l-bits, thus implying that these long-range interactions also fall off exponentially with distance. For weakly interacting systems, the l-bits are presumed to have significant overlap with the bare p-bits; therefore, in the regime of weak interactions, we should be able to perturbatively "dress" the p-bits to produce our constants of motion $\{\tau_i^z\}$—this "dressing" also falls off exponentially with distance. However, this has recently proved to be a naive general presumption, as the l-bits of the paradigmatic spinless fermion model have been shown to possess a distinctly nonperturbative nature[5] [55]. Nevertheless, we maintain this assumption here, for the sake of simplicity.

The existence of long-range interactions between l-bits may seem counter-intuitive—since we previously stated that the p-bit Hamiltonian only accounts for strictly short-range interactions, and thus only couples p-bits which are nearby in real space—however, due to the way we have dressed the p-bits to form l-bits, each p-bit has a non-zero coupling to each l-bit, regardless of their real-space separation. This is because, when expanded in terms of

[4] These conserved charges will vary depending on the choice of system. For example, in a system of noninteracting fermions subject to a disordered potential, the charges would be the occupation numbers of each of the localised single-particle orbitals [15], which we also consider explicitly in chapter 2.

[5] This was one our significant findings, and is the focus of chapter 2.

l-bits, a p-bit consists of an infinite sum of l-bit operators, where the weight of the long-range terms falls off exponentially with range, thus producing the exponentially decreasing tails which stretch off to infinity. This means that, while exponentially decreasing, the long-range terms are nonzero, and will thus couple l-bits regardless of distance, albeit negligibly for extremely long ranges. The fact that these l-bits interact with each other inevitably leads to dephasing between these initial p-bit product states, which consequently means that there will be no local observables that show persistent oscillations, according to Eq. (1.11), in the long-time limit.

The p-bits and l-bits possess vastly different dynamics; whereas the dynamics of entangled p-bits leads to *dissipation* due to spin "flips", there is no such dissipation regarding l-bits due to the lack of any spin flips. When these dynamics are represented on a Bloch sphere (see Fig. 1.1), the l-bits will still precess in the xy-plane, but their z-components will remain fixed at a certain value—the z-components are "frozen" and no spin flips occur. The lack of dissipation must mean that the spreading of entanglement in the thermal phase, composed of p-bits, must behave differently in comparison with the FMBL phase, composed of l-bits. Therefore, it is useful to highlight the key points regarding the spreading of entanglement in each of these phases, in order to better grasp the reasoning behind their respective dynamics.

1.5 Entanglement Behaviour

Previously, in section 1.3, we introduced the concept of the volume-law, wherein the entanglement entropy of a given many-body eigenstate scales with the size of the system. The reason for this scaling can be explained quite simply using an example: Say we had a traditional d-dimensional thermalising system of length L, composed of an ensemble of spins, or—to use our previously-established vernacular—p-bits. The direct interaction between two p-bits, A and B, produces entanglement between A and B, and thus results in the precession of each of these individual p-bits in the xy-planes of their respective Bloch spheres (see Fig. 1.1). As their xy-components become coupled with each other, signifying entanglement between the p-bits, this results in dephasing and decoherence. If B was to subsequently interact with another p-bit C, then C would not only become entangled with B, via direct interaction, but also with A, via indirect interaction. This spreading of

entanglement is *ballistic* in nature, and the speed at which entanglement spreads in such a system is of the order of the *Lieb-Robinson velocity*—a theoretical finite upper bound on the speed at which quantum information can travel [56]. The larger the volume of the thermalising system, the faster entanglement will spread, simply due to the greater number of particles leading to a greater number of interactions—both direct and indirect. This is what leads to the so-called volume-law, where the entanglement entropy scales as $S_{thermal} \sim L^d$.

However, entanglement spreads very differently in FMBL systems, where the spreading of entanglement is no longer ballistic. As we can see from our FMBL Hamiltonian in Eq. (1.14), the interactions between two pseudospins, A and B, which we call l-bits, are determined only by the projective measurement τ_i^z on each individual l-bit. Since, as we stated previously, these operators $\{\tau_i^z\}$ are constants of motion, this means that any subsequent interactions between B and another l-bit C will not produce entanglement between A and C—entanglement can only occur through direct interaction. Increasing the size of a system in the FMBL regime will still increase the rate at which entanglement spreads, due to the greater number of direct interactions; however, due to the lack of indirect interactions, we can deduce that the spreading of entanglement in the FMBL regime must be much slower than in a thermalising system of the same size. Therefore, FMBL systems will not possess a volume-law, and will instead possess an area-law, where the entanglement entropy scales as $S_{FMBL} \sim L^{d-1}$—sometimes possessing a logarithmic correction of the form $S_{FMBL} \sim L^{d-1} \ln L$ [3].

By making use of the Heisenberg uncertainty principle $\Delta E \Delta t \sim 1$ ($\hbar = 1$), we can say that the interactions J_{ij} within our FMBL system will have a noticeable impact on the phase of a precessing l-bit once Jt is of order one. Using this fact, we can now say that the time taken for two l-bits, separated by distance R, to become entangled with each other is approximated by

$$t \sim \frac{1}{J(R)}, \tag{1.15}$$

where $J(R)$ is the total interaction strength between two l-bits separated by a distance R, and is thus composed of a sum of the individual terms J_{ij}. Since the individual terms J_{ij} decrease exponentially with range, this means that $J(R)$ must also decrease exponentially with range, albeit at a slightly slower rate. This exponential fall-off can be approximated

as

$$J(R) = J\left[V(R)\right] \propto \exp\left[-V^{\frac{1}{d}}(R)\right], \tag{1.16}$$

where $V(R)$ is the finite-interaction volume around a given l-bit with radius $\sim R$, and $V^{1/d}(R) \sim R$. By solving Eqs. (1.15) and (1.16) simultaneously, we can obtain

$$V(t) \sim \ln^d(t), \tag{1.17}$$

which tells us that after time t has passed, a given l-bit will become entangled with all other l-bits within a volume $V(t)$ around it. In order to more accurately model the effective interaction between two l-bits, we can rewrite the Hamiltonian in Eq. (1.14) as

$$H = E_0 + \sum_i h_i \tau_i^z + \sum_{i,j} \tau_i^z J_{ij}^{\text{eff}} \tau_j^z, \tag{1.18}$$

where the individual effective interaction terms between two l-bits, i and j, in a particular many-body eigenstate are given by

$$J_{ij}^{\text{eff}} = J_{ij} + \sum_{n,\{k\}} K_{i\{k\}j}^{(n)} \left(\prod_{m=1}^{n} \tau_{k_m}^z \right). \tag{1.19}$$

The effective interaction, defined in Eq. (1.19), is useful for explaining the behaviour of the multispin terms, which dominate the effective interaction at long range. The dominant multispin terms, with comparatively high values of $K_{i\{k\}j}^{(n)}$, will have all of their sites k_m near the straight line that connects sites i and j. Flipping a single spin k will change the expectation value of every τ_k^z from one to minus one (or vice versa), and thus change the sign of every multispin term containing this spin. If a spin far from the straight line connecting sites i and j is flipped, it will have little effect on the overall sum; however, flipping a spin that lies directly on the straight line between i and j will change the sign of a significant number of the dominant multispin terms. This cancellation of multispin terms leads to dramatic differences between *different* many-body eigenstates of Eq. (1.14). In the context of our model, this is the reasoning behind spin flips leading to dissipation. While spin flips may occur in thermalising systems, they will not occur in MBL systems, since all of the $\{\tau_k^z\}$ within the l-bit Hamiltonian are constants of motion. Also, since both J_{ij} and $K_{i\{k\}j}^{(n)}$ decrease exponentially with range, this leads to J_{ij}^{eff} also decreasing exponentially with range; therefore, the total effective interaction between two l-bits, i

and j, can be approximated as

$$J^{\text{eff}}(R) \sim J_0 \exp\left(-\frac{R}{\tilde{\xi}}\right), \tag{1.20}$$

where $\tilde{\xi}$ defines a quantity which will be referred to as the *interaction decay length*—henceforth referred to simply as the *interaction length* for brevity. $J^{\text{eff}}(R)$ is composed of a sum of 2^R individual terms J_{ij}^{eff}; therefore, since the J_{ij}^{eff} terms also decrease exponentially with range, this means that the interaction lengths $\tilde{\xi}_{ij}$ of the individual terms will be shorter than the full interaction length $\tilde{\xi}$[6]. We can now attempt to obtain the entanglement entropy as a function of time; but first, we must define a system, and an initial state, to work with. If we initialise our FMBL system in a nonentangled pure state—and consider the long-time growth of the *bipartite entanglement entropy* between two semi-infinite spin chains [5]—then the distance R that the entanglement entropy spreads in time t is given simply by rearranging Eq. (1.20) for R and substituting $J^{\text{eff}}(R) \sim 1/t$. Performing these manipulations, we obtain

$$R(t) \sim \tilde{\xi} \ln(J_0 t). \tag{1.21}$$

In the long-time limit, the initial state eventually dephases due to interactions, and produces a *von Neumann entropy* [57] given by

$$\begin{aligned} s(\tilde{\xi}) = s[\rho(\tilde{\xi})] &\equiv -\operatorname{Tr}\left[\rho(\tilde{\xi}) \log_2 \rho(\tilde{\xi})\right] \\ &= -\sum_i \lambda_i(\tilde{\xi}) \log_2 \lambda_i(\tilde{\xi}), \end{aligned} \tag{1.22}$$

where $\rho(\tilde{\xi})$ is the density matrix of our system as a function of the interaction length $\tilde{\xi}$ and the $\{\lambda_i(\tilde{\xi})\}$ are the eigenvalues of $\rho(\tilde{\xi})$. The Boltzmann constant k_B is set to one for convenience. We also define $0 \log_2 0 \equiv 0$ [57], thus avoiding any potential singularities that could arise. The von Neumann entropy, as shown in Eq. (1.22), is sometimes referred to as the *diagonal entropy*, since the only the diagonal elements of $\rho(\tilde{\xi}) \log_2 \rho(\tilde{\xi})$ contribute to the trace. The resulting entanglement entropy of our system is obtained by multiplying Eqs. (1.21) and (1.22) together, producing

$$S_{EE} = s(\tilde{\xi}) \tilde{\xi} \ln(J_0 t). \tag{1.23}$$

Note that different eigenstates will have varying interaction lengths $\tilde{\xi}$, and will thus produce different diagonal entropies, since the diagonal entropy is the measure of entropy

[6] The existence of differing interaction lengths, which may behave differently from each other, emphasises the need to carefully define which interaction length we are considering at any given time.

for a *particular* quantum state. The entanglement entropy is therefore dominated by the eigenstates which maximise the quantity $s(\tilde{\xi})\tilde{\xi}$, as can be seen in Eq. (1.23). Recalling that p-bits can be expressed as an infinite sum of l-bits, this means that their entanglement will also grow logarithmically with time, in accordance with Eq. (1.23), in the long-time limit. This is consistent with the results found in [7] and [58].

1.6 Conserved Quantities and Localisation Length

We have casually mentioned "dressing" the bare p-bits to form l-bits, but how exactly is this done? Unfortunately, there is no single answer to this question. A given system of spin-s particles system possesses $(2s+1)^N$ degrees of freedom, resulting in a staggering $[(2s+1)^N]!$ discretely different ways of constructing a set of operators with a unique bijective mapping to each of the $(2s+1)^N$ many-body eigenstates of a given Hamiltonian. We will henceforth call these unique bijective mappings "assignments". Each assignment will produce a different definition of l-bits; therefore, in order to fully enumerate a particular assignment, we need to set the $(2s+1)^N - 1$ relative phases, quantified by Eq. (1.11), between each of the $(2s+1)^N$ eigenstates. As previously discussed in section 1.3, systems that obey the ETH will have their phases set in a particular way, so as to cancel off any long-time contributions to local observables; however, these contributions to local observables should not cancel off in the localised regime, and should thus preserve information about the initial state of the system. Setting an assignment where the $(2s+1)^N-1$ relative phases do not cancel off in the long-time limit turns out to be quite difficult, as almost all of these assignments will result in eigenstate thermalisation, and thus fail to produce l-bits in the localised regime.

Nonetheless, a relatively convenient way of doing this is to start with the bare p-bits—which, by definition, mutually commute with each other and the Hamiltonian—and "dress" them iteratively, order by order in perturbation theory, necessitating order n in perturbation theory when involving any p-bit a distance n away. At each step along the way, we ensure that the l-bits retain the same commutation relations that the p-bits possess—their mutual commutativity with each other and the Hamiltonian. This approach, while convenient, has its limitations. One such limitation is the fact that it will fail to produce unique l-bits outside of the weak-interaction limit, due to degeneracies involved with the

use of perturbation theory, inevitably resulting in an ambiguous definition of l-bits [18]. Another such limitation is the assumption that the p-bits adiabatically connect to the l-bits at all—while a seemingly innocent assumption, it is by no means guaranteed, as we will discuss in chapter 2.

In spite of these limitations, there do exist ways to present a more complete, and nonperturbative, definition of l-bits that possess the properties we wish them to have [59]. One possible way is to construct the l-bits using *projection operators* [15]. In order to simplify things, let us construct the l-bit operators for a particular site k, located in real space. We do this for a particular assignment where the many-body eigenstates of Eq. (1.14)—simultaneous eigenstates of all of the τ_k^z—have relative phases which are implicitly assumed. Half of the many-body eigenstates $\{|\alpha\rangle\}$ will have $\langle\tau_k^z\rangle_\alpha = +1$, and can be "flipped" in order to create $|\bar{\alpha}\rangle = \tau_k^x |\alpha\rangle$, which has $\langle\tau_k^z\rangle_{\bar{\alpha}} = -1$. There will exist $2^N/2 = 2^{(N-1)}$ of these states $\{|\alpha\rangle\}$, and all other τ_l^z's will have the same value in $|\alpha\rangle$ and $|\bar{\alpha}\rangle$. Using these constraints, we can now define the l-bits via localised Pauli operators [15], which take the form:

$$\tau_k^x = \sum_\alpha \left(|\alpha\rangle\langle\bar{\alpha}| + |\bar{\alpha}\rangle\langle\alpha|\right), \tag{1.24}$$

$$\tau_k^y = -i\sum_\alpha \left(|\alpha\rangle\langle\bar{\alpha}| - |\bar{\alpha}\rangle\langle\alpha|\right), \tag{1.25}$$

$$\tau_k^z = \sum_\alpha \left(|\alpha\rangle\langle\alpha| - |\bar{\alpha}\rangle\langle\bar{\alpha}|\right). \tag{1.26}$$

We can easily confirm that these l-bit Pauli operators obey the same commutation relations as the more traditional p-bit Pauli operators $\{\sigma_i^a\}$ (where $a \in \{x, y, z\}$), and are thus suitable definitions of l-bits in the localised regime.

Now, in order to be able to analyse our system more readily, we set a unique assignment between the 4^N many-body p-bit operators and the set of all operators that can be written as outer products of the form depicted in Eq. (1.5). The l-bit operators defined by Eqs. (1.24), (1.25), and (1.26) can therefore be expanded as a function of these many-body p-bit operators. By looking at the form of these many-body p-bit operators, we can define a range r as the distance between the two farthest-apart non-identity p-bit Pauli operators contained within the outer product. By taking the weighted average (using the norm of the operators) over the values of r for a particular l-bit k, we can obtain the mean range $\overline{r}_k$ for that l-bit. This mean range $\overline{r}_k$ gives us an indication of the maximum distance between

coupled l-bits, before the interaction terms in the Hamiltonian start becoming insignificant. By averaging over all of the $\{\overline{r}_k\}$ in our system, we can obtain a characteristic mean range $\overline{\mathcal{R}}$ for our entire system of l-bits. It is important to note that the definitions stemming from these weighted averages are arbitrary, and a more convenient definition may exist depending on the circumstance. For a given FMBL system, provided we have chosen an appropriate assignment, we can make the hopeful prediction that this mean range $\overline{\mathcal{R}}$ is finite and robust to the thermodynamic limit, where the energy density corresponds to infinite temperature. The optimal assignment is defined as the one that minimises this mean range $\overline{\mathcal{R}}$, thus providing one possible measure of the so-called *localisation length* ξ, which is expected to diverge at the transition between the ergodic and localised regimes. Speaking in a general sense, localisation implies that quantum correlations, such as entanglement, between our l-bits should have a finite extent set by this localisation length ξ; therefore, the localisation length ξ makes an appearance in the area-law described in section 1.5—approximated by $S_{FMBL} \sim \xi L^{d-1}$ [3].

By using the aforementioned optimal assignment, the l-bits will generically consist of an infinite sum of many-body p-bit operators. Although, similarly to the reverse—i.e. p-bits expanded in terms of l-bits—the weight of each of these terms will fall off exponentially with range. It is also worth noting that, while most of l-bits will have ranges which lie fairly close to the mean range $\overline{\mathcal{L}}$, some of them will possess a range much greater than $\overline{\mathcal{L}}$ due to *resonances* within the system. These l-bits are fairly uncommon in most systems, and the probability of them occurring will fall off exponentially with range [15].

1.7 The Notion of Integrability

For dynamical quantum systems governed by a Hamiltonian, there exists the notion of *quantum integrability*, which essentially means the model in question is solvable via the *Bethe ansatz*[7]—an ansatz method for finding the exact wavefunctions of certain one-dimensional quantum many-body models, including the Anderson impurity model. The methodology behind this relates to the *Yang-Baxter equation*, which is used to obtain the so-called *transfer matrix* of a particular quantum system—this is used to generate an infinite set of conserved quantities that commute with the Hamiltonian, including the Hamiltonian itself. Therefore, if we can construct a transfer matrix that satisfies the

[7] See Refs. [60] and [61] for an introductory overview of the Bethe ansatz and the Yang-Baxter equation.

Yang-Baxter equation, and also generates the Hamiltonian, then we deem this particular quantum system to be *integrable*.

Using the aforementioned methodology, we can argue that the Hamiltonian in Eq. (1.14) can be classified as integrable in certain regimes. Turning to the phenomenological features of one-dimensional integrable systems, we find useful markers of integrability; for example, systems comprising a one-dimensional, translationally invariant chain of N spins, will typically possess N conserved densities[8] that we denote $\{\bar{n}_i\}$. Interestingly, it seems that FMBL systems can, in a sense, possess many more conserved densities than this due to the nature of the l-bits we have constructed—if we consider n l-bits near site k, then we can create 2^n independent conserved quantities, all localised around k, by making l-bit product states of the form $\bigotimes_{k=1}^{n} \tau_k^a$ (where $a \in \{0, x, y, z\}$) [15]. Another notable property is the fact that the Hamiltonian in Eq. (1.14) will retain its integrable structure even when weakly perturbed—it is robust to small parameter variations. This stems from the notion that the constants of motion $\{\tau_k^z\}$ can simply be redefined under weak perturbations. Note, however, that a Hamiltonian robust to weak perturbation need not always possess l-bits which are straightforwardly redefined in perturbation theory—the latter implies the former, but the former does not imply the latter.

1.8 Spin Echo and Potential Applications

Having explored the unique phenomenology of many-body localised systems—such as logarithmic spreading of entanglement, finite dephasing (despite zero dissipation), and emergent integrability—it is natural to ponder whether or not these novel properties have any potential applications. Perhaps unsurprisingly, the answer is a resounding yes. It turns out that the lack of dissipation, due to the lack of any l-bit spin flips, enables dephasing to potentially be reversed via *spin echo* procedures[9]. The basic concept underlying a spin echo measurement is best described using an example: Say we were to set up a weakly interacting system consisting of two spins, A and B. The precession of spin A will be affected by the precession of spin B, and vice versa, thus generating mutual entanglement. Eventually, the different precession speeds of spins A and B will result in dephasing between the two; however, we can "refocus" the phase of spins A and B via a

[8] If one tries to create additional conserved densities by forming a so-called composite density of the form $\bar{n}_i \otimes \bar{n}_j$, then it appears that these will be non-local operators with an approximate range N [15].

[9] See [3] for a more detailed explanation of spin echo.

pulse of electromagnetic radiation at some resonant frequency—essentially reversing the dephasing between the two spins—and subsequently leaving a so-called spin echo which can be measured.

In theory, there is nothing preventing us from using MBL systems to store quantum information to be retrieved later via spin-echo procedures; however, there is a limitation that prevents us from doing so using generic spin-echo procedures. This limitation originates from the fact that l-bits are *pseudospins* that relate to p-bits via local unitary transformations of varying complexity, which are also often dependent on parameters such as disorder and interaction strength. This makes accessing l-bits experimentally a distinctly nontrivial task; at least, when compared to the generic procedures that exist for accessing p-bits. Therefore, while we can directly manipulate p-bits using standard spin-echo procedures, direct manipulation of l-bits is much more difficult since each one comprises a sum of p-bit product states. If we cannot directly manipulate a single l-bit, we will be unable to fully reverse the dephasing of this l-bit; thus, we do not have access to its spin echo. However, not all hope is lost. Promising work has suggested that "high-fidelity" spin echo measurements can be made [62,63], despite the fact that only p-bits are accessible; however, this is only strictly true in the "perturbative" regime [2], where l-bits are simply p-bits with very weak "dressing". As of yet, we are uncertain about what kind of spin-echo procedure is required to fully dephase an l-bit far outside of this perturbative regime; however, the revival probability of retrieving an initial state is large for strong enough disorder [4].

In addition to these spin-echo procedures, there exist other closely-related experimental signatures of dephasing dynamics. One such signature involves *temporal revivals* of local observables [64], and another concerns *double-electron resonance*—a modification of the aforementioned spin-echo procedures—allowing one to probe the dephasing of a given spin via the probing of distant spins [62]. Furthermore, power-law decays of various quantities have been identified for systems in the many-body localised regime—quantities including mutual information [65], fluctuations of the out-of-time-order correlation functions (OTOCs) [66], and fluctuations of the *Loschmidt echo* [67]. Each of these three power-law decays were found to stem from a common dynamical dephasing mechanism, indicating some universality in dephasing behaviour of many-body localised systems.

Chapter 2

Orbital Structure

2.1 Context and Background

Many-body localised (MBL) systems constitute a broad class of closed quantum systems that fail to equilibrate under their own dynamics [2–7]. This behaviour manifests itself as a violation of the eigenstate thermalisation hypothesis [13,14], a hypothesis that more conventional, ergodic systems obey. A pressing question [42] is whether the MBL phase can be explored equally well via features of the wavefunctions, such as in the area law of entanglement [5,6], and via energy-level statistics [9], as well as how firmly these approaches tie into key theoretical concepts. In particular, wavefunction-based characterisations so far approach each eigenstate individually, while energy-level statistics are generally based on energy-level spacings, and thereby involve the interplay of several states [6, 10, 11]. This leaves a conceptual gap between the most reliable characterisations of MBL and the most influential theoretical framework, the concept of robust emergent integrability [15–18], which ties the MBL phase transition to the emergence of an extensive set of local conserved quantities that are commonly referred to as l-bits [15–21]. These l-bits can be seen as highly structured constraints on the complete set of eigenstates of any given system, both energetically as well as in terms of their wavefunctions. In principle, an all-encompassing description of MBL should therefore also allow to develop expectations for the *joint characteristics of the wavefunctions* of a given system.

In this work, we set out a framework to formulate and verify such expectations for the paradigmatic case of fermionic systems, and use this to uncover their strongly correlated nature from a transparent geometric perspective. Our framework rests on the

observation that for these systems, the MBL wavefunctions are closely approximated by Slater determinants, a realisation that previously proved useful to lift Fock-space localisation [68, 69] into real space by means of the one-particle density matrix [25–35]. Here, we propose to capture this structure by considering the span of single-particle orbitals whose Slater determinant provides the largest overlap to a given eigenstate—known in quantum chemistry as Brueckner orbitals [22–24]—and show that this indeed provides a natural avenue to study the unexplored geometric interrelations between the wavefunctions of a given system.

Our key insights are the following: While individual MBL wavefunctions are indeed well approximated by a single Slater determinant, when comparing different eigenstates *of the same system* the underlying orbitals are generally mutually incompatible with each other. We define and quantify this mutual incompatibility precisely using a natural geometric measure, based on the projection operators of the occupied Brueckner orbitals from different eigenstates. We then establish the finite extent of this incompatibility in a model system, use random-matrix theory as a benchmark to show that it scales systematically with system size, and develop this picture further by varying the disorder and interaction strength. Finally, we relate the observed incompatibility to features of the aforementioned l-bit operators, whose systematical dressing is revealed by geometric correlations of states with different particle numbers. The proposed framework therefore provides a natural perspective on the emergence of MBL that complements traditional insights, revealing strongly correlated features that can be precisely quantified.

2.2 A Curious Question

As we discussed in the introduction, systems in the many-body localised regime are characterised by distinctive dynamical properties that are reminiscent of a phase transition into a non-thermal regime. Chief amongst these is the spontaneous emergence of an extensive set of conserved quantities which are invariant under the dynamics of the system. In the noninteracting case, we see individual physical particles—hereby referred to as *p-bits*—localise around specific positions in real space, as shown in Fig. 2.1(b). However, as we introduce finite interactions into the system—as shown in Fig. 2.1(c)—it is natural to wonder if there exists a many-body analogue to these p-bits which maintain the necessary

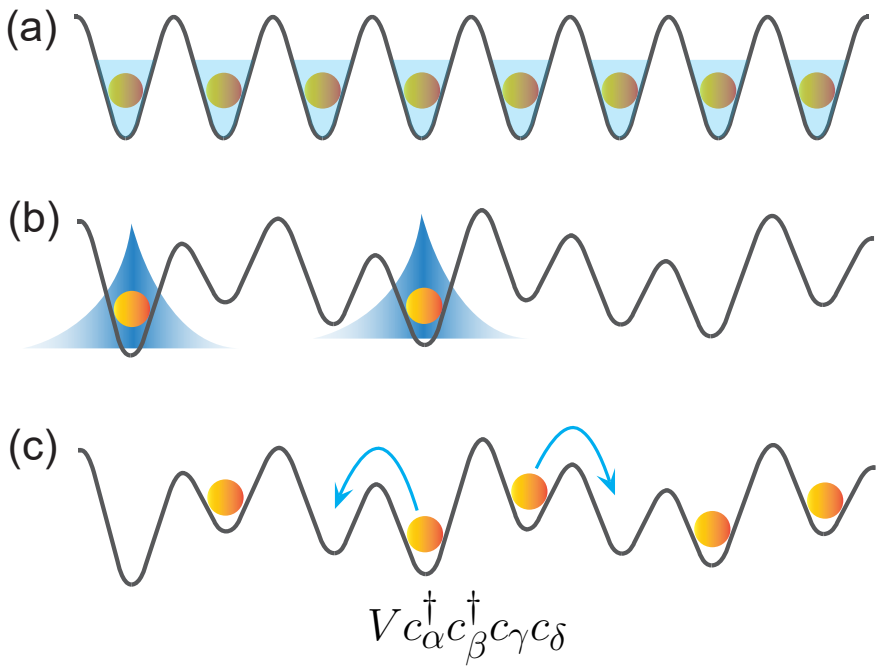

Figure 2.1: (a) In a typical non-disordered system—a clean crystal, for example—the eigenstates spread throughout the system in a Bloch-wave-like manner. The single-particle orbitals associated with such an eigenstate will all be occupied to roughly the same degree, signifying thermal equilibrium. (b) The distinguishing property of Anderson localisation is that, for sufficiently strong disorder, there is a vanishing probability that any given particle will make a resonant transition from one site to another spatially separated from it. The particles are thus spatially localised, with exponentially decaying presence as one moves away from it. The single-particle orbitals will therefore be distinctly occupied or unoccupied—their wave-like nature is lost. (c) It is instructive to ask what happens when one introduces finite interactions into an Anderson-localised system. To first order, this means the introduction of pairwise hoppings of particles between localised single-particle orbitals. It is natural to question if the localised phase is robust to such a process.

dynamical invariance. Let us hereby refer to these quasiparticle-like conserved quantities as localised bits, or *l-bits*. Of course, in the noninteracting case, l-bits simply take the form of p-bits; therefore, a natural construction of l-bits involves the adiabatic extension of these p-bits into the interacting regime via perturbative expansion. Such an expansion can be written as

$$q_i^\dagger = p_i^\dagger + \sum_{l,m,n} K_{lmn} p_l^\dagger p_m^\dagger p_n + \dots . \tag{2.1}$$

Note that the form of Eq. (2.1) implies that the l-bit operator $q_i^\dagger$ simply collapses to a bare p-bit operator $p_i^\dagger$ in the absence of interactions, where all the interaction constants $\{K_{lmn}\}$ are zero and we have perfect Fock-space localisation. It is not hard to see why such an l-bit construction is a highly attractive prospect, as it allows us to account for interactions via an iterative process, by which we gradually add terms that obey the same commutation relations as the p-bits; namely, that $\{q_i^\dagger, q_j\} = \delta_{ij}$, $\{q_i, q_j\} = 0$, and $[q_i^\dagger q_i, H] = 0$ for all i and j[1]. In addition, the l-bit operators must also generate a complete orthogonal set of single-quasiparticle orbitals which span the space of the single-quasiparticle sector[2]; thus, they should be able to identify all eigenstates of the Hamiltonian via some action on the vacuum state.

An instructive question arises: what is the minimum number of unique orbitals required to span a many-body localised system? Let us begin with the noninteracting case. Since, by definition, there is a bijective mapping between single-particle orbitals and p-bit operators $p_i^\dagger$, this question is equivalent to: how many p-bit operators $p_i^\dagger$ are required to form a complete basis of many-body eigenstates with the form $(\prod_i p_i^\dagger)\,|\text{vac}\rangle$? Say we have a system composed of N particles confined to a one-dimensional lattice of L atomic sites; the basis of such a system will be spanned by a number of eigenstates equal to the binomial coefficient $\binom{L}{N} = L!/N!(L-N)!$. Therefore, we can simply surmise that we require L p-bit operators $p_i^\dagger$, with each eigenstate being a unique product state of N of them $(\prod_i^N p_{x_i}^\dagger)\,|\text{vac}\rangle$. This is simply a restatement of the *Slater determinant* in *second quantisation* notation[3] (see appendix A.1). If it is truly the case that extending this notion into the regime of finite interactions simply requires that we evolve our p-bit single-particle operators $p_i^\dagger$ into l-bit quasiparticle operators $q_i^\dagger$, this means that, analogous to the noninteracting case, we will require L quasiparticle orbitals to span a general many-body localised system. These quasiparticle orbitals will map onto l-bit operators, but what form should these l-bit operators take?

On the face of it, the assumptions made in the perturbative construction of Eq. (2.1) are not at all outlandish; however, have they ever been verified? To make things as explicit as possible, we can summarise the purpose of this chapter with the exploration of two very

[1] In the case of bosonic p-bits, we need simply replace the anticommutation relations $\{a, b\}$ with commutation relations $[a, b]$.

[2] We will henceforth refer to single-quasiparticle orbitals simply as quasiparticle orbitals for brevity.

[3] There are many detailed sources which explain second quantisation notation in great depth, such as Ref. [78].

simply stated questions:

1. Are the eigenstates of a given many-body localised system well-approximated by Slater determinants?
2. If so, are these Slater determinants constructed from a common set of single-particle orbitals?

The former question pertains to a more general property of many-body localised systems; namely, that strongly localised eigenstates should be close to Slater determinants of quasiparticle orbitals. The entire premise of emergent integrability—in the context of low-to-moderate interaction strength—rests upon the answer to the former question being "yes". The latter question is more nuanced, and concerns what form l-bits should take. The validity of the perturbative expansion outlined in Eq. (2.1) rests upon the assumption that all eigenstates are constructed from a common set of L quasiparticle orbitals, thus immediately implying that the answer to the latter question is "yes". If the answer to this question is no, then we have identified an important flaw in considering l-bits as perturbative in nature.

2.3 Constructing Single-Particle Orbitals

2.3.1 The One-Particle Density Matrix

In order to quantify the extent to which defined l-bits manifest themselves in individual many-body localised eigenstates, we make use of the one-particle density matrix (OPDM), defined as

$$\rho_{ij}^{(n)} \equiv \langle \psi_n | \, c_i^\dagger c_j \, | \psi_n \rangle \,, \tag{2.2}$$

where $|\psi_n\rangle$ represents the nth many-body eigenstate. Note that we have also made the switch from generic p-bit operators p_i to explicit fermion creation and annihilation operators, denoted by $c_i^\dagger$ and c_i respectively. The OPDM is normalised differently to the more traditional density matrix, with $\mathrm{tr}\{\rho\} = 1$, in that it obeys the condition $\mathrm{tr}\,\{\rho\} = N$. Therefore, we can interpret its eigenvalues as single-particle occupations, as the L eigenvalues will conveniently sum to N. From each of these OPDMs, we can also obtain a set of L natural orbitals $\{|\phi_\alpha\rangle\}$, defined by the eigenvalue-eigenvector relationship

$$\rho \, |\phi_\alpha\rangle = n_\alpha \, |\phi_\alpha\rangle \,, \tag{2.3}$$

where n_α represents the occupation associated with the αth natural orbital $|\phi_\alpha\rangle$, which is subject to $\langle\phi_\alpha|\phi_\beta\rangle = \delta_{\alpha\beta}$. In the case of perfect Fock-space localisation, where all states are constructed from Slater determinants, the occupation spectrum of the OPDMs will be degenerate, and all occupations will be either one or zero exactly. In this case, the N natural orbitals with eigenvalue $n_\alpha = 1$ will span the space of the single-particle sector used in the relevant Slater determinant. However, this exact case is generally only guaranteed in the case of noninteracting systems, and it is more likely that the occupation spectrum will be non-degenerate in the case of non-zero interactions. In this case, there is no choice of N orbitals that will span the space of the entire single-particle sector, and thus all L orbitals are required.

The occupation spectrum of the OPDMs provides a useful diagnostic regarding the transition into the fully many-body localised regime: whereas systems in the ergodic phase will exhibit many-body-like occupations where $0 < n_\alpha < 1$, we expect systems in the localised phase to have well-defined occupations, such that $n_\alpha = 1$ or $n_\alpha = 0$. This behaviour signifies the suppression of Fock-space delocalisation in the many-body localised phase, while it is pronounced in the ergodic phase.

Therefore, in the many-body localised regime, the L natural orbitals serve as perfect candidates for the single-particle orbitals supposed in section 2.2, with the N occupied orbitals for a given eigenstate mapping directly onto the N single-particle operators required to build that eigenstate. However, this indeed presumes the answer to both questions in section 2.2 being "yes", which we have yet to verify. The answer to question 2 depends upon further numerical analysis; we can, however, remove the necessary presumption of question 1 by creating so-called best-fit Slater determinants that approximate a given eigenstate, which will be discussed in section 2.3.3.

2.3.2 Measures of Localisation

There exist typically utilised scalar measures that gauge the closeness of a given state to a Slater determinant; namely, the *occupation entropy* of a state's corresponding OPDM, given by

$$S_n = -\operatorname{tr} \rho_n \ln \rho_n, \tag{2.4}$$

along with its *purity*:

$$\mathcal{P}_n = \mathrm{tr}\left(\rho_n\right)^2, \tag{2.5}$$

where ρ_n is the OPDM associated with the nth many-body eigenstate, and $\mathbf{0}\ln\mathbf{0} \equiv \mathbf{0}$. From the form of Eq. (2.4), it can be seen that the occupation entropy will only be zero when all eigenvalues of the OPDM are either one or zero; therefore, states with a low occupation entropy will be close to a Slater determinant, and these states will also possess a high purity of order $\mathcal{P}_n \sim N$.

However, while the aforementioned measures are relatively quick to calculate, and provide reasonable qualitative evidence indicating closeness to a Slater determinant, we can utilise a more direct measure involving Brueckner orbitals, which we will now discuss.

2.3.3 Brueckner Orbitals

Brueckner orbitals are the name given to a set of N single-particle orbitals, each with dimension L, which maximise the overlap between a single Slater determinant constructed from these orbitals (optimal Slater determinant), and a given eigenstate of our system. To phrase this more mathematically, the Brueckner orbitals maximise the overlap

$$\mathcal{I}_n \equiv |\langle\psi_n|S_n\rangle|^2, \tag{2.6}$$

between eigenstate $|\psi_n\rangle$ and its corresponding optimal Slater determinant $|S_n\rangle$. Therefore, this allows us to accurately quantify how well a given eigenstate can be approximated by a single Slater determinant. These orbitals enjoy a wide range of applications in quantum-chemical approaches to interacting quantum systems [22–24, 70], and their use can also be extended to a systematic approximation by a series of Slater determinants [71, 72].

While it may be possible to utilise analytical methods to construct these orbitals for smaller systems with fewer fermions, this becomes an impossibly difficult task for even slightly larger systems where $N > 2$. There is more than one way to construct these orbitals numerically; however, we should turn our attention to methods in which the overlap increases monotonously with the number of iterations in order to be sure that the Brueckner orbitals are at least close to optimal. One possible way of doing this involves the optimisation of one single-particle orbital at a time, thus ensuring monotonous improvement of the overlap as the number of iterations is increased. A detailed review of a generalised process for constructing M orbitals which maximise the overlap $\mathcal{I}_n$ can

be found in Ref. [71] and also appendix A.2; however, it should be noted that we solely concern ourselves with the special case of $M = N$ here.

2.3.4 Projecting onto a Single-Particle Space

We have now defined two types of candidate single-particle orbitals in the form of the natural orbitals of the OPDM, and also the Brueckner orbitals which maximise overlap with a single Slater determinant. In general, these two sets of single-particle orbitals can be very different to one another. In particular, when the overlap is moderate or small, the differences are very easily seen by noting that—for a given many-body eigenstate $|\psi_n\rangle$—there are L corresponding natural orbitals $\{\phi_\alpha^{(n)}\}_{\alpha=1}^{L}$, whereas there are only N Brueckner orbitals $\{\chi_\alpha^{(n)}\}_{\alpha=1}^{N}$. The two sets of orbitals can be so different, that constructing the Bruckner orbitals from the—more easily obtained—OPDMs can prove to be a very numerically unfavourable task [70–72].

We can therefore surmise that the natural orbitals span a larger space, and this is relatively unsurprising, as the natural orbitals can be thought of as a many-body extension of the noninteracting case where all states are exactly representable as Slater determinants. However, as we discussed in section 2.2, the many-body localised regime is characterised by a spontaneous emergent integrability, and this has dramatic consequences on the nature of natural orbitals. In particular, as stated in section 2.3.1, the natural orbitals will start to reflect single-particle-like behaviour in the localised regime, and will thus display more defined occupations $n_\alpha \to 0$ or 1. This emergent order out of chaos reduces the span of the single-particle sector, and results in a reduction in the number of natural orbitals $L \to N$, which signals the formation of a distinct basis of l-bit quasiparticle operators. As the natural orbitals undergo a notable transformation, so do the Brueckner orbitals, in that they will increasingly become better approximations of the many-body eigenstates, signified by a unity-approaching overlap $\mathcal{I}_m \to 1$. Concurrently, the OPDMs will become more projector-like in nature $\rho_m \to P_m$, where the projectors can be explicitly written as $(P_m)_{ij} = \langle S_m|c_i^\dagger c_j|S_m\rangle$. These general observations indeed apply well to individual eigenstates inside the many-body-localised regime [25–27], which we will expand on in later sections.

If we observe the new emergent structure of many-body localised natural orbitals and compare them to the, now more accurate, Brueckner orbitals, we can see that they

now span the same single-particle space, as they are now both sets of N L-dimensional orbitals which must uniquely characterise a given many-body eigenstate. In fact, in the case of perfect localisation $n_\alpha \in \{0, 1\}$, the natural orbitals are completely identical to the Brueckner orbitals, provided that the Brueckner orbitals are properly orthogonalised. In noninteracting systems, the single-particle eigenstates are known to provide a joint set from which one can choose the Brueckner orbitals; however, it is presumptuous to assume the same for the case of finite interactions. In general, such a single-particle basis is not at all guaranteed by the mere requirement that the corresponding many-body Slater determinants are orthogonal to each other. This can be summarised by the following statement: *Even when two (or perhaps all) eigenstates of an interacting system are exact Slater determinants, this does not guarantee that there is a common single-particle basis from which one can form the Brueckner orbitals of these eigenstates.* This is the observation that gave rise to question 2 in section 2.2.

Indeed, it is easy to quantify and detect this *orbital incompatibility*, as it can be established already on the level of pairs of many-body eigenstates $|\psi_l\rangle$ and $|\psi_m\rangle$. When the orbitals of both states are compatible with each other, their projectors, P_l and P_m, commute. We therefore introduce the following incompatibility measure,

$$\mathcal{C}_{ml} \equiv \sqrt{\mathrm{tr}\,[P_l, P_m][P_m, P_l]} = \sqrt{2\mathrm{tr}\,(P_l P_m - (P_l P_m)^2)}, \tag{2.7}$$

which mathematically corresponds to the Frobenius norm of the commutator of both projectors. As the projectors P_m characterise N-dimensional subspaces in the single-particle Hilbert space H_1—mathematically, the Grassmannian $G(H_1, N)$—this provides us with a simple geometric picture of the interrelation between different wavefunctions of a given MBL system.

2.4 A Deeper Look into Orbital Incompatibility

Previously, in section 2.3.4, we established a measure of incompatibility between two projectors; however, the incompatibility measure is also applicable directly to the OPDM corresponding to a many-body eigenstate. The general incompatibility measure will therefore be defined as

$$\|[\rho_n, \rho_m]\| \equiv \sqrt{\mathrm{tr}\,[\rho_n, \rho_m][\rho_m, \rho_n]}. \tag{2.8}$$

The reason Eq. (2.8) can be used as a measure of incompatibility can be seen more clearly by explicitly presenting the OPDM in its diagonal basis $\rho_n = U_n D_n U_n^\dagger$, where D_n is the diagonal matrix of occupations, and U_n is the matrix of natural orbitals fulfilling $U_n^\dagger U_n = \mathbb{1}$. If we assume that any given pair of OPDMs are constructed from the same natural orbitals, then this allows us to set $U_n = U_m = U$ and thus rewrite Eq. (2.8) as

$$\begin{aligned}[\rho_n, \rho_m] &= \left[U D_n U^\dagger, U D_m U^\dagger\right] \\ &= U[D_n, D_m]U^\dagger \\ &= \mathbf{0}. \end{aligned} \tag{2.9}$$

It is clear from Eq. (2.9) that any two OPDMs which share the same natural orbitals will commute, resulting in an incompatibility measure of zero. Such orbitals are said to be "compatible". Conversely, if the compatibility measure is non-zero, then the orbitals are said to be "incompatible". If all OPDMs were to be constructed from the same basis of natural orbitals, then it would follow that the compatibility measure would be zero for all pairs of eigenstates, thus immediately affirming both questions asked in section 2.2 with a resounding "yes"; however, there is no reason to believe that this is necessarily the case.

2.4.1 A Tight Lower Bound

We justify our compatibility measure by establishing that it possesses a strict lower bound of zero. From our definition of the OPDM in Eq. (2.2), it is readily seen that the OPDM is Hermitian, which is to say that $\rho_n = (\rho_n)^\dagger$. Using this property, we find that

$$\begin{aligned}[\rho_n, \rho_m]^\dagger &= (\rho_n \rho_m)^\dagger - (\rho_m \rho_n)^\dagger \\ &= (\rho_m)^\dagger (\rho_n)^\dagger - (\rho_n)^\dagger (\rho_m)^\dagger \\ &= \rho_m \rho_n - \rho_n \rho_m \\ &= -[\rho_n, \rho_m], \end{aligned} \tag{2.10}$$

and thus is anti-Hermitian. Therefore, the product of commutators in Eq. (2.8) can also be written as

$$\begin{aligned}[\rho_n, \rho_m][\rho_m, \rho_n] &= -[\rho_n, \rho_m][\rho_n, \rho_m] \\ &= [\rho_n, \rho_m]^\dagger [\rho_n, \rho_m] \\ &\equiv A_{nm}^\dagger A_{nm}. \end{aligned} \tag{2.11}$$

Eq. (2.11) informs us that Eq. (2.8) is simply the *Frobenius norm* of $[\rho_n, \rho_m]$. It is readily seen that Eq. (2.11) is Hermitian, since $(A^\dagger_{nm}A_{nm})^\dagger = A^\dagger_{nm}A_{nm}$. Moreover, we can conclude that

$$\mathbf{v}^\dagger A^\dagger_{nm}A_{nm}\mathbf{v} = (A_{nm}\mathbf{v})^\dagger (A_{nm}\mathbf{v}) \geq 0 \quad \forall\ \mathbf{v}. \tag{2.12}$$

Since Eq. (2.12) is true for all vectors, including eigenvectors, this signifies that all of the eigenvalues of $A^\dagger_{nm}A_{nm}$ are non-negative, and thus $\operatorname{tr} A^\dagger_{nm}A_{nm} \geq 0$. By substituting Eq. (2.11) into Eq. (2.8), and imposing the condition described in Eq. (2.12), we can now state

$$\|[\rho_n, \rho_m]\| \begin{cases} = 0 & \text{if } \rho_n = UD_nU^\dagger \quad \forall\ n \\ \geq 0 & \text{otherwise} \end{cases} \tag{2.13}$$

We have now proven that the compatibility measure described in Eq. (2.8) is greater than or equal to zero, and is always exactly zero when the OPDMs are constructed from the same single-particle orbitals; therefore, Eq. (2.8) is a valid measure of compatibility.

2.4.2 A Naive Upper Bound

The compatibility measure is also subject to a mathematical upper bound, implying that there exists a theoretical maximal incompatibility. In order to derive such a bound, we begin by rewriting the definition of the compatibility measure as

$$\begin{aligned} \|[\rho_n, \rho_m]\| &\equiv \sqrt{\operatorname{tr}\left[\rho_n, \rho_m\right]\left[\rho_m, \rho_n\right]} \\ &= \sqrt{2\operatorname{tr}(\rho_n)^2(\rho_m)^2 - 2\operatorname{tr}(\rho_n\rho_m)^2}. \end{aligned} \tag{2.14}$$

We note that $\operatorname{tr}(\rho_n)^2(\rho_m)^2$ belongs to an inner product space. This is easily confirmed by verifying the following properties for all n and m:

1. $\operatorname{tr}(\rho_n)^2(\rho_m)^2 = \operatorname{tr}^*(\rho_n)^2(\rho_m)^2$,
2. $\operatorname{tr}\big[(\rho_n)^2 + C\big](\rho_m)^2 = \operatorname{tr}(\rho_n)^2(\rho_m)^2 + \operatorname{tr} C(\rho_m)^2$,
3. $\operatorname{tr}(\rho_n)^2(\rho_n)^2 > 0$.

The first point can be proved by noting that the $\{\rho_n\}$ are real matrices, thus the trace of products of them will always be a real number. The second point is automatically satisfied by the properties of the trace. The third point can be addressed by recalling that $\operatorname{tr}\rho_n = N > 0$, thus immediately implying that $\operatorname{tr}(\rho_n)^4 > 0$ since the $\{\rho_n\}$ are real matrices.

Since we are dealing with an inner product space, we can now use the Cauchy-Schwarz identity to place an upper bound on the quantity

$$\begin{aligned}\mathrm{tr}(\rho_n)^2(\rho_m)^2 &\leq \sqrt{\mathrm{tr}(\rho_n)^4\,\mathrm{tr}(\rho_m)^4} \\ &\leq \sqrt{\mathrm{tr}(\rho_n)^2\,\mathrm{tr}(\rho_m)^2} \\ &= \sqrt{\mathcal{P}_n\mathcal{P}_m}. \end{aligned} \tag{2.15}$$

If we additionally note that $\mathrm{tr}(\rho_n\rho_m)^2 > 0$, then, by making use of Eq. (2.15), we can reformulate Eq. (2.14) as

$$\|[\rho_n,\rho_m]\| \leq \sqrt{2}\,(\mathcal{P}_n\mathcal{P}_m)^{\frac{1}{4}} \leq \sqrt{2N}. \tag{2.16}$$

The minimal purity of a given OPDM is given by N^2/L; therefore, provided that $N^2/L > 1$, Eq. (2.16) will be stronger than the Böttcher-Wenzel inequality, which produces an upper bound of $\sqrt{2P_nP_m} \leq \sqrt{2}N$.

2.4.3 Justifying the Compatibility Measure

Thus far, we have provided convincing arguments that our choice of compatibility measure fulfils its purpose in the most extremal cases, in that it is bounded by zero for perfect compatibility and possesses a finite mathematical upper bound. However, we have yet to expound on a necessary critique: is it a viable measure of compatibility between the extremal cases of perfect localisation and total ergodicity?

A convincing argument can be formulated as follows. We know from section 2.4.1 that the compatibility measure can be written compactly as $\|[\rho_n,\rho_m]\| = \sqrt{-\mathrm{tr}\,[\rho_n,\rho_m]^2}$, where we proved $[\rho_n,\rho_m]$ to be an anti-Hermitian matrix. For convenience, let us use the notation $[\rho_n,\rho_m]\,|\phi_i^{nm}\rangle = i\lambda_i^{nm}\,|\phi_i^{nm}\rangle$, where $\lambda_i^{nm} \in \mathbb{R}$ as the eigenvalues of an anti-Hermitian matrix are necessarily purely imaginary. It is then trivially seen that the compatibility measure can be written as

$$\|[\rho_n,\rho_m]\| = \sqrt{\sum_{i=1}^{L}(\lambda_i^{nm})^2}. \tag{2.17}$$

It is readily seen that if there exists a shared natural orbital $|\phi_i^{nm}\rangle$ between two given OPDMs, then it is also an eigenvector of the commutator between them, subject to $[\rho_n,\rho_m]\,|\phi_i^{nm}\rangle = \mathbf{0}$, and thus directly implying $\lambda_i^{nm} = 0$ for each shared natural orbital between ρ_n and ρ_m. Turning our attention back to Eq. (2.17), we can see that applying

this implies that the compatibility measure will fall precipitously to zero as more and more orbitals are shared between any two given OPDMs. By the simple reversal of this statement, we can also say that the compatibility measure will rise as fewer orbitals are shared.

2.4.4 A Random Matrix Benchmark

To provide further insight, we now turn to the special case of incompatible projectors in the ergodic regime—a regime in which the OPDMs ρ typically differ greatly from the projectors P. To determine how sizeable the numerically observed orbital incompatibility of MBL states is, we compare it to the extreme case of two random Slater determinants, $|S_m\rangle$ and $|S_l\rangle$, with mutually uncorrelated projectors, P_m and P_l, admitting for additional generality that they may represent states of possibly different particle number, N and N'. As before, we denote the dimensionality of the single-particle Hilbert space as L.

We set out to obtain a compact result for the averaged[4] squared incompatibility,

$$\overline{\mathcal{C}^2_{ml}} = 2\,\mathrm{tr}\,\overline{P_m P_l} - 2\,\mathrm{tr}\,\overline{P_m P_l P_m P_l} \tag{2.18}$$

$$= 2\,\mathrm{tr}\,\overline{(P_l P_m P_l)} - 2\,\mathrm{tr}\,\overline{(P_l P_m P_l)^2}, \tag{2.19}$$

where the expression in the second line exploits that any projector fulfils $P_l^2 = P_l$. This is useful, as for any pair of states, we can adopt a single-particle basis in which P_l is diagonal and projects onto the first N states of the basis. In this basis, the combination

$$P_l P_m P_l = \begin{pmatrix} X & 0 \\ 0 & 0 \end{pmatrix} \tag{2.20}$$

appearing in Eq. (2.19) has a finite subblock X of size $N \times N$, and in terms of this

$$\overline{\mathcal{C}^2_{ml}} = 2\,\mathrm{tr}\,\overline{X} - 2\,\mathrm{tr}\,\overline{X^2}, \tag{2.21}$$

where the trace is now of matrices of size N.

Diagonalising P_m in this basis, we can further write $(P_m)_{rs} = \sum_{n=1}^{N'} U_{rn} U^*_{sn}$, where the columns of the unitary matrix U are the orthonormalised eigenstates of P_m, and the sum runs over the N' eigenstates with eigenvalue 1 (the remaining eigenvalues vanish). Therefore, $X = uu^\dagger$ be further written in terms of a rectangular $N \times N'$-dimensional

[4] All disorder-averaged quantities are indicated with overbar notation i.e. $\overline{A}$ is the mean average of A from many disorder realisations.

subblock u of the $L \times L$-dimensional unitary matrix U. We then have to calculate

$$\overline{\mathcal{C}_{ml}^2} = 2\,\mathrm{tr}\,\overline{uu^\dagger} - 2\,\mathrm{tr}\,\overline{(uu^\dagger)^2}. \tag{2.22}$$

In random-matrix theory, we can evaluate these averages using a standard ensemble. Here we consider two cases, systems with real orbitals and systems with complex orbitals. For the case of real orbitals, we take U to be uniformly distributed over the orthogonal group $O(L)$, which is also known as the circular real ensemble (CRE; distinct from the circular orthogonal ensemble in which $U = U^T$ is still complex) [73]. For the case of complex orbitals, we take U to be uniformly distributed over the unitary group $U(L)$, which corresponds to the standard circular unitary ensemble (CUE). In both ensembles, all matrix elements of U are equivalent, which allows us to decompose the averaged traces

$$\mathrm{tr}\,\overline{uu^\dagger} = NN'A, \tag{2.23}$$

$$\mathrm{tr}\,\overline{(uu^\dagger)^2} = NN'[B + (N + N' - 2)C + (N - 1)(N' - 1)D] \tag{2.24}$$

of the truncated matrices into a small number of fundamental terms,

$$A \equiv \overline{|u_{rs}|^2}, \quad B \equiv \overline{|u_{rs}|^4}, \tag{2.25}$$

$$C \equiv \overline{|u_{rs}|^2|u_{rt}|^2} = \overline{|u_{sr}|^2|u_{tr}|^2} \quad (s \neq t), \tag{2.26}$$

$$D \equiv \overline{u_{rs}u_{ps}^* u_{pt}u_{rt}^*} \quad (r \neq p, s \neq t), \tag{2.27}$$

where unspecified indices are unconstrained. The same equivalence of matrix elements also implies the following sum rules,

$$\mathrm{tr}\,\overline{UU^\dagger} = L^2A = L, \tag{2.28}$$

$$\mathrm{tr}\,\overline{(UU^\dagger)^2} = L^2B + 2L^2(L - 1)C + L^2(L - 1)^2D = L, \tag{2.29}$$

$$\overline{[(UU^\dagger)_{11}]^2} = LB + L(L - 1)C = 1. \tag{2.30}$$

These expressions can all be combined to express the desired average as

$$\overline{\mathcal{C}_{ml}^2}|_{\mathrm{RMT}} = -2DNN'(L - N)(L - N'). \tag{2.31}$$

Averages such as the ones presented above also appear in quantum transport, where u would be interpreted as a block of a scattering matrix and the given combinations determine, for instance, universal conductance fluctuations and shot noise [74]. Furthermore, such averages also appear in the dynamics of quantum-chaotic systems, where U represents a time-evolution operator [75], while truncated versions appear in the description of

leaky systems [76] and in Floquet-descriptions of quantum transport [77]. Here, A and B can be worked out by interpreting them as moments of a coordinate from a random L-dimensional unit vector, parametrised in hyperspherical coordinates, thereby relating it to integrals of the form

$$I_{n,m} = \int_0^\pi \cos^n(\varphi) \sin^m(\varphi) d\varphi, \tag{2.32}$$

while C and D then follow from the given sum rules. In the CRE, we then have

$$A = \frac{I_{2,L-2}}{I_{0,L-2}} = \frac{1}{L}, \tag{2.33}$$

$$B = \frac{I_{4,L-2}}{I_{0,L-2}} = \frac{3}{L(L+2)}, \tag{2.34}$$

$$C = \frac{1}{L(L+2)}, \tag{2.35}$$

$$D = -\frac{1}{(L-1)L(L+2)}, \tag{2.36}$$

while in the CUE we have

$$A = 2\frac{I_{2,2L-2}}{I_{0,2L-2}} = \frac{1}{L}, \tag{2.37}$$

$$B = 2\frac{I_{4,2L-2}}{I_{0,2L-2}} + 2\frac{I_{2,2L} I_{2,2L-3}}{I_{0,2L-2} I_{0,2L-3}} = \frac{2}{L(L+1)}, \tag{2.38}$$

$$C = \frac{1}{L(L+1)}, \tag{2.39}$$

$$D = -\frac{1}{L(L^2-1)}. \tag{2.40}$$

(In both cases, A also follows from the given sum rule, and they can be related to each other using $B|_{\mathrm{CUE}(L)} = 2[B|_{\mathrm{CRE}(2L)} + C|_{\mathrm{CRE}(2L)}]$.)

Therefore, as our final results, we obtain

$$\overline{\mathcal{C}_{ml}^2}|_{\mathrm{RMT}} = \frac{2NN'(L-N)(L-N')}{(L-1)L(L+2)} \quad \text{(CRE)} \tag{2.41}$$

for the averaged squared incompatibility of random Slater determinants with real orbitals, and

$$\overline{\mathcal{C}_{ml}^2}|_{\mathrm{RMT}} = \frac{2NN'(L-N)(L-N')}{L(L^2-1)} \quad \text{(CUE)} \tag{2.42}$$

for the case of complex orbitals. For large systems near half filling, both expressions approach $\overline{\mathcal{C}_{ml}^2}|_{\mathrm{RMT}} \sim L/8 \equiv C_0^2$. Level repulsion between the eigenvalues of X then guarantees that fluctuations about this value are suppressed [74]. Therefore, C_0 not only characterises the squared incompatibility, but can be used as a benchmark for the incom-

patibility $\mathcal{C}_{ml}$ itself.

2.5 A Paradigmatic Model

Due to the necessity of accurate eigendecompositions for dynamical analysis, we are typically constrained to one-dimensional lattice models. In particular, there is a notable choice that has become a well-studied model in the study of many-body localisation: the random-field Heisenberg spin chain. However, since our key questions revolve around the connection between noninteracting localised particles and l-bits—the many-body analogue spontaneously emergent in the many-body localised regime—it makes sense to choose a model that allows for the continuous introduction of finite interactions. Taking this need into account, this leaves us with a paradigmatic model[5] that is closely related to the aforementioned random-field Heisenberg model: the $S = 1/2$ XXZ spin chain in a random field

$$H_{\mathrm{XXZ}} = t\left[\sum_{i=1}^{L}\left(S_i^x S_{i+1}^x + S_i^y S_{i+1}^y + \Delta S_i^z S_{i+1}^z\right) - \sum_{i=1}^{L} h_i S_i^z\right], \tag{2.43}$$

where Δ allows for the continuous addition of finite density-density interactions and h represents onsite interactions which can be chosen randomly to introduce disorder into the model. The entire Hamiltonian is expressed in units of the nearest-neighbour hopping constant t; therefore, all other parameters are defined to be unitless [25]. We can therefore, with no loss of generality, set $t = 1$ for convenience, thus simplifying the form of the Hamiltonian.

In order to explore the various properties of the many-body localised phase from a single-particle perspective, we can apply a *Jordan-Wigner transformation* to Eq. (2.43), thus producing a model consisting of N spinless fermions confined to a one-dimensional lattice with L atomic sites. This new formulation will possess $\mathcal{N} = \binom{L}{N}$ uniquely distinct states, which is used to form a basis labelled according to the configuration of occupied and unoccupied sites. Each basis state is labelled as $|X\rangle \equiv |n_1, n_2, \ldots, n_L\rangle$, where each given n_i represents the occupation of site i, and can be either one or zero, representing an occupied or unoccupied atomic site respectively.

In the system we have described, we set the energy scale by introducing a shift, $n_i \to n_i - 1/2$, thus ensuring that partial filling of atomic sites will centre the spectrum roughly

[5] It is worth noting that Eq. (2.43) is actually a generalisation of the random-field Heisenberg model, as the latter is retrieved simply by setting interactions to $\Delta = 1$.

about $E = 0$. Since the occupation of each site can only be one or zero in our model, this produces the more specific properties: $c_i |0_i\rangle = 0$, and $c_i^\dagger |1_i\rangle = 0$. Using this notation, our Hamiltonian will take the form:

$$H = -\frac{1}{2}\sum_{i=1}^{L}\left(c_i^\dagger c_{i+1} + \text{h.c.}\right) + \sum_{i=1}^{L}\epsilon_i\left(n_i - \frac{1}{2}\right) + V\sum_{i=1}^{L}\left(n_i - \frac{1}{2}\right)\left(n_{i+1} - \frac{1}{2}\right). \quad (2.44)$$

where $n_i = c_i^\dagger c_i$ denotes the number operator[6] for site i. The parameters, ϵ_i and V, respectively denote the on-site potential at site i, and the repulsive interaction strength between adjacent sites. From the form of the Hamiltonian, we can see that only nearest-neighbour "hoppings" are allowed (e.g. $|1000\rangle \to |0100\rangle$ is allowed, whereas $|1000\rangle \to |0010\rangle$ is forbidden); and in addition, we employ periodic conditions, such that $c_{i+1} \equiv c_{(i \bmod L)+1}$, therefore allowing transitions from the last atomic site to the first atomic site and vice-versa[7].

It can be seen from the Hamiltonian defined in Eq. (2.44) that the interaction term (with prefactor V) is dependent on the occupations of adjacent atomic sites and explicitly connects the model with Anderson localisation—as the noninteracting case $V = 0$ corresponds to a free-particle model in a random potential. However, the on-site potentials $\{\epsilon_i\}$, can be chosen freely. The importance of the onsite potentials cannot be overstated, since the entire many-body localisation transition is encoded into the way we introduce disorder into said onsite potentials. There exist a few different studies into various forms of disorder; the most-studied distributions of the $\{\epsilon_i\}$ being: the box distribution with ϵ_i uniformly distributed in the range $[-W, W]$, the bimodal distribution $\epsilon_i \in \{-W, W\}$ with corresponding probabilities $\{P, (1-P)\}$ [79, 80], and the quasi-periodic case $\epsilon_i = \epsilon\cos(2\beta\pi i)$ where β is an irrational number[8] [82–84]. Here, we choose to study our questions using the most general of the disorder distributions: the uniform box distribution.

2.5.1 Making the Basis Explicit

Since we have utilised second quantisation notation to construct the Hamiltonian, we must explicitly represent our basis states using the same notation in order to avoid ambiguity.

[6] One could also make the transformation $n_i \to n_i + n_{\text{shift}}$ where $n_{\text{shift}} \in \mathbb{R}$ with no loss of generality. This is because we can arbitrarily shift the zero of the Hamiltonian without affecting the relative differences between quantities.

[7] It is worth noting that the choice of boundary condition can be tailored to our needs; for example, we could also consider "open" boundary conditions where $c_{L+1} |X\rangle = 0$.

[8] This model—in the special case of zero interactions $V = 0$—corresponds to the well-studied Aubry-André model [81].

Let $X \equiv (x_1, x_2, \ldots, x_N)$ denote an ordered N-tuple subject to the constraint $(1 \leq x_1 < x_2 < \ldots < x_N \leq L)$ where $\{x_i \in \mathbb{Z} | 1 \leq x_i \leq L\}$. Using this notation, we can uniquely define a given basis state as

$$|X\rangle \equiv c^\dagger_{x_1} c^\dagger_{x_2} \ldots c^\dagger_{x_N} |\text{vac}\rangle \,, \tag{2.45}$$

and a given many-body eigenstate can be written as

$$|\psi_n\rangle \equiv \sum_{x_1<x_2<\ldots<x_N} \psi_n(x_1, x_2, \ldots, x_N) c^\dagger_{x_1} c^\dagger_{x_2} \ldots c^\dagger_{x_N} |\text{vac}\rangle \,, \tag{2.46}$$

where $|\psi_n\rangle$ represents the nth many-body eigenstate, and $\psi(x_1, x_2, \ldots, x_N) \equiv \psi(X)$ represents the amplitude of a particular basis state. Note that Eqs. (2.45) and (2.46) are also subject to the normalisation conditions $\langle n|m\rangle = \delta_{nm}$ and $\langle \psi_n | \psi_m \rangle = \sum_{X=1}^{\mathcal{N}} \psi^*_n(X)\psi_m(X) = \delta_{nm}$ respectively.

In order to maintain consistency, the $\{x_i\}$ in $c^\dagger_{x_1} c^\dagger_{x_2} \ldots c^\dagger_{x_N}$ can be interpreted as the exponents of a base-2 (binary) number, written as $2^{x_1-1} + 2^{x_2-1} + \ldots + 2^{x_N-1}$. This interpretation allows one to order the basis states in ascending order, which will be utilised here[9]. For example, $|1\rangle \equiv c^\dagger_1 c^\dagger_2 \ldots c^\dagger_N |\text{vac}\rangle$ and $|\mathcal{N}\rangle \equiv c^\dagger_{L-N+1} c^\dagger_{L-N+2} \ldots c^\dagger_L |\text{vac}\rangle$. Using the ordering system defined here, we can explicitly write the Hamiltonian operator as an $\mathcal{N} \times \mathcal{N}$ matrix, and the unitary transformation which diagonalises the Hamiltonian matrix as $H = \Psi D_H \Psi^\dagger$ can be written as

$$\Psi = \begin{pmatrix} \psi_1(1) & \psi_2(1) & \ldots & \psi_{\mathcal{N}}(1) \\ \psi_1(2) & \psi_2(2) & \ldots & \psi_{\mathcal{N}}(2) \\ \vdots & \vdots & \ddots & \vdots \\ \psi_1(\mathcal{N}) & \psi_2(\mathcal{N}) & \ldots & \psi_{\mathcal{N}}(\mathcal{N}) \end{pmatrix}, \tag{2.47}$$

where each column corresponds to a given many-body eigenstate, and each row corresponds to particular basis state. This matrix of eigenvectors, along with the corresponding diagonal matrix of eigenvalues, can be obtained numerically via the exact diagonalisation of the Hamiltonian matrix.

[9]Note that either descending or ascending order is acceptable, the latter of which is known as *lexographic ordering*.

2.6 An Illustrative Analytical Solution

2.6.1 A Minimal Special Case

To explain how the quasiparticle dressing arises, we provide a complete analytical solution of a minimal model, representing on a small system of $L = 4$ sites with a particular disorder configuration $\varepsilon_1 = \varepsilon_3$, $\varepsilon_2 = \varepsilon_4$ (approximate disorder configurations of this type will be present generically in sufficiently long systems; however, for the analytical treatment we apply periodic boundary conditions). Shifting energies such that $\varepsilon \equiv \varepsilon_1 = \varepsilon_3 = -\varepsilon_2 = -\varepsilon_4$, we can rewrite the Hamiltonian as

$$\begin{aligned} H = &- (d_1^\dagger d_2 + d_2^\dagger d_1) + \varepsilon[n_1' - n_2' + n_3' - n_4'] \\ &+ V[(n_1' + n_3')(n_2' + n_4') - \sum_i n_i' + 1], \end{aligned} \tag{2.48}$$

where we change the single-particle basis to

$$d_1^\dagger = \frac{c_1^\dagger + c_3^\dagger}{\sqrt{2}}, \;\; d_2^\dagger = \frac{c_2^\dagger + c_4^\dagger}{\sqrt{2}}, \;\; d_3^\dagger = \frac{c_1^\dagger - c_3^\dagger}{\sqrt{2}}, \;\; d_4^\dagger = \frac{c_2^\dagger - c_4^\dagger}{\sqrt{2}} \tag{2.49}$$

and denote the corresponding densities as $n_i' = d_i^\dagger d_i$.

One wonderful property that makes this construction an instructive special case, is that while there are L single-quasiparticle operators, only $L/2$ are required to fully represent the hopping part of the Hamiltonian. Since this part comprises the only non-diagonal terms, then this allows us to trivially deduce—in the subspace of $N = 2$ particles—the form of two of the Hamiltonian's eigenvectors immediately, as they send the hopping term to zero. These two eigenvectors are of the form $|1\rangle = d_1^\dagger d_2^\dagger |\text{vac}\rangle$ and $|2\rangle = d_3^\dagger d_4^\dagger |\text{vac}\rangle$. These are simply deduced as $(d_1^\dagger d_2 + d_2^\dagger d_1) d_1^\dagger d_2^\dagger |\text{vac}\rangle = (d_1^\dagger d_2 + d_2^\dagger d_1) d_3^\dagger d_4^\dagger |\text{vac}\rangle = 0$ due to the number of creation and annihilation operators in each product state differing by more than one for at least one site. In addition to this, the rest of the Hamiltonian being diagonal means that we can easily confirm, without much calculation, that $H d_1^\dagger d_2^\dagger |\text{vac}\rangle = H d_3^\dagger d_4^\dagger |\text{vac}\rangle = 0$. We also note that the product-state form of these eigenvectors also implies that they are exact Slater determinants.

The other eigenvectors, however, are not as easily deduced, but they turn our to be exact Slater determinants also. We can make their calculation simple and explicit by defining a basis and representing Eq. (2.48) as a matrix. As in section 2.5.1, we order the basis states in the standard computational way, by ordering them in ascending order as if

they were binary numbers. Utilising this ordering, we can write the matrix representation

$$S(X) = \begin{pmatrix} 0 & 0 & 0 & 0 & 0 & 0 \\ 0 & -(2\varepsilon + V) & 0 & -1 & 0 & 0 \\ 0 & 0 & 0 & 0 & -1 & 0 \\ 0 & -1 & 0 & 0 & 0 & 0 \\ 0 & 0 & -1 & 0 & 2\varepsilon - V & 0 \\ 0 & 0 & 0 & 0 & 0 & 0 \end{pmatrix} \tag{2.50}$$

A notable property of the matrix above is the fact that two of the rows and columns contain only zeroes. These are a direct result of the two zero-eigenvalue eigenvectors that we previously deduced. We can therefore, without loss of generality, reduce our matrix to a smaller one of the form

$$S(X) = \begin{pmatrix} -(2\varepsilon + V) & 0 & -1 & 0 \\ 0 & 0 & 0 & -1 \\ -1 & 0 & 0 & 0 \\ 0 & -1 & 0 & 2\varepsilon - V \end{pmatrix} \tag{2.51}$$

The eigenvectors of this matrix can be formulated as ansatzes that exploit its simple structure. Namely, the eigenvectors will be four-dimensional vectors with exactly two nonzero elements. If we delay normalisation until the final analysis, we can write these eigenvectors quite simply as

$$\begin{aligned} |3\rangle &\cong (0, -1, 0, \alpha), \\ |4\rangle &\cong (0, \alpha, 0, 1), \\ |5\rangle &\cong (-1, 0, \beta, 0), \\ |6\rangle &\cong (\beta, 0, 1, 0), \end{aligned} \tag{2.52}$$

It is trivial to verify that these vectors are indeed orthogonal to each other, and thus satisfy the necessary conditions for them to be suitable candidate eigenvectors. The next task is a purely algebraic one, in that we can calculate the values of α and β by simply subjecting them to the definition of an eigenvector, $H|\psi\rangle = E|\psi\rangle$, and solving the resulting simultaneous equations that arise. It is perhaps of little surprise that the form of α and β are reminiscent of the solutions to a quadratic equation. The full set of eigenstates and

associated eigenenergies , normalised and rewritten in second quantisation notation—in the interacting subspace of $N = 2$ particles—are thus of the form

$$\begin{aligned}
|1\rangle &= d_1^\dagger d_2^\dagger |\text{vac}\rangle, \quad |2\rangle = d_3^\dagger d_4^\dagger |\text{vac}\rangle \quad (E_{1,2} = 0),\\
|3\rangle &= \frac{1}{\sqrt{1+\alpha^2}} (\alpha d_1^\dagger - d_2^\dagger) d_3^\dagger |\text{vac}\rangle \quad (E_3 = \alpha),\\
|4\rangle &= \frac{1}{\sqrt{1+\alpha^2}} (d_1^\dagger + \alpha d_2^\dagger) d_3^\dagger |\text{vac}\rangle \quad (E_4 = -1/\alpha),\\
|5\rangle &= \frac{1}{\sqrt{1+\beta^2}} (\beta d_1^\dagger - d_2^\dagger) d_4^\dagger |\text{vac}\rangle \quad (E_5 = 1/\beta),\\
|6\rangle &= \frac{1}{\sqrt{1+\beta^2}} (d_1^\dagger + \beta d_2^\dagger) d_4^\dagger |\text{vac}\rangle \quad (E_6 = -\beta),
\end{aligned} \tag{2.53}$$

where $|\text{vac}\rangle$ denotes the state without any particles and

$$\begin{aligned}
\alpha &= (\varepsilon - V/2) + \sqrt{1 + (\varepsilon - V/2)^2},\\
\beta &= (\varepsilon + V/2) + \sqrt{1 + (\varepsilon + V/2)^2}.
\end{aligned} \tag{2.54}$$

Notably, these states are all exact Slater determinants, but their form already suggests that they cannot be created from a common set of single-particle orbitals. To verify this feature, we identify the subspace of occupied orbitals in terms of the projectors P_m. In the single-particle basis (2.49), where $(P_m)_{ij} = \langle m | d_i^\dagger d_j | m \rangle$, this gives

$$\begin{aligned}
P_1 &= \begin{pmatrix} 1&0&0&0\\ 0&1&0&0\\ 0&0&0&0\\ 0&0&0&0 \end{pmatrix}, \quad P_2 = \begin{pmatrix} 0&0&0&0\\ 0&0&0&0\\ 0&0&1&0\\ 0&0&0&1 \end{pmatrix} \quad P_3 = \begin{pmatrix} \frac{\alpha^2}{1+\alpha^2} & -\frac{\alpha}{1+\alpha^2} & 0&0\\ -\frac{\alpha}{1+\alpha^2} & \frac{1}{1+\alpha^2} & 0&0\\ 0&0&1&0\\ 0&0&0&0 \end{pmatrix}\\
P_4 &= \begin{pmatrix} \frac{1}{1+\alpha^2} & \frac{\alpha}{1+\alpha^2} & 0&0\\ \frac{\alpha}{1+\alpha^2} & \frac{\alpha^2}{1+\alpha^2} & 0&0\\ 0&0&1&0\\ 0&0&0&0 \end{pmatrix} \quad P_5 = \begin{pmatrix} \frac{\beta^2}{1+\beta^2} & -\frac{\beta}{1+\beta^2} & 0&0\\ -\frac{\beta}{1+\beta^2} & \frac{1}{1+\beta^2} & 0&0\\ 0&0&1&0\\ 0&0&0&0 \end{pmatrix} \quad P_6 = \begin{pmatrix} \frac{1}{1+\beta^2} & \frac{\beta}{1+\beta^2} & 0&0\\ \frac{\beta}{1+\beta^2} & \frac{\beta^2}{1+\beta^2} & 0&0\\ 0&0&1&0\\ 0&0&0&0 \end{pmatrix}.
\end{aligned} \tag{2.55}$$

We now see that the projectors, P_3 and P_4, do not commute with the projectors, P_5 and P_6. The same is true in the original single-particle basis associated with the operators

$c_i^\dagger$, for which the projectors follow from a unitary transformation $UP_lU^\dagger$ with

$$U = \frac{1}{\sqrt{2}} \begin{pmatrix} 1 & 0 & 1 & 0 \\ 0 & 1 & 0 & 1 \\ 1 & 0 & -1 & 0 \\ 0 & 1 & 0 & -1 \end{pmatrix}. \tag{2.56}$$

In particular, any such single-particle basis change leaves the incompatibility measure (2.7), invariant.

Therefore, this minimal model provides an exact realisation of orbital incompatibility. Each projector uniquely identifies the corresponding Slater-determinant eigenstate up to an overall phase factor, but as the projectors do not commute, these Slater determinants cannot be built from a common set of single-particle orbitals [10].

Notably, despite the described orbital incompatibility, we can still identify mutually commuting conserved quantities, beyond the number operator $I_0 = n_1 + n_2 + n_3 + n_4$, that provide a complete set of quantum numbers to uniquely discriminate all states. Within the two-particle sector, a possible choice is

$$\begin{aligned} &I_1 = d_3^\dagger d_3, \quad I_2 = d_4^\dagger d_4, \\ &I_3 = \frac{1}{1+\alpha^2} d_3^\dagger d_3 (\alpha d_1^\dagger - d_2^\dagger)(\alpha d_1 - d_2) + \frac{1}{1+\beta^2} d_4^\dagger d_4 (\beta d_1^\dagger - d_2^\dagger)(\beta d_1 - d_2), \end{aligned} \tag{2.57}$$

each of which have eigenvalues 0 and 1, and thus qualify as bit-like conserved quantities. We note that I_3 displays explicit dressings with occupations $d_i^\dagger d_i$. These considerations can be extended to explicitly formulate such bit-like conserved quantities that are valid in all particle-number sectors, which exhibit an analogous dressing with occupation operators of single-particle orbitals. But before we explore this, we can squeeze more information out of our existing formulations by simply considering the effect of the many-body localisation transition on the l-bits.

2.6.2 The High-Disorder Limit

We can extend our understanding of the many-body localised case by taking the limit of large disorder in our minimal model—specifically, we take the limit of large ε. Applying the limit of large epsilon to Eq. (2.54), we find that the high-disorder limit produces simple linear behaviour $\alpha \approx \beta \sim 2\varepsilon$. If we now apply this to the eigenstates in Eq. (2.53), we

[10] The states, $|1\rangle$ and $|2\rangle$, are degenerate, but this cannot be used to remove this feature.

find that our alternate single-particle basis simply becomes the quasiparticle basis

$$\begin{aligned}
&|1\rangle = d_1^\dagger d_2^\dagger|\text{vac}\rangle, \quad |2\rangle = d_3^\dagger d_4^\dagger|\text{vac}\rangle \quad (E_{1,2} = 0),\\
&|3\rangle \sim d_1^\dagger d_3^\dagger|\text{vac}\rangle \quad (E_3 \sim 2\varepsilon),\\
&|4\rangle \sim d_2^\dagger d_3^\dagger|\text{vac}\rangle \quad (E_4 \sim -1/2\varepsilon),\\
&|5\rangle \sim d_1^\dagger d_4^\dagger|\text{vac}\rangle \quad (E_5 \sim 1/2\varepsilon),\\
&|6\rangle \sim d_2^\dagger d_4^\dagger|\text{vac}\rangle \quad (E_6 \sim -2\varepsilon).
\end{aligned} \tag{2.58}$$

From Eq. (2.58), we also see level repulsion weaken as the eigenvalues start to become more degenerate. We can also apply this very same large limit to the conserved quantities, which produces

$$\begin{aligned}
&I_1 = d_3^\dagger d_3, \quad I_2 = d_4^\dagger d_4,\\
&I_3 \sim (d_3^\dagger d_3 + d_4^\dagger d_4) d_1^\dagger d_1.
\end{aligned} \tag{2.59}$$

The conserved quantities are very clearly many-body-like in that at least one of them—namely, I_3—involves a sum of different quasiparticle densities. However, it is worth exploring the persistence of the quasiparticle transformation in the most general case, to which we now turn.

2.6.3 Explicit Construction of Quasiparticles

We here identify the exact form of quasiparticles for the minimal model of Sec. 2.6.1 across all particle-number sectors. These can be obtained by a unitary transformation

$$q_i^\dagger = U d_i^\dagger U^\dagger, \tag{2.60}$$

constrained by the requirement that the eigenstates in all particle-number sectors (including the vacuum state) can be written as

$$|n\rangle = \prod_{i \in I_n} q_i^\dagger |\text{vac}\rangle, \tag{2.61}$$

where $\{q_i^\dagger, q_j\} = \delta_{ij}$.

Using the exact form (2.53) of the eigenstates and eigenenergies, this unitary trans-

formation can be identified as

$$\begin{aligned} U = {} & n'_1 n'_2 + \bar{n}'_1 \bar{n}'_2 \\ & + (D_1^\dagger d_1 \bar{n}'_2 + D_2^\dagger d_2 \bar{n}'_1) \bar{n}'_3 \bar{n}'_4 \\ & + (D_1 d_1^\dagger n'_2 + D_2 d_2^\dagger n'_1) n'_3 n'_4 \\ & + (D_{13}^\dagger d_1 \bar{n}'_2 + D_{23}^\dagger d_2 \bar{n}'_1) n'_3 \bar{n}'_4 \\ & + (D_{14}^\dagger d_1 \bar{n}'_2 + D_{24}^\dagger d_2 \bar{n}'_1) \bar{n}'_3 n'_4, \end{aligned} \tag{2.62}$$

which features occupations $n'_i = 1 - \bar{n}'_i = d_i^\dagger d_i$, as well as additional single-particle operators

$$D_1^\dagger = \frac{1}{\sqrt{1+\gamma^2}} (\gamma d_1^\dagger - d_2^\dagger), \tag{2.63}$$

$$D_2^\dagger = \frac{1}{\sqrt{1+\gamma^2}} (d_1^\dagger + \gamma d_2^\dagger) \tag{2.64}$$

with $\gamma = \varepsilon + \sqrt{1+\varepsilon^2}$, and

$$D_{13}^\dagger = \frac{1}{\sqrt{1+\alpha^2}} (\alpha d_1^\dagger - d_2^\dagger), \tag{2.65}$$

$$D_{23}^\dagger = \frac{1}{\sqrt{1+\alpha^2}} (d_1^\dagger + \alpha d_2^\dagger), \tag{2.66}$$

$$D_{14}^\dagger = \frac{1}{\sqrt{1+\beta^2}} (\beta d_1^\dagger - d_2^\dagger), \tag{2.67}$$

$$D_{24}^\dagger = \frac{1}{\sqrt{1+\beta^2}} (d_1^\dagger + \beta d_2^\dagger) \tag{2.68}$$

with α and β as given in Eq. (2.54).

Utilising also the corresponding occupations, $N_i = 1 - \bar{N}_i = D_i^\dagger D_i$, the quasiparticle operators (2.60) follow as

$$q_1^\dagger = (n'_3 n'_4 + \bar{n}'_3 \bar{n}'_4) D_1^\dagger + n'_3 \bar{n}'_4 D_{13}^\dagger + \bar{n}'_3 n'_4 D_{14}^\dagger; \tag{2.69}$$

$$q_2^\dagger = (n'_3 n'_4 + \bar{n}'_3 \bar{n}'_4) D_2^\dagger + n'_3 \bar{n}'_4 D_{23}^\dagger + \bar{n}'_3 n'_4 D_{24}^\dagger \tag{2.70}$$

$$\begin{aligned} q_3^\dagger = {} & [n'_1 n'_2 + \bar{n}'_1 \bar{n}'_2 + (D_{23}^\dagger D_2 \bar{N}_1 + D_{13}^\dagger D_1 \bar{N}_2) \bar{n}'_4 \\ & + (\bar{N}_2 D_1^\dagger D_{14} + \bar{N}_1 D_2^\dagger D_{24}) n'_4] d_3^\dagger; \end{aligned} \tag{2.71}$$

$$\begin{aligned} q_4^\dagger = {} & [n'_1 n'_2 + \bar{n}'_1 \bar{n}'_2 + (D_{24}^\dagger D_2 \bar{N}_1 + D_{14}^\dagger D_1 \bar{N}_2) \bar{n}'_3 \\ & + (\bar{N}_2 D_1^\dagger D_{13} + \bar{N}_1 D_2^\dagger D_{23}) n'_3] d_4^\dagger. \end{aligned} \tag{2.72}$$

From these expressions, the densities $I_i = q_i^\dagger q_i$ then deliver the desired bit-like con-

served quantities. The two densities

$$I_1 = q_3^\dagger q_3 = d_3^\dagger d_3, \quad I_2 = q_4^\dagger q_4 = d_4^\dagger d_4 \tag{2.73}$$

take the simple form of a one-particle density. We furthermore have $I_3 + I_4 = d_1^\dagger d_1 + d_2^\dagger d_2$, so that $I_1 + I_2 + I_3 + I_4 = I_0$ is the number operator. The remaining combination reads

$$I_3 - I_4 = (N_1 - N_2)(n_3' n_4' + \bar{n}_3' \bar{n}_4') + (N_{13} - N_{23}) n_3' \bar{n}_4' + (N_{14} - N_{24}) \bar{n}_3' n_4'. \tag{2.74}$$

As anticipated, this is manifestly many-body-like, and displays a strong dressing with the particle-number occupations in various orbitals of the system. We refer to this as many-body-like since it is not the case that the quasiparticle densities are conserved; but rather, it is a sum of them that is conserved in the case of Eq. (2.74).

2.7 Numerical Results

2.7.1 Systematic Orbital Incompatibility

To establish the incompatibility of MBL states numerically, we first calculate the Brueckner orbitals for each many-body eigenstate in a given realisation [11], and determine from these the overlaps $\mathcal{I}_m$. We then order the states either by overlap $\mathcal{I}_m$ or energy E_m, and next perform the disorder averages of these quantities, as well as of the incompatibility measures $\mathcal{C}_{ml}$ for all pairs of eigenstates. All averages are carried out over 10^3 realisations.

The results of this procedure in a many-body localised system ($V = 1.5$, $W = 8$) of length $L = 14$ at half filling ($N = 7$) are shown in Fig. 2.2. In panels (a-c) the states are ordered by overlap. The averaged overlaps in panel (b) confirm that, as anticipated, a large fraction of states are exceedingly well approximated by a Slater determinant. Panel (a) then verifies that nonetheless, these states generically have noticeably incompatible orbitals, with the incompatibility roughly constant along the antidiagonal. The incompatibility is less pronounced for the states with the very largest overlaps, which as seen in panel (c) arise from the edge of the energy spectrum. Panels (d) and (e) show that these features are otherwise roughly independent of energy, provided again that we avoid the edges of the energy spectrum, according to which the states are ordered there [see panel

[11] Brueckner orbitals can be constructed systematically in several ways. Here, we adopt the method of Ref. [71], where one starts from a set of trial orbitals and updates these iteratively one at a time, by which $\mathcal{I}_m$ increases monotonously. This method can also be extended to approximate the state using $M > N$ orbitals entering several Slater determinants.

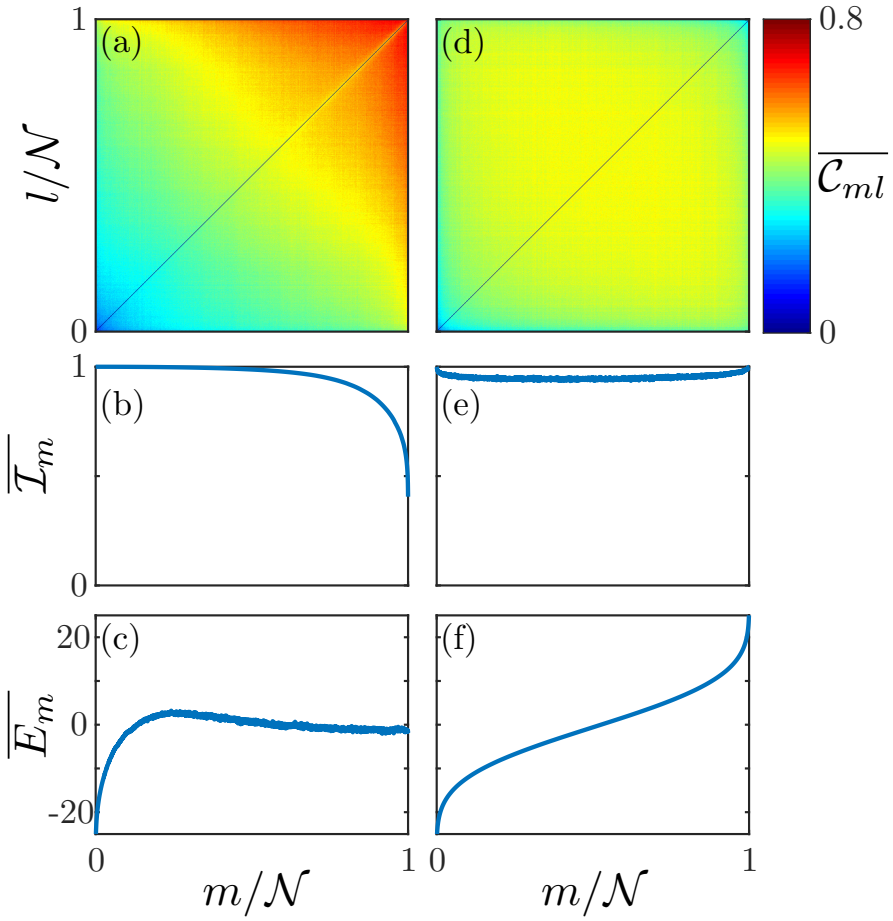

Figure 2.2: Geometric features of eigenstates in the many-body localised system (2.44) (half-filled system of size $L = 14$, with $V = 1.5$, $W = 8$; total number of states denoted as $\mathcal{N}$). In the left column, states are ordered by descending overlap $\mathcal{I}_m$ with a single Slater determinant, while in the right column they are ordered by ascending energy E_m; see panels (b,c,f,g) for the averaged behaviour of these quantities. The observed large overlaps $\mathcal{I}_m$ show that a large fraction of states are well approximated by a single Slater determinant. Panels (a,d) show the averaged incompatibility $\mathcal{C}_{ml}$ defined in Eq. (2.7), which quantifies the geometric interrelation of the states. This incompatibility is appreciable even for states with $\mathcal{I}_m \approx 1$, which are very precisely approximated by a single Slater determinant.

(f)].

As shown in Fig. 2.3, the observed incompatibility is indeed sizable and scales systematically with the system size. As a benchmark, we consider the extreme case of a pair of states with randomly incompatible orbitals, and hence mutually uncorrelated projectors. Applying random-matrix theory (RMT; see section 2.4.4), we find that for such a pair of states, the squared incompatibility averages to $\overline{\mathcal{C}_{ml}^2}|_{\mathrm{RMT}} = 2N^2(L-N)^2/(L-1)L(L+\eta)$,

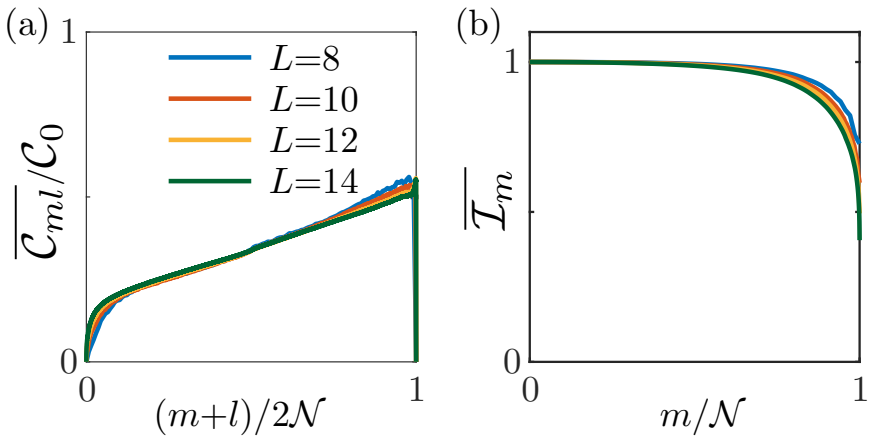

Figure 2.3: Panel (a) shows the orbital incompatibility $\mathcal{C}_{ml}$ for half-filled systems as in Fig. 2.2, but for different sizes $L = 8, 10, 12, 14$ and additionally averaged over pairs with fixed $l + m$ (states are ordered by descending overlap $\mathcal{I}_m$). The collapse of data in units of the random-matrix benchmark $\mathcal{C}_0 = \sqrt{L/8}$ reveals that this incompatibility scales systematically as in a random system, and takes appreciable values. Panel (b) shows that the overlap $\mathcal{I}_m$ itself only weakly depends on the system size.

where $\eta = 1$ for complex orbitals and $\eta = 2$ for real orbitals. Hence, as self-averaging suppresses statistical fluctuations, for a half-filled large system $\overline{\mathcal{C}_{ml}}|_{\mathrm{RMT}} \sim \sqrt{L/8} \equiv \mathcal{C}_0$. To compare the MBL system with this benchmark, we take the result from Fig. 2.2(a) averaged over the antidiagonals, and supplement this with the corresponding results for half-filled systems of size $L = 8, 10, 12$. Figure 2.3(a) then confirms that the incompatibility in the MBL system is indeed sizeable, and in particular scales reliably as $\overline{\mathcal{C}_{ml}} = O(L^{1/2})$, with a slight tendency to flatten out for larger systems.

Figure 2.4 illuminates how these characteristic features develop as a function of the disorder strength, where we focus on states from the central 10% of the energy spectrum. At values of $W \gtrsim 4$, where many-body localisation sets in, a noticeable fraction of these states become very well approximated by a single Slater determinant. This occurs roughly independently of the system size, as can be seen both from the averages shown in panel (b) as well as, in particular, in the colour-coded probability-density functions (pdfs) $P(\mathcal{I}_m)$ in panels (c,d). For smaller values of W, hence, in the ergodic phase, such well-approximated states are rare, and the pdf is strongly size dependent. On the other hand, the incompatibility measure $\mathcal{C}_{ml}$ retains its systematic scaling for all disorder strengths, approaching its RMT limiting value $\mathcal{C}_0$ for very weak disorder. Most importantly, this measure is again

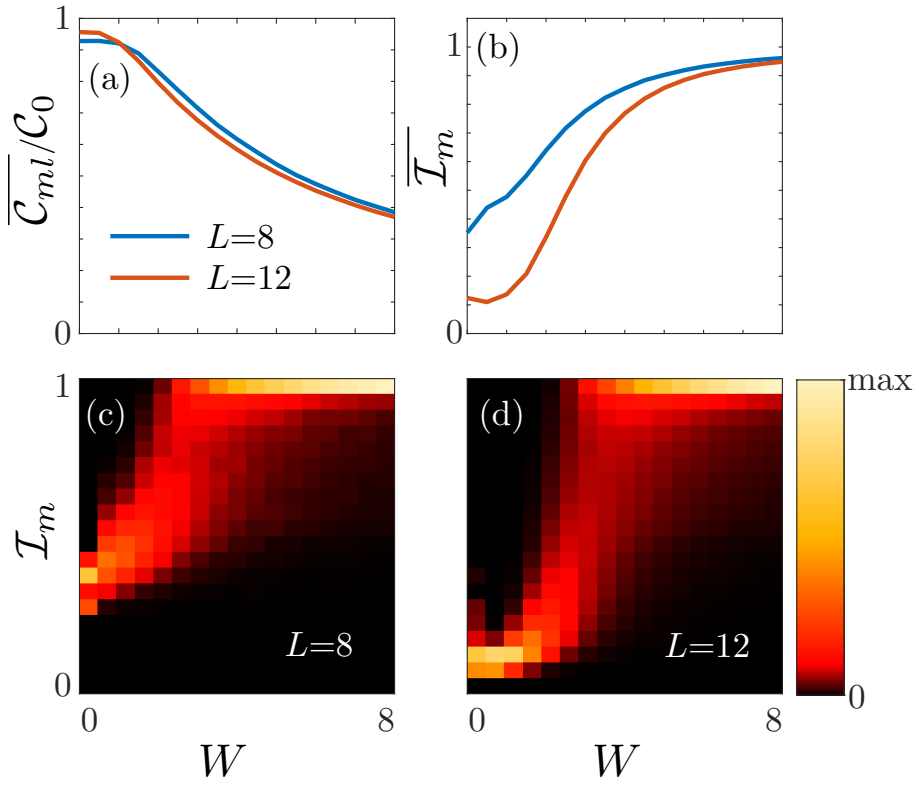

Figure 2.4: Dependence of (a) the averaged incompatibility $\mathcal{C}_{ml}$ and (b) the overlap $\mathcal{I}_m$ on the disorder strength W (half-filled systems of size $L = 8, 12$ at fixed $V = 1.5$, obtained from eigenstates from the middle 10% of the energy spectrum). Panels (c,d) display the colour-coded probability density function of $\mathcal{I}_m$ for both system sizes.

still sizeable deep in the MBL phase, dropping only gradually to $\approx \mathcal{C}_0/2$ at $W = 8$.

Figure 2.5 further explores how the incompatibility develops as interactions V are switched on when one moves from Anderson localisation to many-body localisation ($W = 8$, thick curve), and contrasts this with systems developing ergodic many-body dynamics ($W = 2, 3, 4$, thin curves). In the ergodic systems, the overlaps $\mathcal{I}_m$ drop significantly with increasing interactions, and depend noticeably on system size. In contrast, in the crossover to the MBL regime for $W = 8$, the overlaps $\mathcal{I}_m$ remain high while the incompatibility $\mathcal{C}_{ml}$ increases, with both quantities being only weakly dependent on the system size.

2.7.2 Numerical Evidence for Quasiparticle Dressing

So far, we have used the Brueckner orbitals to provide a direct geometric view of the relation between different many-body localised eigenstates. In the remainder, we highlight the utility of this framework to further illuminate the general phenomenology of these

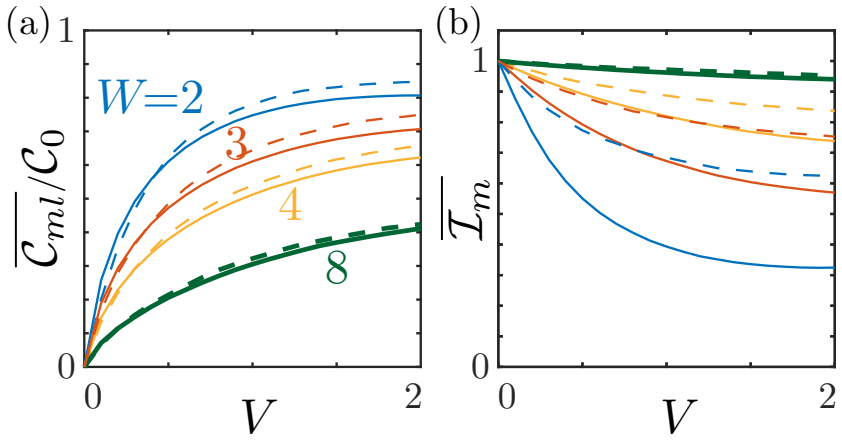

Figure 2.5: Dependence of (a) the averaged incompatibility $\mathcal{C}_{ml}$ and (b) the overlap $\mathcal{I}_m$ on the interaction strength V (half-filled systems of size $L = 12$, solid lines, and $L = 8$, dashed lines, obtained from eigenstates from the middle 10% of the energy spectrum). The thick lines show data for $W = 8$, where the system crosses over from Anderson localisation to many-body localisation. The thin lines contrast this to cases where the system transitions towards ergodic behaviour.

systems, and formulate new questions. This applies particularly to the notion of emergent integrability involving an extensive set of local conserved quantities, the aforementioned l-bits. In the present work, these l-bits provide useful context when one interprets them as quasiparticle densities $\mathcal{Q}_i = q_i^\dagger q_i$, and seeks to construct the quasiparticle operators in the form displayed in Eq. (2.1) [26].

In the noninteracting case, where $q_i^\dagger = p_i^\dagger$, all eigenstates are Slater determinants constructed from a shared set of single-particle orbitals. In a many-body localised system, higher-order terms must be taken into account, and a key guiding question is then whether this expansion is perturbative in nature. Focusing on the first term in the series and assuming that it dominates, this would require the eigenstates of the system to be well approximated by Slater determinants. But as we have seen, this is not a sufficient condition: even though the eigenstates are all well approximated by Slater determinants, these Slater determinants cannot be constructed from a common set of single-particle orbitals, revealing that the construction of the l-bits is of a nonperturbative nature.

To further quantify this, we consider the relation of eigenstates $|\psi_m\rangle$ with $N = L/2$ particles to eigenstates $|\psi_l\rangle$ with $N = L/2 - 1$ particles. Some of these eigenstates should be related by the application of a single quasiparticle operator $|\psi_m\rangle = q_i^\dagger|\psi_l\rangle$. In terms

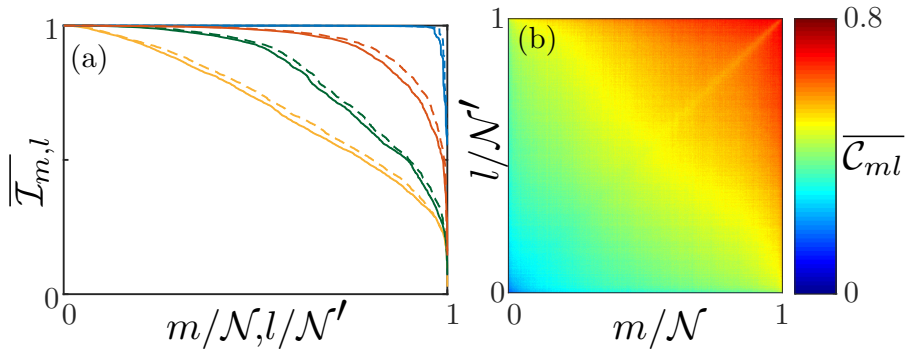

Figure 2.6: (a) Overlap $\mathcal{I}_{m,l}$ in individual realisations and (b) averaged orbital incompatibility in the system of Fig. 2.2, but with states taken from half-filling (solid curves, $N = 7$, index m) and from the sector with a particle removed (dashed curves, $N = 6$, index l; total number of states denoted as $\mathcal{N}'$). See the text for an interpretation of the systematic correlations in (a) and reduced incompatibility along the diagonal of (b) in terms of emergent integrability.

of the projectors, P_m and P_l, the compatibility of these states will then depend on how much the higher-order dressing terms in $q_i^\dagger$ fall into the space of orbitals that are already occupied in $|\psi_l\rangle$. If they fully do, the two states will have the same overlap with a single Slater determinant $\mathcal{I}_m = \mathcal{I}_l$, and be highly compatible.

As shown in Fig. 2.6, this feature is indeed present in the numerical data, and manifests itself both on the level of individual realisations as well as in the statistical averages. Firstly, as shown in panel (a), in individual realisations, hence, for fixed given systems, the overlaps $\mathcal{I}_m$ of states with different particle number follow each other closely. Secondly, as shown in panel (b), for pairs of states between which the generic compatibility is not already high, this interrelation shows up as a reduced averaged incompatibility of states along the diagonal. The threshold value $\overline{\mathcal{C}_{ml}} \approx 0.5$ at the boundary of the region where this effect is visible reveals the residual incompatibility of the described pairs of states.

These geometric observations give quantitative insights into emergent integrability down to the level of individual systems, circumventing the challenging task of directly constructing the underlying quasi-particle operators.

2.8 Conclusions

In summary, we established a geometric framework to describe the interrelation of eigenstates in fermionic many-body localised systems, unraveling the intriguing structure and correlations exhibited by these paradigms of constrained complex quantum dynamics. Applied to a paradigmatic model system, this approach reveals that while individual eigenstates are well approximated by single Slater determinants, they collectively depart from a uniquely-defined single-particle picture. This supports the notion of strongly dressed quasiparticle excitations residing behind the local conserved quantities that characterise the emergent integrability of these systems. The results complement the existing phenomenology based on individual eigenstates, such as the emergence of an area law of entanglement, both on the level of individual realisations as well as in statistical averages.

These considerations can also be usefully extended in a number of directions. For instance, based on our approach, one could inquire how well a single basis of orbitals can approximate a larger number of eigenstates, if not all of them. For this, the geometric perspective could be deepened by exploiting the general mathematical properties of the projectors P_m, hence, the structure of the Grassmannian $G(H_1, N)$ defined by the N dimensional subspaces in the single-particle Hilbert space H_1. Furthermore, to obtain additional insights into the ergodic phase and transition region, one could make use of the fact that the notion of Brueckner orbital could be extended to systematically approximate states by multiple Slater determinants. Finally, the described connection of our approach to the ubiquitous notion of l-bits, as well as generalisations of the one-particle density matrix [31,33], could be explored to extend these considerations to non-fermionic systems, such as bosonic systems and spin chains.

Chapter 3

Chiral Symmetry and Zero Modes

3.1 Context and Background

Complex quantum systems owe their rich physical properties to the intricate interplay of symmetries, disorder, and interactions. This interplay is mirrored by the intertwined concepts and frameworks which have been developed to capture these aspects. Symmetry-reduced representations of quantum systems were established at the beginning of quantum mechanics [85], while the absence of unitary symmetries allows for complex wave dynamics even for low numbers of degrees of freedom [86]. This ties both to semiclassical descriptions of classically chaotic systems as well as to statistical descriptions of structureless noninteracting disordered systems, whose properties are captured by random-matrix theory [87]. The latter provides a natural framework to classify complex quantum systems also in accordance with their invariance under antiunitary symmetries, as pioneered by Wigner and Dyson [88,89] and completed with the ten Altland-Zirnbauer universality classes [90]. This ten-fold way also underpins the topological classification of electronic band structures in periodic systems of different spatial dimensionality [91]. Besides time-reversal symmetry, this classification also accounts for antiunitary charge-conjugation symmetries and the combination of the two into a unitary chiral symmetry, as originally encountered in random-matrix descriptions of Dirac systems [92].

For structureless systems, random-matrix theory describes wave functions ergodically spreading across the whole system, but this can be amended to also provide statistical descriptions of Anderson-localised systems, in particular in one-dimensional or quasi-one-dimensional geometries [74]. Again, these descriptions can be organised according to

the universality classes of the ten-fold way [93], and then account for topological phenomena in nonperiodic, disordered settings. The most striking effect amongst these is the possibility of such systems to be less localised near spectral symmetry points. This phenomenon was first realised by Dyson [94], who noted that a one-dimensional system with hopping disorder develops a logarithmically diverging density of states around the band centre—the so-called Dyson singularity, which goes along with anomalously localised states that exhibit a stretched-exponential spatial profile. Within the classification framework described above, this relative delocalisation phenomenon becomes tied to the existence of a topologically protected zero mode in a chirally symmetric system with an odd-dimensional Hilbert space [95], and also occurs in higher-dimensional systems, where the anomalously localised states can resemble those at a metal-insulator transition [96,97]. Weaker analogues of such anomalous localisation characteristics also occur in absence of spectral symmetries [98, 99]. Such robust features deserve attention as they significantly broaden the scope for topologically protected quantum phenomena to realistic, disordered systems, both conceptually as well as in practical terms.

For many-body systems, interactions provide a significant complication of all of these aspects, with much recent effort devoted to the question of ergodic versus many-body localised behavior [2, 3, 100]. The ergodic phase is again well captured by random-matrix theory [101], reflecting its original setting of nuclear physics [102]. Topological aspects have been extensively studied for gapped ground-state physics [103], but topological order can also emerge in excited states, where it competes with the many-body localised phase [104, 105]. In particular, it has been found that such novel phases can be induced by a particle-hole symmetry that pairs up excited states around the centre of the spectrum [105–107]. However, the role of many-body zero modes pinned to such spectral symmetry points is much less understood, both conceptually as well as concerning the identification of concrete phenomena.

Here, we clarify this role by drawing motivation from the Dyson singularity. We first identify a natural disordered many-body system displaying an analogous chiral many-body zero mode, consisting of a simple spin-1 Ising chain with a random transverse field. We then address the question of its localisation properties both in real space and in Fock space, where we identify two localisation phenomena that characterise the zero mode. (i) In real space the spin correlations of the zero mode fragment into 5 independent sectors.

This fragmentation occurs both with respect to the even and odd sublattice, which generalises the sublattice polarisation of chiral zero modes in noninteracting systems, as well as with respect to the orientations of the correlated spin, which is specific to the chosen many-body context. This phenomenon holds at all disorder strengths. (ii) In contrast to the noninteracting case, the zero mode still localises at strong disorder, both in real space as well as in Fock space, as indicated, e.g., by an area law for the entanglement entropy, a large inverse participation ratio, and short-ranged spatial correlations. However, these measures also indicate that quantitatively, the zero mode is noticeably less localised than the nonzero modes—a phenomenon that for brevity we refer to as 'relative delocalisation' in the remainder of this work. In particular, the bipartite entanglement entropy is significantly enhanced for the zero mode by a system-size-independent factor of order unity, while the inverse participation ratio is correspondingly reduced. Thereby, the zero mode attains characteristics that set it apart from all other states in the system, even if they may be very close in energy.

In Sec. 3.2, we describe the spin-1 Ising chain, which provides a natural model for the described phenomena as it combines a chiral symmetry with an odd-dimensional Hilbert space, and always features a zero mode in one of the two spin-parity sectors. In Sec. 3.3 we first discuss the real-space fragmentation of the spin correlations, as this follows directly from the symmetry constraints and holds at all disorder strengths, which we show analytically and illustrate numerically. In this section we also identify the spin correlations that are most characteristic to quantify the localisation properties of zero modes and nonzero modes, to which we then turn to in Secs. 3.4 and 3.5. In Sec. 3.4 we demonstrate the relative delocalisation of the zero mode numerically based on both Fock-space and real-space measures. The analytical explanation of this relative delocalisation is provided in Sec. 3.5, where we identify the dominant hybridisation patterns of zero modes and nonzero modes. Enforced by the chiral-symmetry constraints, the dominant zero-mode hybridisation configurations involve three spin states on neighbouring spins, while those of nonzero modes only involve two spin states, so that the Fock-space localisation characteristics of these modes fundamentally differ. In Sec. 3.6 we summarise and discuss the results and put them into further context.

3.2 Background

3.2.1 Model

To demonstrate the effects outlined in this work, we require a many-body system in which a chiral symmetry is manifest for a system with an odd-dimensional Hilbert space. This is naturally provided by a spin-1 Ising chain with a transverse magnetic field, given by the Hamiltonian

$$H = \sum_{n=1}^{N} h_n S_n^z + J \sum_{n=1}^{N} S_n^x S_{n+1}^x. \tag{3.1}$$

Here J is the coupling strength between adjacent spins, described by the matrices

$$S^x = \frac{1}{\sqrt{2}} \begin{pmatrix} 0\,1\,0 \\ 1\,0\,1 \\ 0\,1\,0 \end{pmatrix}, \qquad S^y = \frac{1}{\sqrt{2}i} \begin{pmatrix} 0 & 1 & 0 \\ -1 & 0 & 1 \\ 0 & -1 & 0 \end{pmatrix}, \quad S^z = \begin{pmatrix} 1\,0 & 0 \\ 0\,0 & 0 \\ 0\,0 & -1 \end{pmatrix}, \tag{3.2}$$

while disorder of strength W is introduced via the on-site potentials, chosen independently from uniform box distributions $h_n \in [-W, W]$. While the 2-dimensional Pauli matrices are very well-known due to their exceedingly frequent use in the description of spin-1/2 systems, spin operators for higher spins are less commonly expressed. For this reason, it makes sense to define the function of spin operator for any arbitrary spin before proceeding with any specific matrix representations.

First of all, we should define the spin vector, which is commonly represented as:

$$\mathbf{S} = \begin{pmatrix} S^x \\ S^y \\ S^z \end{pmatrix}. \tag{3.3}$$

Each of the $\{S^i\}$ in Eq. (3.3) have commutation relations which hold regardless of spin, which are as follows:

$$\left[S^a, S^b\right] = i\varepsilon_{abc} S^c, \tag{3.4}$$

where $a, b, c \in \{x, y, z\}$, and ε_{abc} is the *Levi-Civita symbol*. In addition to the $\{S^i\}$ in Eq. (3.4), we can also define ladder operators of the form:

$$\begin{aligned} S^+ &= S^x + iS^y, \\ S^- &= S^x - iS^y. \end{aligned} \tag{3.5}$$

We can now define general properties for each of these operators. For a given spin-s,

the generalised form of its spin operators $\{S^i\}$, in the Zeeman basis $|s,m\rangle \equiv |m\rangle$, are:

$$\begin{aligned}
\langle m'|S^x|m\rangle &= (\delta_{m',m+1} + \delta_{m'+1,m})\frac{1}{2}\sqrt{s(s+1)-m'm}, \\
\langle m'|S^y|m\rangle &= (\delta_{m',m+1} - \delta_{m'+1,m})\frac{1}{2i}\sqrt{s(s+1)-m'm}, \\
\langle m'|S^z|m\rangle &= \delta_{m',m}m, \\
\langle m'|S^+|m\rangle &= \delta_{m',m+1}\sqrt{s(s+1)-m'm}, \\
\langle m'|S^-|m\rangle &= \delta_{m'+1,m}\sqrt{s(s+1)-m'm}, \\
\langle m'|\hat{\mathbf{S}}^2|m\rangle &= \delta_{m',m}s(s+1).
\end{aligned} \tag{3.6}$$

Considering the spin-1 case specifically, the action of the spin operators, defined in Eq. (3.6), on a given single-spin basis state are as follows:

$$\begin{aligned}
S^x|0\rangle &= \frac{1}{\sqrt{2}}(|+1\rangle + |-1\rangle), & S^x|\pm1\rangle &= \frac{1}{\sqrt{2}}|0\rangle, \\
S^y|0\rangle &= \frac{1}{\sqrt{2}i}(|+1\rangle - |-1\rangle), & S^y|\pm1\rangle &= \mp\frac{1}{\sqrt{2}}|0\rangle, \\
S^z|0\rangle &= 0|0\rangle, & S^z|\pm1\rangle &= \pm|\pm1\rangle.
\end{aligned} \tag{3.7}$$

From this point, if we define a single-spin basis in vector form like so:

$$|+1\rangle = \begin{pmatrix}1\\0\\0\end{pmatrix}, \quad |0\rangle = \begin{pmatrix}0\\1\\0\end{pmatrix}, \quad |-1\rangle = \begin{pmatrix}0\\0\\1\end{pmatrix}, \tag{3.8}$$

then we can proceed to build matrix representations of each of the primary spin operators of the form presented in Eq. (3.2). Along with ladder operators of the form:

$$S^+ = \sqrt{2}\begin{pmatrix}0&1&0\\0&0&1\\0&0&0\end{pmatrix}, \qquad S^- = \sqrt{2}\begin{pmatrix}0&0&0\\1&0&0\\0&1&0\end{pmatrix}. \tag{3.9}$$

The length of the chain is denoted as N, and in our general discussion below the size of the individual spins is denoted as S. The Hilbert space then has dimension $\mathcal{N} = (2S+1)^N$, and is conveniently spanned by the joint eigenbasis

$$|\mathbf{s}\rangle = \bigotimes_n |s_n^z\rangle \tag{3.10}$$

of all operators S_n^z, where we label the states by the vector $\mathbf{s}$ of components $s_n^z \in \{-S, -S+1, \ldots, S\}$.

3.2.2 Symmetries

The primary reason we choose to study the transverse Ising model owes to the fact that it possesses a chiral symmetry

$$\mathcal{X} H \mathcal{X} = -H, \tag{3.11}$$

with a unitary involution fulfilling $\mathcal{X}\mathcal{X}^\dagger = \mathcal{X}^2 = \mathbb{1}$. To see that this chiral symmetry is manifest for all sizes of spin, consider the spin rotation operator

$$\mathcal{X} = i^{2SN} \prod_{n \text{ even}} U_n^x(\pi) \prod_{n \text{ odd}} U_n^y(\pi), \tag{3.12}$$

or, more generally

$$U_{ab}(\pi) = i^{2SN} \prod_{n \text{ even}} U_n^a(\pi) \prod_{n \text{ odd}} U_n^b(\pi), \tag{3.13}$$

with individual rotation matrices

$$U_n^a(\varphi) = \exp\left(i\varphi S_n^a\right). \tag{3.14}$$

It is easy enough to see that $U_{ab}(\pi)$—via unitary transformation $U_{ab}(\pi) H U_{ab}^{-1}(\pi)$—reverses the sign of all Hamiltonians of the general form

$$H^{ab} = \sum_{i=1}^{N} h_i^c S_i^c + \sum_{i=1}^{N} J_i^a S_i^a S_{i+1}^a + \sum_{i=1}^{N} J_i^b S_i^b S_{i+1}^b, \tag{3.15}$$

provided that $a \neq b \neq c$, where $a, b, c \in \{x, y, z\}$.

The operator (3.12) is well-defined in infinite chains and finite chains with open boundary conditions, while periodic boundary conditions require that the chain consists of an even number of spins. This is easiest to highlight via examples.

The mathematical difference between open and periodic boundary conditions is the spin-spin interaction term between the first and N-th spin in the chain, in other words:

$$\begin{aligned} H_{\text{op}}^{ab} &= \sum_{n=1}^{N} h_n S_n^c + \sum_{n=1}^{N-1} J_n^a S_n^a S_{n+1}^a + \sum_{n=1}^{N-1} J_n^b S_n^b S_{n+1}^b, \\ H_{\text{per}}^{ab} &= H_{\text{op}}^{ab} + J_N^a S_N^a S_1^a + J_N^b S_N^b S_1^b. \end{aligned} \tag{3.16}$$

From Eq. (3.16), one can see that the $S_N^a S_1^a$ term only exists in the case of periodic boundary conditions. If we now turn our attention to the structure of Eq. (3.12), we can see that both of the possible chiral symmetry operators, U_{ab} and U^{ba}, both apply distinct operations to the even and odd sites of the spin chain. If we perform a chiral symmetry

transformation on our Hamiltonian with each boundary condition, we find that:

$$\begin{aligned} U_{ab}H^{ab}_{\text{op}}U_{ab} &= -H^{ab}_{\text{op}} \quad \forall\ N \\ U_{ab}H^{ab}_{\text{per}}U_{ab} &= \begin{cases} -H^{ab}_{\text{op}} + J^a_N S^a_N S^a_1 + J^b_N S^b_N S^b_1 & \text{if } N \text{ is odd} \\ -H^{ab}_{\text{op}} - J^a_N S^a_N S^a_1 - J^b_N S^b_N S^b_1 & \text{if } N \text{ is even} \end{cases} \end{aligned} \tag{3.17}$$

From Eq. (3.17), we can see that open boundary conditions preserve the chiral symmetry of the Hamiltonian for any number of spins; however, periodic boundary conditions only preserve the chiral symmetry if, and only if, the number of spins is even. Since we use periodic boundary conditions in our model, this restricts us to the study of even-length spin chains if we wish to study the effects of this chiral symmetry. This is what we will henceforth assume.

The operator $\mathcal{X}$ rotates all spins by π, about axes alternatingly aligned with x and y, thus inverting the sign of all on-site terms $\sim S^z_n$, as well as exactly one of the two spin operators in the interaction terms $\sim S^x_n S^x_{n+1}$, in accordance with the requirements of Eq. (3.11). The factor i^{2SN} in the definition (3.12) makes sure that $\mathcal{X}^2 = \mathbb{1}$ holds for all system lengths and arbitrary spin.

The assignment of sites as even or odd provides a gauge freedom, allowing the definition of an alternative chiral symmetry operator

$$\tilde{\mathcal{X}} = i^{2SN} \prod_{n \text{ even}} U^y_n(\pi) \prod_{n \text{ odd}} U^x_n(\pi). \tag{3.18}$$

It follows that the system also possesses an ordinary symmetry $[\mathcal{P}, H] = 0$, arising from

$$\mathcal{X}\tilde{\mathcal{X}} \propto \mathcal{P} \equiv \prod_n U^z_n(\pi), \tag{3.19}$$

which inverts the sign of all operators S^x_n in the Hamiltonian and leaves the operators S^z_n invariant. In the basis (3.10),

$$\mathcal{P}|\mathbf{s}\rangle = \exp\left(i\pi \sum_n s^z_n\right)|\mathbf{s}\rangle = (-1)^{\sum_n s^z_n}|\mathbf{s}\rangle, \tag{3.20}$$

so that $\mathcal{P}$ represents the total spin parity of the system. Therefore, we can divide the Hilbert space into sectors of even and odd parity, which are of size $\mathcal{N}_+ = \mathcal{N}_- = \mathcal{N}/2$ for half-integer spins, while

$$\mathcal{N}_\pm = (\mathcal{N} \pm (-1)^N)/2 \tag{3.21}$$

for integer spins. A partition into separate symmetry sectors would take the form:

$$H = H^+ \oplus H^- \cong \begin{pmatrix} \boxed{H^+} & 0 \\ 0 & \boxed{H^-} \end{pmatrix}, \tag{3.22}$$

where the basis of $H^{\pm}$ includes all basis states that fulfil $\langle X|\mathcal{P}|X\rangle = \pm 1$ for any given basis state $|X\rangle$. All numerical data in this report looks at the data collected from one of these symmetry sectors—never the total Hamiltonian—as we see extreme degeneracy-related effects in the eigenvalues if we do not discriminate between symmetry sectors.

Finally, as S_n^x and S_n^z can always be represented by real matrices, the Hamiltonian displays a time-reversal symmetry $\mathcal{T}H\mathcal{T} \equiv H^* = H$, where $\mathcal{T}$ is antiunitary and fulfils $\mathcal{T}^2 = 1$. Therefore, the system also possesses a charge-conjugation (particle-hole) symmetry $\mathcal{C}H\mathcal{C} = -H$, where $\mathcal{C} = \mathcal{T}\mathcal{X}$ is an antiunitary operator with $\mathcal{C}^2 = 1$.

For spins of size 1/2, it is well known that the rotations defined in Eq. (3.14) can be written as $U^a(\pi) = i\sigma_a$ with the usual 2×2-dimensional Pauli matrices σ_a, where one exploits the fact that $\sigma_a^2 = \mathbb{1}$. Note that U^a denotes a single-site operation, but the subscript is dropped simply for brevity. In the case of spin 1, where the spin operators are given by Eq. (3.2), we obtain in contrast

$$U^a(\pi) = \mathbb{1} - 2(S^a)^2, \tag{3.23}$$

where

$$U^a(\pi)U^b(\pi) = U^c(\pi) \quad \forall\ a \neq b \neq c \neq a, \tag{3.24}$$

with corresponding matrix representations

$$U^x = \begin{pmatrix} 0 & 0 & -1 \\ 0 & -1 & 0 \\ -1 & 0 & 0 \end{pmatrix}, \qquad U^y = \begin{pmatrix} 0 & 0 & 1 \\ 0 & -1 & 0 \\ 1 & 0 & 0 \end{pmatrix}, \quad U^z = \begin{pmatrix} -1 & 0 & 0 \\ 0 & 1 & 0 \\ 0 & 0 & -1 \end{pmatrix}. \tag{3.25}$$

It is easy enough to see from Eq. (3.25) that each of these operators is indeed Hermitian and squares to unity, which immediately implies unitarity.

In other words, the set of these chiral symmetry operators, with the identity operator, is isomorphic to the Klein four-group, which describes the symmetries of a nonsquare rectangle. We can also exploit the relations $[U^a, S^a] = 0$ and $\left\{U^a, S^b\right\} = 0$, provided that $a \neq b$. Also, while the spin-1 case is not as trivial as the spin-1/2 case, as many of the

convenient properties of the Pauli matrices do not hold here—i.e. distinct spin-1 operators do not anticommute, and also do not square to unity. Nonetheless, there is a particular property that spin-1 operators possess which is of use to us; namely:

$$\left\{S^a, (S^b)^2\right\} = S^a + \delta_{ab} S^a, \tag{3.26}$$

where $a, b \in \{x, y, z\}$.

3.2.3 Basis Transformations

Although much of the numerics are obtained from the specific Hamiltonian shown in Eq. (3.1), we can, in fact, generalise our findings by establishing operators that change the basis of our Hamiltonian. In order to generalise sufficiently, we require only two operators: the *roll* operator, and the *swap* operator.

The roll operator takes the form:

$$R^{xyz} = -(S^x S^y + S^y S^z + S^z S^x), \tag{3.27}$$

where the following properties hold true: $\det(R^{xyz}) = 1$, $R^{xyz}(R^{xyz})^\dagger = (R^{xyz})^\dagger R^{xyz} = \mathbb{1}$, and $(R^{xyz})^3 = \mathbb{1}$.

The roll operator applies a cyclic shift to each of the spin operators like so:

$$\begin{aligned} R^{xyz} S^x (R^{xyz})^\dagger &= S^y, \\ R^{xyz} S^y (R^{xyz})^\dagger &= S^z, \\ R^{xyz} S^z (R^{xyz})^\dagger &= S^x. \end{aligned} \tag{3.28}$$

The swap operator takes the form:

$$V^{ca} = \{S^a, S^c\} + i\varepsilon_{abc} S^a S^b S^c, \tag{3.29}$$

where the following properties hold true: $\det(V^{ca}) = 1$, $V^{ca} = (V^{ca})^\dagger$, and $(V^{ca})^2 = \mathbb{1}$.

The swap operator swaps two of the three spin operators, while reversing the sign of the third. In other words:

$$\begin{aligned} V^{ca} S^a V^{ca} &= S^c, \\ V^{ca} S^c V^{ca} &= S^a, \\ V^{ca} S^b V^{ca} &= -S^b. \end{aligned} \tag{3.30}$$

By using Eqs. (3.27) and (3.29), we can obtain any form of the transverse Ising model—depicted in Eq. (3.15)—by applying them in succession to our specific Hamiltonian (3.1).

3.2.4 Symmetry Groups

The operators we have defined thus far—$\{U^a\}$, $\{V^{ca}\}$, and R^{xyz}—are all members of the SU(3) symmetry group. In fact, we can define a symmetry group via these operators which is necessarily subject to all four of the group axioms (with multiplication as the group operation). The symmetry group is:

$$G = \mathcal{U}\mathcal{R}\mathcal{V}, \tag{3.31}$$

where $AB = \{ab : a \in A, b \in B\}\ \forall\ A, B$ is a pairwise composition of the elements in A and B, and the relevant proper subgroups are defined as:

$$\begin{aligned} \mathcal{U} &= \mathcal{U}^x \cup \mathcal{U}^y \cup \mathcal{U}^z, \\ \mathcal{R} &= \{\mathbb{1}, R^{xyz}, (R^{xyz})^\dagger\}, \\ \mathcal{V} &= \mathcal{V}^{xy} \cup \mathcal{V}^{yz} \cup \mathcal{V}^{zx} \end{aligned} \tag{3.32}$$

where $\mathcal{U}^a = \{\mathbb{1}, U^a\}$, $\mathcal{V}^{ca} = \{\mathbb{1}, U^b V^{ca}\}$, provided that $a \neq b \neq c$ and $a, b, c \in \{x, y, z\}$. For ease of reference, we can define $S_0(G) = \{\mathcal{U}^x, \mathcal{U}^y, \mathcal{U}^z, \mathcal{R}, \mathcal{V}^{xy}, \mathcal{V}^{yz}, \mathcal{V}^{zx}\}$ as the set of all simple proper subgroups of G.

In addition to the larger symmetry group G, we can also identify a set of useful non-simple proper subgroups $S(G)$, each element of which is also subject to all four of the group axioms:

$$S(G) = \{\mathcal{U}, \mathcal{U}\mathcal{R}, G \backslash \mathcal{U}, \mathcal{R} \cup \mathcal{V}\}, \tag{3.33}$$

where $A \backslash B = \{a : a \in A, a \notin B\}\ \forall\ A, B$ denotes the group of all elements which are in A, but are not in B. If we look closely, we can deduce that $\mathcal{R} \cup \mathcal{V}$ is isomorphic to the dihedral group of order six D_3, and thus describes the symmetries of an equilateral triangle. We can prove this isomorphism by considering the form of D_3 like so:

$$D_3 = \{r_0, r_1, r_2, s_{12}, s_{23}, s_{31}\}, \tag{3.34}$$

where $\{r_0, r_1, r_2\}$ and $\{s_{12}, s_{23}, s_{31}\}$ respectively denote the set of rotations and reflections that leave the equilateral triangle unchanged. We can also write down the complete set of simple subgroups of D_3, $S_0(D_3) = \{\{r_0, r_1, r_2\}, \{r_0, s_{12}\}, \{r_0, s_{23}\}, \{r_0, s_{31}\}\}$.

The elements D_3 can be expressed as linear maps:

$$\begin{aligned} r_1 &: (1,2,3) \mapsto (3,1,2), \\ s_{ab} &: (1,2,3) \mapsto \begin{cases} (2,1,3) & \text{if } (a,b) = (1,2) \\ (1,3,2) & \text{if } (a,b) = (2,3) \\ (3,2,1) & \text{if } (a,b) = (3,1) \end{cases} \end{aligned} \tag{3.35}$$

where $(1,2,3)$ denotes the corners of an equilateral triangle, which are numbered in ascending order in the clockwise direction. We can now prove that $(\mathcal{R} \cup \mathcal{V}) \cong D_3$.

Proof. This should prove that there exists a group isomorphism between $\mathcal{R} \cup \mathcal{V}$ and D_3.

(i): If $\mathcal{R} \cup \mathcal{V}$ is isomorphic to D_3, then there exists a linear map f, such that

$$f : (\mathcal{R} \cup \mathcal{V}) \mapsto D_3,$$

where f is defined as:

$$f(ab) = f(a)f(b) = f(i)f(j) = f(ij),$$

for all $a, b \in (\mathcal{R} \cup \mathcal{V})$, $i, j \in D_3$.

(ii): $\mathcal{R} \cup \mathcal{V}$ and D_3 possess the same group operation; therefore, we can trivially let $f(x) = x$, which instantly proves $f(xy) = f(x)f(y)\ \forall\ x, y$ and reduces the proof of $f(ab) = f(a)f(b) = f(i)f(j) = f(ij)$ to the proof of $ab = ij$.

(iii): Set $(\mathbb{1}, R^{xyz}, (R^{xyz})^\dagger, U^z V^{xy}, U^x V^{yz}, U^y V^{zx}) = (r_0, r_1, r_2, s_{12}, s_{23}, s_{31}) = (1,2,3,4,5,6) \equiv \boldsymbol{v}$. This allows us to write down:

$$\begin{aligned} \mathbb{1} &: \boldsymbol{v} \mapsto (1,2,3,4,5,6) \leftarrow\!\shortmid r_0 : \boldsymbol{v}, \\ R^{xyz} &: \boldsymbol{v} \mapsto (3,1,2,6,4,5) \leftarrow\!\shortmid r_1 : \boldsymbol{v}, \\ (R^{xyz})^\dagger &: \boldsymbol{v} \mapsto (2,3,1,5,6,4) \leftarrow\!\shortmid r_2 : \boldsymbol{v}, \\ U^z V^{xy} &: \boldsymbol{v} \mapsto (4,5,6,1,2,3) \leftarrow\!\shortmid s_{12} : \boldsymbol{v}, \\ U^x V^{yz} &: \boldsymbol{v} \mapsto (5,6,4,3,1,2) \leftarrow\!\shortmid s_{12} : \boldsymbol{v}, \\ U^y V^{zx} &: \boldsymbol{v} \mapsto (6,4,5,2,3,1) \leftarrow\!\shortmid s_{12} : \boldsymbol{v}. \end{aligned}$$

(iv): (ii) and (iii) prove that (i) is true; therefore

$$(\mathcal{R} \cup \mathcal{V}) \cong D_3.$$

3.2.5 Variance of Basis States

One might ask the question of how well the basis states approximate the many-body eigenstates. One possible measure of this is defined as such:

$$\Delta(E^X) \equiv \sqrt{\langle X|H^2|X\rangle - \langle X|H|X\rangle^2}. \tag{3.36}$$

From Eq. (3.36), we can see that $\Delta(E^X) = 0$ if $\langle X|H^2|X\rangle = \langle X|H|X\rangle^2$, and this is only true if $|X\rangle$ is an eigenstate of H. Therefore, we can use Eq. (3.36) as a measure of how well $|X\rangle$ approximates $|\psi_n\rangle$.

Some algebraic manipulation yields the following result:

$$\Delta(E^X) = J\sqrt{\sum_{i=1}^{N} \langle X|(S_i^x)^2(S_{i+1}^x)^2|X\rangle}, \tag{3.37}$$

which can be written alternatively as

$$\Delta(E^X) = \frac{1}{2}J\sqrt{4N(0,0) + 2N(0,1) + N(1,1)}, \tag{3.38}$$

where $N(|s_i|, |s_{i+1}|)$ counts the number of times the permutation (s_i, s_{i+1}) appears in the basis state $|X\rangle$, and is subject to the following constraint:

$$N(0,0) + N(0,1) + N(1,1) = \begin{cases} N-1 & \text{if } H = H_{\text{op}} \\ N & \text{if } H = H_{\text{per}} \end{cases} \tag{3.39}$$

From Eq. (3.38), we can see that the permutation $(0,0)$ contributes the most to $\Delta(E^X)$, thus the highest value of $\Delta(E^X)$ occurs when $|X\rangle = |\mathbf{0}\rangle$. This means that $|\mathbf{0}\rangle$ is the worst approximation of a given many-body eigenstate (compared to other basis states), and any many-body eigenstates that primarily localise through this channel will probably be more delocalised (in Fock-space) than the average state.

3.2.6 The Zero Mode

A direct consequence of the chiral symmetry is that eigenstates $|\psi_k\rangle$ with energies E_k are paired with eigenstates $|\psi_{\bar{k}}\rangle = \mathcal{X}|\psi_k\rangle$ with energy $E_{\bar{k}} = -E_k$. The exception are zero modes with energy $E_k = 0$, for which we formally identify the indices $\bar{k} = k$. Even in the case of degeneracy of these zero modes, they can always be chosen to fulfil $\mathcal{X}|\psi_k\rangle = \sigma|\psi_k\rangle$, where $\sigma = \pm 1$ distinguishes between two types of zero modes. The number ν_σ of modes of each type is then constrained by the signature of $\mathcal{X}$, according to $\operatorname{Tr}\mathcal{X} = \nu_+ - \nu_-$, which

serves as a topological index. In particular, in a system with an odd overall Hilbert space dimension, at least one zero mode is always guaranteed to exist, as it is impossible to pair up all states.

In the Ising chain, the Hilbert space dimension $\mathcal{N}$ is even in the case of half-integer spins, and so are the two parity sectors of dimensionality $\mathcal{N}_\pm = (2S+1)^{N-1}$ as soon as $N \geq 2$. In contrast, according to Eq. (3.21), for integer spins $\mathcal{N}_-$ is even but $\mathcal{N}_+$ is odd. Hence, at least one zero mode, denoted as $|\psi_0\rangle$, is guaranteed to exist in the even-parity sector of chains with integer spins. In the basis (3.10), this can be attributed to the existence of the state $|\mathbf{0}\rangle$ (the state where $s_n^z = 0$ for all spins), which is the only basis state that is left invariant under the operation with the chiral operator $\mathcal{X}$, which connects all other basis states in pairs with index $\mathbf{s}$ and $\bar{\mathbf{s}} = -\mathbf{s}$.

The zero mode possesses an energy that remains pinned to zero no matter the disorder or interaction strength. This invariance with respect to parameter variations does not occur for any other eigenstate, which leaves the question if this has any bearings on the localisation characteristics, in analogy to what is known from single-particle systems. Therefore, the key question explored in this work is whether the zero mode displays different localisation characteristics to the modes with finite energy.

3.2.7 Numerical Techniques

We will address the localisation properties of the zero mode both by analytical and numerical approaches. The numerical results are obtained by exact diagonalisation from the positive parity sector in chains with an even number N of spins of size $S = 1$, where we apply periodic boundary conditions. As the effective Hilbert space dimension rises as $(3^N + 1)/2$, and only a single zero mode is present in each realisation, we obtain disorder averages from chains of limited lengths up to $N = 8$, but also show results from individual realisations with $N = 10$. For nonzero modes we collect data from the middle 10% of the spectrum. Quantities assigned to the zero mode are denoted in the form Q_0, while those of nonzero modes are denoted in the form $Q_{\neq 0}$. Disorder averages of any quantity are denoted by an overline, and are obtained from 10000 realisations. Where focusing on individual disorder strengths, we use values $W = 1$ for weak disorder (ergodic regime), $W = 8$ for moderate disorder, and $W = 20$ for strong disorder (localised regime).

3.3 Fragmentation of the Zero-Mode Correlations

We start with a general key characteristic of the zero mode, which relates to its real-space structure and holds at all strengths of disorder. We first introduce the spin correlation matrix that captures this structure, and discuss its general properties. We then show that the spin correlations of the zero mode fragment into five independent elementary patterns, while for nonzero modes there are only two, and verify and illustrate these patterns numerically.

3.3.1 Spin Correlation Matrix

The real-space spin structure in a given energy eigenstate $|\psi_k\rangle$ is captured by the correlations

$$C_{k,nm} \equiv \begin{pmatrix} \langle S_n^x S_m^x \rangle & \langle S_n^x S_m^y \rangle & \langle S_n^x S_m^z \rangle \\ \langle S_n^y S_m^x \rangle & \langle S_n^y S_m^y \rangle & \langle S_n^y S_m^z \rangle \\ \langle S_n^z S_m^x \rangle & \langle S_n^z S_m^y \rangle & \langle S_n^z S_m^z \rangle \end{pmatrix}, \tag{3.40}$$

which we consider as blocks of a Hermitian matrix $\mathcal{C}_k$ of dimension $3N \times 3N$. We term the eigenvalues and eigenvectors of this correlation matrix the correlation eigenvalues and eigenvectors, in distinction to the energy eigenvalues and eigenvectors associated with the Hamiltonian.

The following features are useful to note.

(i) According to the relation $(S_n^x)^2 + (S_n^y)^2 + (S_n^z)^2 = 2\mathbb{1}$, the trace $\mathrm{Tr}\,\mathcal{C}_k = 2N$ is fixed.

(ii) The matrix is well-behaved under local changes $(S_n^x, S_n^y, S_n^z) \to (S_n^x, S_n^y, S_n^z)O_n^T$ of the spin basis by an orthogonal transformation O_n (hence, basis changes that are compatible with the Lie algebra), which transform the correlation matrix as $C_{k,nm} \to O_n C_{k,nm} O_m^T$. This leaves the eigenvalues of $\mathcal{C}_k$ invariant, while the corresponding eigenvectors automatically adapt to the chosen local spin orientations.

(iii) Since the eigenstates of the Hamiltonian have a fixed parity, the expectation values $\langle S_n^z S_m^x \rangle = \langle S_n^z S_m^y \rangle = 0$. Therefore, the spin correlation matrix decomposes into a direct sum $\mathcal{C}_k = \Delta_k \oplus Z_k$, given by the block decomposition $C_{k,nm} = \Delta_{k,nm} \oplus Z_{k,nm}$, where

$$\Delta_{k,nm} = \begin{pmatrix} \langle S_n^x S_m^x \rangle & \langle S_n^x S_m^y \rangle \\ \langle S_n^y S_m^x \rangle & \langle S_n^y S_m^y \rangle \end{pmatrix}, \tag{3.41}$$

$$Z_{k,nm} = \langle S_n^z S_m^z \rangle .$$

(iv) Utilising the unitary matrix

$$V = \frac{1}{\sqrt{2}} \begin{pmatrix} 1 & 1 \\ -i & i \end{pmatrix}, \tag{3.42}$$

we can further introduce the transformed matrix

$$\rho_{k,nm} = V^\dagger \Delta_{k,nm} V = \begin{pmatrix} \langle S_n^+ S_m^- \rangle & \langle S_n^+ S_m^+ \rangle \\ \langle S_n^- S_m^- \rangle & \langle S_n^- S_m^+ \rangle \end{pmatrix} \tag{3.43}$$

with spin-ladder operators $S_n^\pm = 2^{-1/2}(S_n^x \pm iS_n^y)$. Recalling the analogy between spin-ladder operators and fermionic creation and annihilation operators for systems with spin 1/2, this expression resembles a one-particle density matrix (OPDM), equipped with a Bogoliubov-Nambu structure that is appropriate for a system with a nonconserved particle number.

(v) In a canonical basis state $|\mathbf{s}\rangle$, the correlation matrix $\Delta_\mathbf{s}$ is block-diagonal, with each block having a correlation eigenvalue 1 and an eigenvalue $1-(s_n^z)^2$, so that the correlation eigenvectors are localised on individual spins. The correlation matrix $Z_\mathbf{s}$ then has elements $Z_{\mathbf{s},nm} = s_n^z s_m^z$, and hence is of rank 1, with a single finite eigenvalue $Z_\mathbf{s}^{\max} = \sum_n (s_n^z)^2$ (as indicated, we interpret this as the maximal eigenvalue). This counts the number of spins with a nonzero z component.

These features imply that fully localised states are characterised by an approximately quantised correlation spectrum, in close analogy to the OPDM occupation spectrum in a many-body localised system [25, 26, 33]. In contrast, in an ergodic state represented by a random superposition of basis states, the correlation matrix self-averages to $\mathcal{C}_k^{\text{erg}} \sim (2/3)\mathbb{1}$. This results in a correlation spectrum centred around the single value 2/3, smoothed out by the influence of the residual off-diagonal elements of $\mathcal{C}_k$, which is in close analogy to the smooth OPDM occupation spectrum in an ergodic many-body system. The properties of our defined spin correlation matrix (3.40)—stated within this section—can be made clear by considering special cases, to which we now turn.

3.3.2 Illustrative Special Cases

3.3.2.1 The Noninteracting ρ Matrix

Since our system undergoes Fock-space localisation in our chosen basis of spin operators, it makes sense to formulate the properties of the ρ-OPDM in the ideal case of perfect

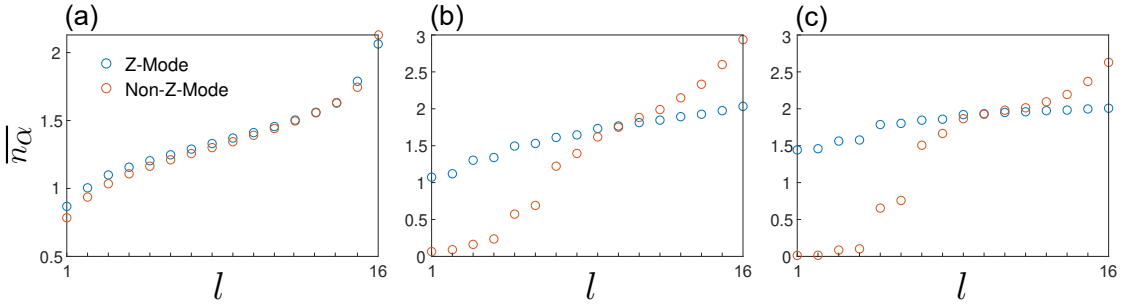

Figure 3.1: (a) Ergodic regime: The ρ-OPDM eigenvalues are close to continuous for both the zero-mode and non-zero-mode; this is typical for most ergodic systems. (b) Transition regime: The ρ-OPDM eigenvalues start to highlight differences between the zero-mode and non-zero-mode. A gap starts to open up in the non-zero-mode spectrum at while the zero-mode spectrum starts to level out and plateau. (c) Localised regime: The ρ-OPDM eigenvalues are now clearly distinct between the zero-mode and non-zero-mode. There appear to be two gaps in the non-zero-mode spectrum, while the zero-mode spectrum has almost completely levelled out at $\langle n_\alpha \rangle \sim 2$. This could possibly be a signature of the possible delocalisation of the zero-mode. Disorder-averaged over 10^3 disorder realisations.

Fock-space localisation. In order to do this, we begin by first defining some lightened notation for an arbitrary cross-term:

$$\rho^{(s',s)} \equiv \begin{pmatrix} \langle s'| S^+S^- |s\rangle & \langle s'| S^+S^+ |s\rangle \\ \langle s'| S^-S^- |s\rangle & \langle s'| S^-S^+ |s\rangle \end{pmatrix}. \tag{3.44}$$

The non-vanishing cross-terms are given by:

$$\begin{aligned} \rho^{(1,1)} &= \begin{pmatrix} 2 & 0 \\ 0 & 0 \end{pmatrix}, \qquad \rho^{(1,-1)} = \begin{pmatrix} 2 & 0 \\ 0 & 2 \end{pmatrix}, \quad \rho^{(-1,1)} = \begin{pmatrix} 2 & 0 \\ 0 & 0 \end{pmatrix}, \\ \rho^{(-1,-1)} &= \begin{pmatrix} 2 & 0 \\ 0 & 0 \end{pmatrix}, \qquad \rho^{(0,0)} = \begin{pmatrix} 2 & 0 \\ 0 & 2 \end{pmatrix}. \end{aligned} \tag{3.45}$$

In the case of perfect Fock-space localisation, any given many-body eigenstate will be equal to a given many-body basis state i.e. $|\psi\rangle = |X\rangle$. Using this fact, we can define more specific notation concerning the many-body diagonal terms:

$$\rho_{X,ij} \equiv \begin{pmatrix} \langle X| S_i^+S_j^- |X\rangle & \langle X| S_i^+S_j^+ |X\rangle \\ \langle X| S_i^-S_j^- |X\rangle & \langle X| S_i^-S_j^+ |X\rangle \end{pmatrix}. \tag{3.46}$$

It is not too hard to surmise that Eq. (3.46) can be succinctly summarised by the following

statements:

$$\begin{aligned} &\rho_{X,ii} \in \{\rho^{(0,0)}, \rho^{(1,1)}, \rho^{(-1,-1)}\}, \\ &\rho_{X,ij} = 0_2 \quad \forall\ i \neq j. \end{aligned} \tag{3.47}$$

This allows us to write our fully diagonalised ρ-OPDM as

$$D(\rho_X) = \bigoplus_{i=1}^{N} \rho_{X,ii}. \tag{3.48}$$

From Eq. (3.48), we can see that perfect Fock-space localisation ($|\psi\rangle = |X\rangle$) reduces ρ-OPDM to a diagonal matrix with exactly two distinct eigenvalues: two and zero. Each non-zero spin in $|X\rangle$ contributes $\{0, 2\}$ to the eigenvalue spectrum, while each zero spin contributes $\{2, 2\}$. These analytical results are in good agreement with what is seen in initial numerical work for a system of size $N = 8$, as seen in Fig. 3.1.

3.3.2.2 The Noninteracting $\mathcal{C}$ Matrix

We again consider the case of perfect Fock-space localisation, and thus formulate some lightened notation for a given cross-term:

$$C^{(s',s)} \equiv \Delta^{(s',s)} \oplus Z^{(s',s)}, \tag{3.49}$$

where

$$\begin{aligned} \Delta^{(s',s)} &\equiv \begin{pmatrix} \langle s'| S^x S^x |s\rangle & \langle s'| S^x S^y |s\rangle \\ \langle s'| S^y S^x |s\rangle & \langle s'| S^y S^y |s\rangle \end{pmatrix}, \\ Z^{(s',s)} &\equiv \left\langle s' \right| S^z S^z \left| s \right\rangle. \end{aligned} \tag{3.50}$$

We can now calculate the non-vanishing cross-terms explicitly:

$$\begin{aligned} &\Delta^{(\pm1,\pm1)} = \frac{1}{2}\begin{pmatrix} 1 & \pm i \\ \mp i & 1 \end{pmatrix}, \qquad \Delta^{(\pm1,\mp1)} = \frac{1}{2}\begin{pmatrix} 1 & \mp i \\ \pm i & -1 \end{pmatrix}, \quad \Delta^{(0,0)} = \begin{pmatrix} 1 & 0 \\ 0 & 1 \end{pmatrix}, \\ &Z^{(\pm1,\pm1)} = 1, \qquad\qquad Z^{(\pm1,\mp1)} = -1. \end{aligned} \tag{3.51}$$

Interestingly, each of these Spin-1 cross-terms can be written quite succinctly as linear combinations of the spin-1/2 operators (including the identity operator).

Again, we define notation for the many-body diagonal terms:

$$C_{X,ij} \equiv \Delta_{X,ij} \oplus Z_{X,ij}, \tag{3.52}$$

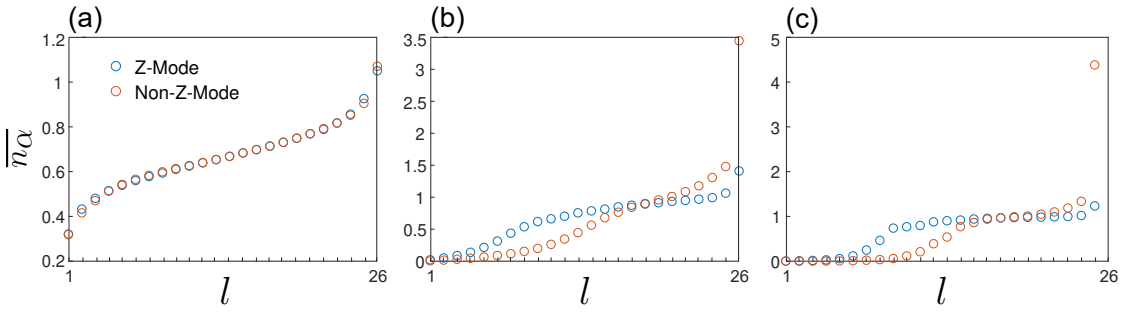

Figure 3.2: (a) Ergodic regime: The $\mathcal{C}$-OPDM eigenvalues are close to continuous for both the zero-mode and non-zero-mode; this is typical for most ergodic systems. (b) Transition regime: The $\mathcal{C}$-OPDM eigenvalues start to highlight differences between the zero-mode and non-zero-mode. A gap starts to open up in the non-zero-mode spectrum as its highest eigenvalue rises dramatically, while the zero-mode spectrum starts to level out and plateau. (c) Transition regime: The $\mathcal{C}$-OPDM eigenvalues are now clearly distinct between the zero-mode and non-zero-mode. A third of the zero-mode eigenvalues are close to zero and the remaining two-thirds plateau at $\langle n_\alpha \rangle \sim 1$. The non-zero-mode eigenvalues exhibit a similar trend; however, more than a third of the non-zero-mode eigenvalues are close to zero and there is a large gap between the highest eigenvalue and the others due to the constraint of the $\mathcal{C}$-OPDM's fixed trace. This stems from the dominant eigenvalue of Z_X being very high for the typical non-zero mode where $|\psi_n\rangle$ is close to $|X \neq \mathbf{0}\rangle$. Disorder-averaged over 10^3 disorder realisations.

where

$$\Delta_{X,ij} \equiv \begin{pmatrix} \langle X| S_i^x S_j^x |X\rangle & \langle X| S_i^x S_j^y |X\rangle \\ \langle X| S_i^y S_j^x |X\rangle & \langle X| S_i^y S_j^y |X\rangle \end{pmatrix}, \qquad (3.53)$$
$$Z_{X,ij} \equiv \langle X| S_i^z S_j^z |X\rangle .$$

Via some logical deductions, we can summarise Eq. (3.52) by the following statements:

$$\begin{aligned} C_{X,ii} &= \Delta_{X,ii} \oplus Z_{X,ii}, \\ C_{X,ij} &= 0_2 \oplus Z_{X,ij} \quad \forall\ i \neq j, \end{aligned} \qquad (3.54)$$

where

$$\begin{aligned} &\Delta_{X,ii} \oplus Z_{X,ii} \in \{C^{(0,0)}, C^{(1,1)}, C^{(-1,-1)}\}, \\ &Z_{X,ij} \in \{-1, 0, 1\} \quad \forall\ i, j. \end{aligned} \qquad (3.55)$$

We can rearrange the order of our $\mathcal{C}$-OPDM's basis states into a more convenient form—

$(\hat{e}_1^x, \hat{e}_1^y, \hat{e}_1^z, \hat{e}_2^x, \hat{e}_2^y, \hat{e}_2^z, \ldots, \hat{e}_N^x, \hat{e}_N^y, \hat{e}_N^z) \rightarrow (\hat{e}_1^x, \hat{e}_1^y, \hat{e}_2^x, \hat{e}_2^y, \ldots, \hat{e}_N^x, \hat{e}_N^y, \hat{e}_1^z, \hat{e}_2^z, \ldots, \hat{e}_N^z)$. Exploiting this reordering allows us to write our full $\mathcal{C}$-OPDM as

$$\mathcal{C}_X = \bigoplus_{i=1}^{N} (\Delta_{X,ii}) \oplus Z_X. \tag{3.56}$$

This vastly simplifies the eigenproblem to:

$$\begin{aligned} \det(\mathcal{C}_X - \lambda\mathbb{1}) &= \prod_{i=1}^{N} [\det(\Delta_{X,ii} - \lambda\mathbb{1})] \det(Z_X - \lambda\mathbb{1}), \\ \mathrm{eig}(\mathcal{C}_X) &= \bigcup_{i=1}^{N} [\mathrm{eig}(\Delta_{X,ii})] \cup \mathrm{eig}(Z_X). \end{aligned} \tag{3.57}$$

We can now diagonalise each $\Delta_{X,ii}$ very easily and thus obtain:

$$D(\Delta_{X,ii}) \in \left\{ \begin{pmatrix} 1 & 0 \\ 0 & 1 \end{pmatrix}, \begin{pmatrix} 0 & 0 \\ 0 & 1 \end{pmatrix} \right\}, \tag{3.58}$$

where each non-zero spin in $|X\rangle$ contributes $\{0, 1\}$ to the eigenvalue spectrum, and each zero spin contributes $\{1, 1\}$.

Now that we have the eigenvalues of the $\{\Delta_{X,ii}\}$, we need the eigenvalues of Z_X. We can begin this problem by first writing down the simple general structure of Z_X explicitly:

$$Z_X = \boldsymbol{s}_X \boldsymbol{s}_X^{\mathrm{T}} = \begin{pmatrix} s_1^X s_1^X & \ldots & s_1^X s_N^X \\ \vdots & \ddots & \vdots \\ s_N^X s_1^X & \ldots & s_N^X s_N^X \end{pmatrix}, \tag{3.59}$$

where s_i^X represents the spin of the i-th spin in basis state $|X\rangle$, and $\boldsymbol{s}_X = (s_1^X, s_2^X, \ldots, s_N^X)$. From the structure of Eq. (3.59)), we can deduce that every row is proportional to every other; therefore

$$\mathrm{rank}(Z_X) = \begin{cases} 0 & \text{if } |X\rangle = |\mathbf{0}\rangle \\ 1 & \text{otherwise} \end{cases} \tag{3.60}$$

By making use of the *rank-nullity theorem*, we can now diagonalise Z_X as:

$$D(Z_X) = 0_{N-1} \oplus \mathrm{Tr}(Z_X), \tag{3.61}$$

where

$$\mathrm{Tr}(Z_X) = \boldsymbol{s}_X^{\mathrm{T}} \boldsymbol{s}_X = \sum_{i=1}^{N} s_i^2. \tag{3.62}$$

The form of Eq. (3.62) immediately tells us that the dominant eigenvalue of Z_X is equal to the number of non-zero spins in $|X\rangle$.

We can now write our fully diagonalised $\mathcal{C}$-OPDM as:

$$D(\mathcal{C}_X) = \bigoplus_{i=1}^{N} [D(\Delta_{X,ii})] \oplus 0_{N-1} \oplus \mathrm{Tr}(Z_X). \tag{3.63}$$

This seems simple enough; however, we can actually recover our ρ-OPDM directly from our $\mathcal{C}$-OPDM by noting the form of Eqs. (3.47) and (3.58), which directly imply that $D(\rho_X) = 2D(\Delta_X)$. These analytical results are in good agreement with what is seen in initial numerical work for a system of size $N = 8$, as seen in both Figs. 3.1 and 3.2.

3.3.2.3 The General Z Matrix

The Z matrix is simpler in structure, and thus we do not need to make the assumption of perfect Fock-space localisation to make meaningful statements about it. Since the S^z spin operator is diagonal, we can surmise that, for any arbitrary many-body eigenstate, we can write the elements of our so-called Z-OPDM—defined in Eq. (3.41)—as

$$Z_{n,ij} = \sum_{X\in[-d,d]} |\psi_n(X)|^2 \langle X|S_i^z S_j^z|X\rangle \,. \tag{3.64}$$

By making use of the chiral symmetry present in our system—and the resulting "mirrored" eigenstates—it is convenient to write a given many-body eigenstate as

$$|\psi_n\rangle \equiv \sum_{X\in[-d,d]} \psi_n(X)\,|X\rangle \,, \tag{3.65}$$

where the indices d label the basis states, and are subject to a specific computational ordering which, although arbitrary, must remain consistent. We can now simplify Eq. (3.64) further by making use of the structure of Eq. (3.59), thus allowing us to write:

$$Z_n = \sum_{X\in[-d,d]} |\psi_n(X)|^2 \boldsymbol{s}_X \boldsymbol{s}_X^{\mathrm{T}}, \tag{3.66}$$

where, by definition, each $\boldsymbol{s}_X \boldsymbol{s}_X^{\mathrm{T}}$ is an $N \times N$ positive semidefinite matrix with rank zero or one. In fact, the only rank zero case of $\boldsymbol{s}_X \boldsymbol{s}_X^{\mathrm{T}}$ is the basis state with all spin-zeroes; therefore, we can simplify our expression further by utilising this fact, along with the fact that $\boldsymbol{s}_{-X} = -\boldsymbol{s}_X$:

$$Z_n = \sum_{X=1}^{d} \left(|\psi_n(X)|^2 + |\psi_n(-X)|^2 \right) \boldsymbol{s}_X \boldsymbol{s}_X^{\mathrm{T}}. \tag{3.67}$$

In particular, Eq. (3.67) allows us to identify a highly useful scalar measure: the largest eigenvalue of Z_n, which we will label as $Z_n^{\max}$. The nature of $Z_n^{\max}$ can be understood qualitatively by considering the extremal cases:

- **Perfect Fock-space localisation** (IPR = 1):

  Z_n will be a rank one positive semidefinite matrix with $Z_n^{\max} = \mathrm{Tr}(Z_n) \in \mathbb{Z}^+$. In this case, $Z_n^{\max}$ can be interpreted simply as the number of non-zero spins in the n-th many-body eigenstate's only possible configuration.

- **Fock-space delocalisation** (IPR = $1/\mathcal{N}$):

  Z_n will consist of the sum of $(\mathcal{N}-1)/2$ rank one positive semidefinite matrices with $Z_n^{\max} \approx 2/3$.

In the case of perfect Fock-space localisation, Eq. (3.67) immediately recovers the correct expression calculated previously in Eq. (3.59). The case of complete Fock-space delocalisation, however, requires a slightly more complex argument, which will now explore.

Consider a matrix created via the concatenation of all of the $\{\boldsymbol{s}_X\}$ like so:

$$S = \left(\boldsymbol{s}_{-d}\boldsymbol{s}_{-d+1}\cdots\boldsymbol{s}_d\right). \tag{3.68}$$

This allows us to rewrite Eq. (3.67) equivalently as:

$$Z_n = \begin{pmatrix}\boldsymbol{s}_{-d}\cdots\boldsymbol{s}_d\end{pmatrix}\begin{pmatrix}|\psi_n(-d)|^2 & \cdots & 0\\ \vdots & \ddots & \vdots\\ 0 & \cdots & |\psi_n(d)|^2\end{pmatrix}\begin{pmatrix}\boldsymbol{s}_{-d}^{\mathrm{T}}\\ \vdots\\ \boldsymbol{s}_d^{\mathrm{T}}\end{pmatrix}, \tag{3.69}$$

which is equivalent to an SVD decomposition, much like Eq. (3.84). If we now assume the case of complete Fock-space delocalisation, then this allows us to state: $|\psi_n(X)|^2 = 1/\mathcal{N}\ \forall\ X \in [-d,d]$. By using this fact, along with Eq. (3.68), we can rewrite Eq. (3.69) as:

$$Z_n\Big|_{\mathrm{IPR}=\frac{1}{\mathcal{N}}} = \frac{1}{\mathcal{N}}SS^{\mathrm{T}}. \tag{3.70}$$

By noting the structure of our $\boldsymbol{s}_X^{\mathrm{T}}$ vectors, one can deduce that SS^{T} is proportional to the identity matrix, with proportionality constant dependent on our choice of symmetry sector like so:

$$SS^{\mathrm{T}} = \begin{cases}\left(3^{N-1}+1\right)\mathbb{1} & \text{if } H = H^+\\ \left(3^{N-1}-1\right)\mathbb{1} & \text{if } H = H^-\end{cases} \tag{3.71}$$

where the symmetry sectors, H^+ and H^-, are described in Eq. (3.22). We can now

substitute Eq. (3.71) into Eq. (3.70), and thus obtain:

$$Z_n\Big|_{\mathrm{IPR}=\frac{1}{\mathcal{N}}} = \begin{cases} 2\left(\frac{3^{N-1}+1}{3^N+1}\right)\mathbb{1} \sim \frac{2}{3}\mathbb{1} & \text{if } H = H^+ \\ 2\left(\frac{3^{N-1}-1}{3^N+1}\right)\mathbb{1} \sim \frac{2}{3}\mathbb{1} & \text{if } H = H^- \end{cases} \tag{3.72}$$

3.3.3 Zero-Mode Correlations

As we show next, for the zero mode the correlation matrix Δ_0 further decomposes into four sectors, each pertaining the S^x or S^y component and additionally confined to the sublattice of even or odd sites. This structure follows directly from the symmetry constraints, and hence holds at all strengths of disorder.

To arrive at these features, we first note that for all states time-reversal symmetry implies

$$\langle\psi_k|S^y_n S^x_m|\psi_k\rangle = 0 \text{ if } n \neq m, \tag{3.73}$$

as this amounts to an expectation value of a Hermitian operator with imaginary matrix elements, evaluated with a real-valued eigenvector. This constraint does not apply for $n = m$ as the matrix product $S^y_n S^x_n$ is not Hermitian (it is furthermore not simply related to S^z_n, in contrast to the case of spin 1/2). However, for the zero mode the chiral symmetry further implies

$$\begin{aligned} \langle\psi_0|S^x_n S^x_m|\psi_0\rangle &= \langle\mathcal{X}\psi_0|S^x_n S^x_m|\mathcal{X}\psi_0\rangle \\ &= (-1)^{n-m}\langle\psi_0|S^x_n S^x_m|\psi_0\rangle, \end{aligned} \tag{3.74}$$

and analogously

$$\langle\psi_0|S^y_n S^y_m|\psi_0\rangle = (-1)^{n-m}\langle\psi_0|S^y_n S^y_m|\psi_0\rangle, \tag{3.75}$$

$$\langle\psi_0|S^x_n S^y_m|\psi_0\rangle = (-1)^{n-m-1}\langle\psi_0|S^x_n S^y_m|\psi_0\rangle, \tag{3.76}$$

$$\langle\psi_0|S^y_n S^x_m|\psi_0\rangle = (-1)^{n-m-1}\langle\psi_0|S^y_n S^x_m|\psi_0\rangle, \tag{3.77}$$

which are relations that hold for all n and m. In combination with the constraint (3.73) from time-reversal symmetry, these relations imply that the blocks $\Delta_{0,nm}$ are all diagonal, and furthermore vanish if $n-m$ is odd. Thus, for the zero mode the Δ correlation matrix decomposes into four independent blocks,

$$\Delta_0 = \Delta_0^{x,\mathrm{even}} \oplus \Delta_0^{x,\mathrm{odd}} \oplus \Delta_0^{y,\mathrm{even}} \oplus \Delta_0^{y,\mathrm{odd}}, \tag{3.78}$$

where the superscripts denote the supporting spin component and sublattice. Including

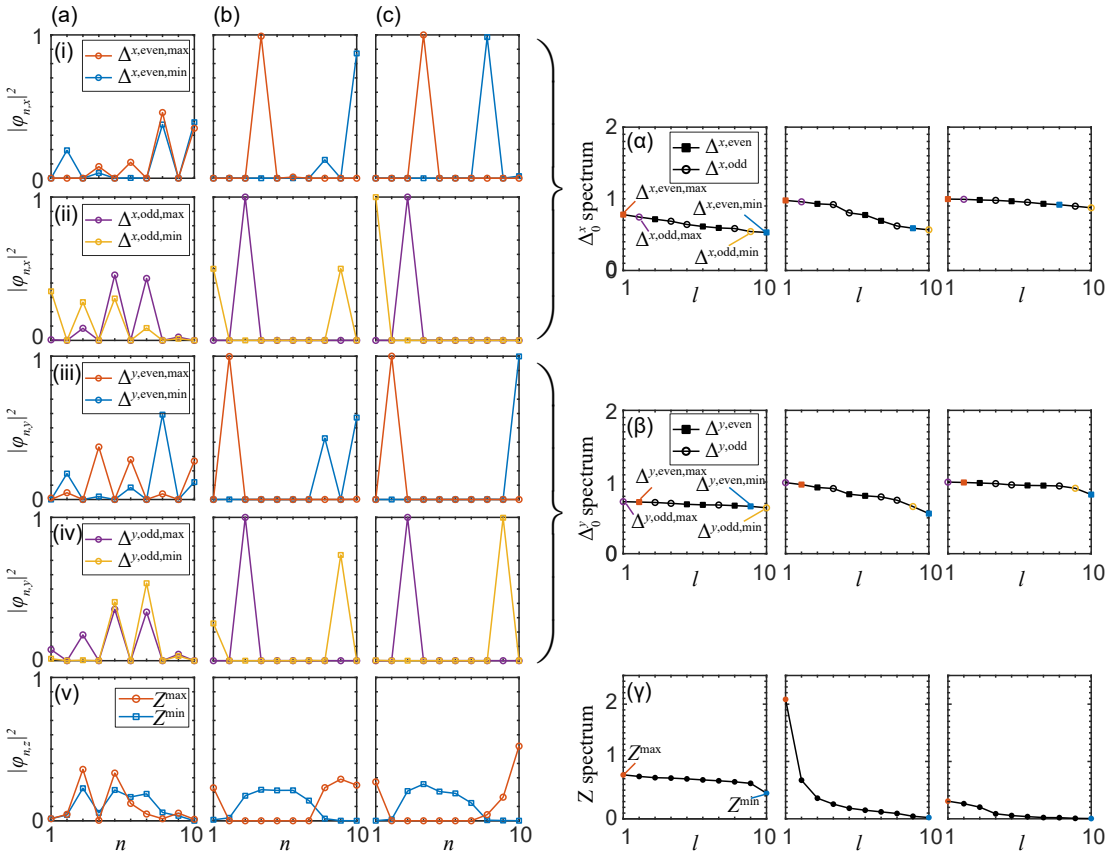

Figure 3.3: Spin correlations in a zero mode of the spin-1 Ising chain, as quantified by the spin correlation matrix $\mathcal{C}$ in an individual realisation of the disorder with strength (a) $W = 1$, (b) $W = 8$, (c) $W = 20$. At any disorder, the correlation matrix fragments into 5 sectors. Panels (i-v) show the correlation eigenvectors with the largest and smallest correlation eigenvalue in each sector. The corresponding correlation eigenvalue spectra are shown in the adjacent panels (α-γ). For weak disorder, these eigenvalues lie around the ergodic value 2/3, while for strong disorder they approach quantised values 1 (for Δ) and 0 (for Z).

the spin correlations from Z_0, we can, therefore, identify five independent elementary spin correlation patterns for the zero mode.

3.3.4 Numerical Illustration

This structure of the spin correlations is illustrated in Fig. 3.3, where we show correlation eigenstates with minimal and maximal correlation eigenvalues in a typical individual disorder realisation at (a) weak, (b) moderate and (c) strong disorder ($W = 1, 8, 20$, respectively). Subpanels (i-iv) show the four types of correlation eigenvectors from Δ_0, while

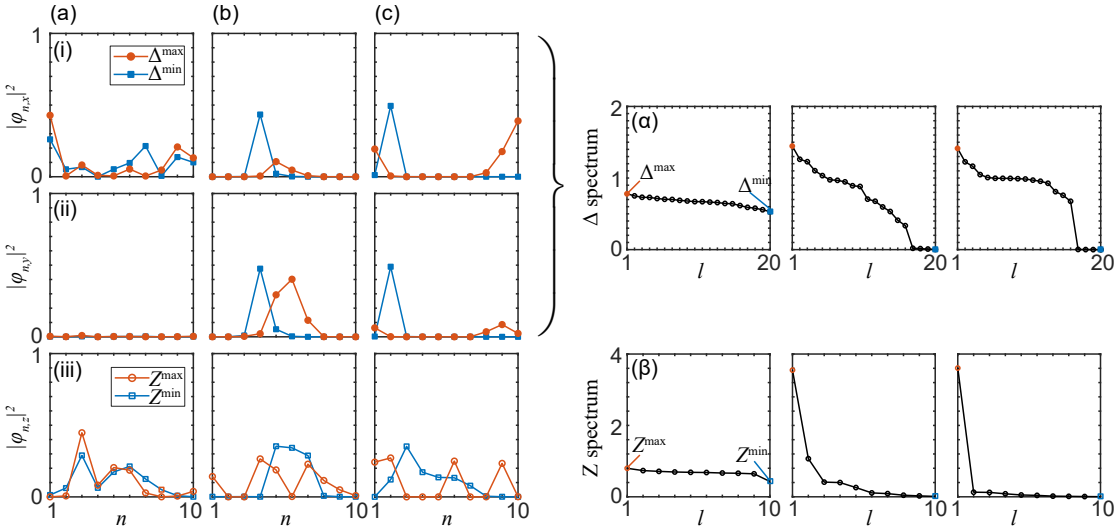

Figure 3.4: Spin correlations for a nonzero mode close to the band centre, in analogy to Fig. 3.3. Note that the correlation eigenvectors displayed in subpanels (i) and (ii) now belong to the same correlation eigenvalues, hence, represent their x and y components, as these no longer separate, also not with respect to the sublattice. Therefore, only two types of elementary spin correlations exist for such nonzero modes. As shown in subpanels (α) and (β), the correlation spectra again become quantised for strong disorder, reflecting the number of spins with finite s_z in the approached basis state $|\mathbf{s}\rangle$.

panel (v) shows correlation eigenvectors from Z_0. The position of these eigenvectors in the occupation spectrum is depicted in the adjacent subpanels (α-γ).

While the predicted fragmented structure holds at all disorder strengths, the correlation eigenvectors from Δ_0 display a noticeable trend from being extended over the whole system for weak disorder, to becoming highly localised on individual spins at strong disorder. In contrast, we notice that the Z-correlation eigenvectors more sensitively quantify the hybridisation of neighbouring spins, a feature that will be important in the subsequent sections. In conjunction, the correlation spectra from Δ_0 and Z_0 both move away from the ergodic value 2/3, approaching the quantised values 1 and 0, respectively, as expected for a many-body localised state.

For comparison, Fig. 3.4 shows the analogous spin correlation features in a representative nonzero mode. Note that subpanels (i) and (ii) now refer to the x and y components of the same Δ-correlation eigenvectors, as these correlations no longer separate. Furthermore, each of these eigenvectors now populates both the even and odd sublattices. Otherwise, we notice the same qualitative tendencies as for the zero mode—the Δ spin

correlations again become highly localised for strong disorder, while the Z correlations remain more extended, and the corresponding correlation spectra move away from their ergodic values 2/3 to quantised values, which now depend on the number of finite spins in the approached basis state $|\mathbf{s}\rangle$. In the example, this state has four finite spins, so that there are four nearly-vanishing Δ-correlation eigenvalues, and a dominant Z-correlation eigenvalue approaching the value 4.

By surveying different examples we can certify that these qualitative features are typical for individual states in fixed disorder realisations, with the variations at moderate and strong disorder pointing to different spin hybridisation patterns. As indicated above, the Z_0-eigenvector with maximal eigenvalue $Z_0^{\max}$ is particularly useful to characterise the excitation patterns of the zero mode above the reference state $|\mathbf{0}\rangle$ for the zero mode, and analogously above the reference states $|\mathbf{s}\rangle$ for nonzero modes. These insights will inform our discussion of the quantitative differences in their localisation, on which we focus in the following sections.

3.4 Zero-Mode Delocalisation

We now turn to the second key feature of the zero mode, which pertains to the fact that it is less localised than the nonzero modes. In this section, we establish this feature based on numerical results, while the theoretical explanation is provided in the following section.

3.4.1 Measures of Localisation

To address this question, we consider a number of complementary indicators of localisation, whose general properties we summarise first.

As a general measure of localisation, we consider the bipartite von Neumann entanglement entropy [108]. This is defined for each normalised eigenstate $|\psi_k\rangle$ as

$$S_k = -\operatorname{Tr}\left(\rho^{(k)} \ln \rho^{(k)}\right), \tag{3.79}$$

where $\rho^{(k)} = \operatorname{Tr}_B |\psi_k\rangle\langle\psi_k|$ is the reduced density matrix of a subsystem A, obtained by tracing out the complement B. We take A to be a contiguous subchain of length $N_A = N/2$, hence half the length of the total system. In delocalised states, the von Neumann entropy is large, and should be well approximated by the Page value for completely ergodic states [101], $S_k \simeq N_A \ln 3 - \frac{1}{2}$. Therefore, the entropy grows linearly with the system size,

which manifests a volume law. In contrast, in a localised state the von Neumann entropy is expected to be small, and on average independent of the system size, which manifests an area law. The value of the entropy can then be taken as a proxy for the effective localisation length [1]. In a basis state $|\mathbf{s}\rangle$, the entanglement entropy $S_{\mathbf{s}} = 0$ vanishes as these states are all separable.

The concept of this entanglement entropy can be extended past pure states to also account for mixed states; however, for mixed states, the entanglement entropy is somewhat of a misnomer, as it is more of a measure of correlations rather than actual entanglement. Nevertheless, we will continue to use the term entanglement entropy here for convenience. Extending this concept makes use of the Schmidt decomposition of a state, which is defined as:

$$|\psi\rangle_{AB} = \sum_{\alpha} \lambda_\alpha \, |u_\alpha\rangle_A \otimes |v_\alpha\rangle_B \,, \tag{3.80}$$

where the states, $|u_\alpha\rangle_A$ and $|v_\alpha\rangle_B$, form an orthogonal basis of their respective Hilbert spaces, and the Schmidt coefficients $\{\lambda_\alpha\}$ are subject to the constraint: $\lambda_\alpha \geq 0 \, \forall \, \alpha$. Also, if $|\psi\rangle_{AB}$ is orthonormal, then this is reflected by the additional constraint: $\sum_\alpha \lambda_\alpha^2 = 1$. The Schmidt decomposition can, in a sense, be interpreted as the decomposition that minimally entangles the two subsystems, A and B. The more general entanglement entropy is thus defined as:

$$S = -\sum_{\alpha} \lambda_\alpha^2 \ln \lambda_\alpha^2. \tag{3.81}$$

Now, an important question arises: how do we calculate the Schmidt coefficients? To proceed, we first rewrite a given state as:

$$|\psi\rangle = \sum_{\alpha\beta} \psi_{\alpha\beta} \, |\alpha\rangle \otimes |\beta\rangle \,, \tag{3.82}$$

where each of the amplitudes $\{\psi_{\alpha\beta}\}$ are now interpreted as the indices of a matrix i.e. $\psi_{\alpha\beta}$ is the matrix coefficient corresponding to the α-th row of the β-th column. We will refer to this matrix as Ψ.

Next, we decompose this matrix via *singular-value decomposition* (SVD), which is defined as:

$$\Psi = L \Lambda R^\dagger, \tag{3.83}$$

where $\Lambda \in \mathbb{C}^{m \times n}$ is diagonal, and $L \in \mathbb{C}^{m \times m}$ and $R \in \mathbb{C}^{n \times n}$ are unitary. Performing SVD

on our matrix of state amplitudes provides us with a matrix of the form:

$$\Psi = \begin{pmatrix} |\psi_1\rangle_A \cdots |\psi_\alpha\rangle_A \cdots \end{pmatrix} \begin{pmatrix} \lambda_1 & \cdots & \cdots & 0 \\ \vdots & \ddots & & \vdots \\ \vdots & & \lambda_\alpha & \vdots \\ 0 & \cdots & \cdots & \ddots \end{pmatrix} \begin{pmatrix} {}_B\langle\psi_1| \\ \vdots \\ {}_B\langle\psi_\alpha| \\ \vdots \end{pmatrix}, \tag{3.84}$$

where the diagonal matrix provides us with the Schmidt coefficients we seek. In our case, it is most convenient to bisect our system into two subsystems of equal size so that the number of Schmidt coefficients is maximised, leading to better statistics due to more data.

To quantify the degree of Fock-space localisation, we make use of the inverse participation ratio (IPR) in the basis (3.10),

$$\mathrm{IPR}_k = \sum_{\mathbf{s}} |\langle \mathbf{s}|\psi_k\rangle|^4. \tag{3.85}$$

In the case of perfect Fock-space localisation, the IPR goes to unity, while in the case of complete delocalisation, the IPR goes to $1/\mathcal{N}$.

We also consider the intensity

$$I_k = |\langle \mathbf{0}|\psi_k\rangle|^2 \tag{3.86}$$

of the states with the special state $|\mathbf{0}\rangle$, which we expect to become large for the zero mode at large disorder, while for ergodic states again $I_k \simeq 1/\mathcal{N}$.

3.4.2 Numerical Results

At strong disorder, the zero mode is expected to have a large overlap $I_0 = |\langle \mathbf{0}|\psi_0\rangle|^2$ with the state $|\mathbf{0}\rangle$, in which the contribution from the field $\mathbf{h}$ vanishes. This is verified in Fig. 3.5(a), which shows that the disorder-averaged $\overline{I_0}$ rises sharply at disorder strengths $W \simeq 4$. In contrast, the corresponding average $\overline{I_{\neq 0}} \sim O(\mathcal{N}^{-1})$ for the nonzero modes is negligible for all disorder strengths. Nonetheless, overall the zero mode is noticeably less localised in Fock space than the nonzero modes, as evidenced in Fig. 3.5(b) by an inverse participation ratio $\overline{\mathrm{IPR}_0}$ that is reduced relative to $\overline{\mathrm{IPR}_{\neq 0}}$, and in Fig. 3.5(c) by a bipartite entanglement entropy $\overline{S_0}$ that is increased relative to $\overline{S_{\neq 0}}$. Therefore, for strong disorder the nonzero modes approach basis states $|\mathbf{s}\rangle$ with $\mathbf{s} \neq \mathbf{0}$ more quickly than the zero mode approaches the basis state $|\mathbf{0}\rangle$. As we explain in Sec. 3.5, the residual hybridisation of basis states can be quantified by the maximal Z spin-correlation eigenvalue $Z_k^{\max}$, whose

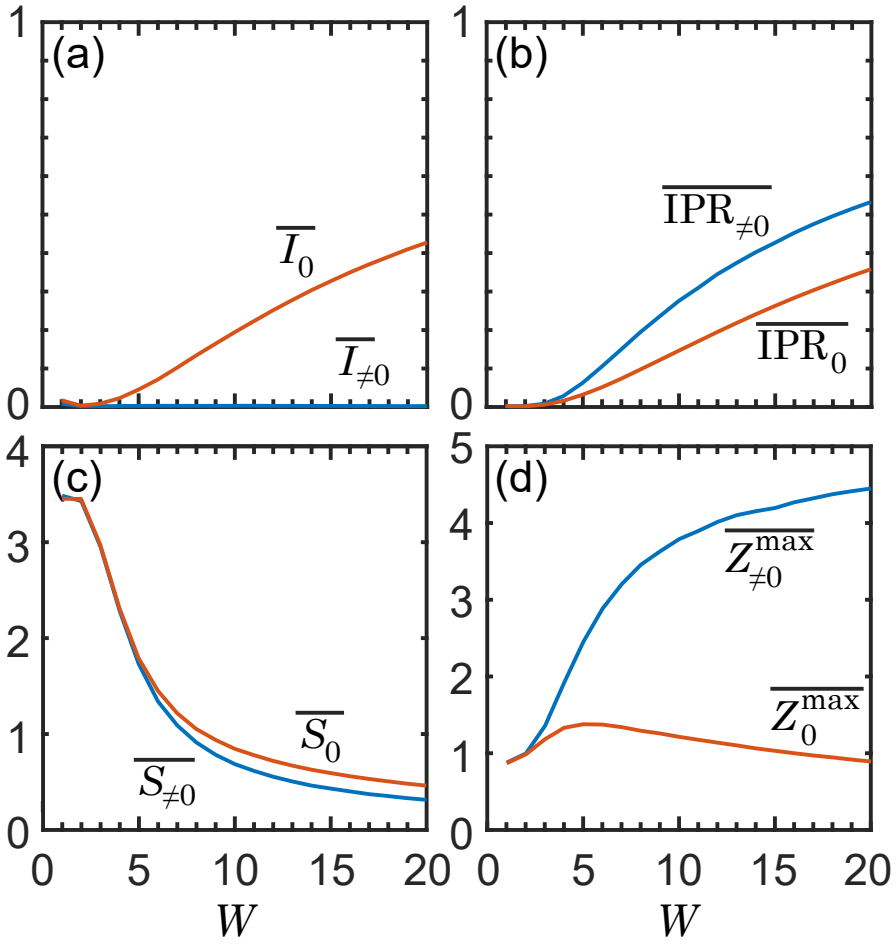

Figure 3.5: Disorder-averaged measures of localisation for the zero mode (light red) and nonzero modes (dark blue) as a function of disorder strength W. (a) Overlap I_k with the basis state $|\mathbf{0}\rangle$, as defined in Eq. (3.86). For the zero mode, $\overline{I_0}$ increases with increasing disorder strength, reaching $\overline{I_0} \sim 1/2$ at around $W = 20$. For nonzero modes, the corresponding average $\overline{I_{\neq 0}} = O(\mathcal{N}^{-1})$ remains negligible at all disorder strengths. As shown in (b), the nonzero modes nonetheless have a larger extent of Fock-space localisation, as quantified by the inverse participation ratio IPR [see Eq. (3.85)], and hence approach an eigenstate $|\mathbf{s}\rangle$ with $\mathbf{s} \neq \mathbf{0}$ more quickly than the zero mode approaches $|\mathbf{0}\rangle$. This relative delocalisation of the zero mode is confirmed in panel (c) by the bipartite entanglement entropy (3.79), which is enhanced for the zero mode. We also see that, in the low-disorder regime, the entropies of both the zero and nonzero modes lie close to the Page value of 3.89 for $N = 8$. Panel (d) shows the maximal Z spin correlation eigenvalue $Z_k^{\max}$, which quantifies the residual hybridisation of these states in the strongly localised regime, as further discussed in Sec. 3.5.

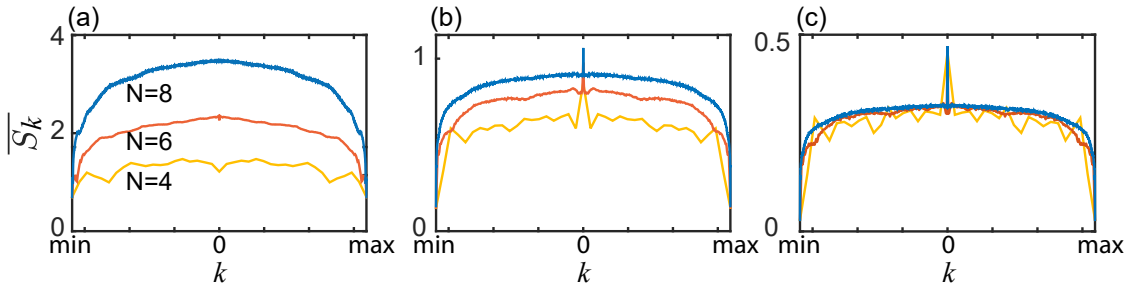

Figure 3.6: Averaged entanglement entropy of energy eigenstates ordered by their energy, with the resulting mode index centred at the zero mode, for disorder strengths (a) $W = 1$, (b) $W = 8$, (c) $W = 20$, and system sizes $N = 4, 6, 8$. The entanglement entropy of the zero mode is enhanced in the localised regime, by an amount that is independent of the accessible system sizes.

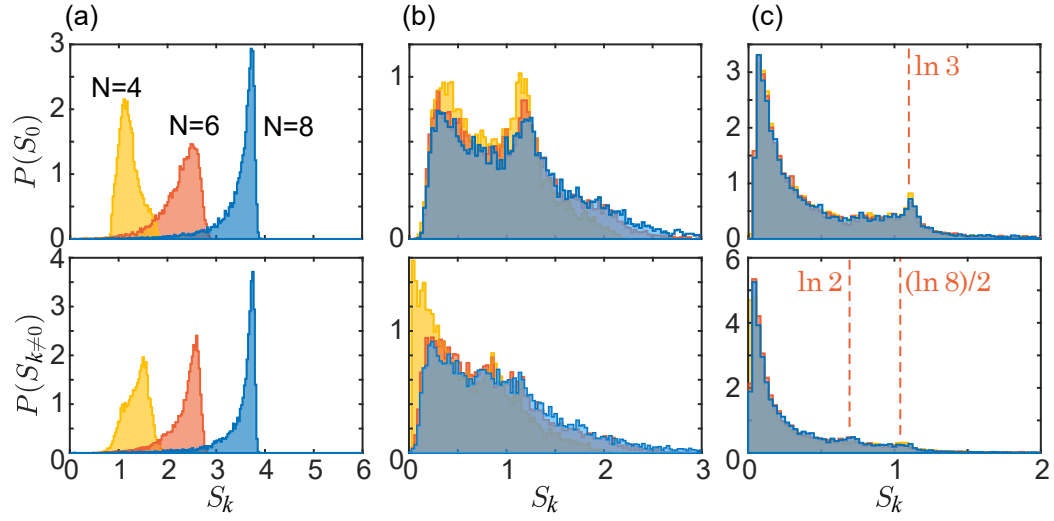

Figure 3.7: Distributions of the entanglement entropy for zero modes (top panels) and nonzero modes (bottom panel), for parameters as in Fig. 3.6. From moderate disorder, the zero mode shows a significant enhancement of entropies $S \gtrsim 1$, with the indicated value $\ln 3$ identified in Sec. 3.5. Nonzero modes display less pronounced features at smaller characteristic values, $\ln 2$ and $(\ln 8)/2$.

average is shown in Fig. 3.5(d).

In Fig. 3.6, we show the disorder-averaged entanglement entropy $\overline{S_k}$ as a function of the mode index k, obtained by ordering all states by their energy and centring the resulting index at the zero mode. The entropy of the zero mode is clearly enhanced in the localised regime, by an amount that is independent of the accessible system sizes, hence remaining consistent with an area law. This well-confined relative delocalisation peak also confirms

that the enhancement is restricted to exact zero modes, and not shared, e.g., by nonzero modes very close to the band centre.

As shown by the statistical distribution functions of the entanglement entropy in Fig. 3.7, this delocalising tendency can be attributed to an accumulation of zero modes with entropy S_0 slightly above 1, to be identified as $S_0 \simeq \ln 3$ in the following section. This accumulation is already well pronounced at moderate values of disorder (panel b), and is well defined at very large values of disorder (panel c), suggesting that it arises from a specific delocalisation mechanism. In contrast, nonzero modes display accumulations at smaller characteristic values of the entropy, to be identified as $\ln 2$ and $(\ln 8)/2$, which hints towards a competition of several distinct delocalisation mechanisms. We will identify the underlying hybridisation patterns in the following section.

3.5 Dimer Hybridisation

We explain the relative delocalisation of the zero mode based on quasi-degenerate perturbation theory at relatively large disorder. This reveals a characteristic dimer hybridisation pattern involving three collective basis states localised on neighbouring spins, while nonzero modes support a much wider range of hybridisation patterns.

3.5.1 Perturbation Theory Set-up

Separating the Hamiltonian into a dominant part $H^{(0)} = \sum_{n=1}^{N} h_n S_n^z$ and a perturbation $V = J \sum_{n=1}^{N} S_n^x S_{n+1}^x$, the unperturbed eigenstates of the system coincide with the canonical basis states $|\mathbf{s}\rangle$ defined in Eq. (3.10), with the zero mode given by $|\psi_0\rangle = |\mathbf{0}\rangle$. These states carry energy $E_{\mathbf{s}}^{(0)} = \sum h_n s_n^z$, have vanishing entanglement entropy $S_{\mathbf{s}}^{(0)} = 0$, Fock-space localisation measures, $\mathrm{IPR}_{\mathbf{s}}^{(0)} = 1$ and $I_{\mathbf{s}}^{(0)} = \delta_{\mathbf{s},\mathbf{0}}$, and quantised correlation eigenvalues from Δ and Z.

These characteristics define the typical features of all modes in the strongly localised regime, where any hybridisation is absent. The question is how the modes gradually delocalise due to resonant interactions at weaker disorder. We show that this involves distinct hybridisation processes on adjacent spins, leading to characteristic features in the entropy, inverse participation ratio, and spin correlations.

We first identify the resonance conditions in general terms, and then derive the hy-

bridisation patterns and their characteristic signatures, which we further support with numerical results.

3.5.2 Resonance Conditions

In first-order perturbation theory, the hybridisation of the zero mode with other states $|\mathbf{s}\rangle$ is strongly suppressed by energy denominators $E_{\mathbf{s}}^{(0)}$. In principle, hybridisation can set in for states with individual $|h_n| \leq J$, for which individual spins can align freely. However, at least two sites need to be involved to retain positive parity, and furthermore these configurations have vanishing perturbation matrix elements unless sites neighbour each other. On the other hand, it should then suffice that $|h_n| - |h_{n+1}| \simeq J$, instead of both $|h_n|, |h_{n+1}| \simeq J$ individually, implying that such disorder configurations should be dominant as they require fewer constraints.

We can verify the above reasoning by examining all excitations patterns above the background state $|\mathbf{0}\rangle$. Amongst the excitations involving neighbouring spins (hence relevant in the first order of the perturbation), only two patterns are allowed by parity, chiral, and time-reversal symmetry, namely those obtained from state $|\mathbf{0}\rangle$ by terms generated via application of the matrix combinations, $iS_n^x S_{n+1}^y$ and $iS_n^y S_{n+1}^x$. These can be conveniently combined into excitation operators

$$\hat{\Phi}_n^{\pm} \equiv iS_n^x S_{n+1}^y \mp iS_n^y S_{n+1}^x, \tag{3.87}$$

leading to the perturbative ansatz

$$|\psi_0\rangle \simeq \left(1 + \sum_n \phi_n^+ \hat{\Phi}_n^+ + \sum_n \phi_n^- \hat{\Phi}_n^-\right)|\mathbf{0}\rangle, \tag{3.88}$$

where $\phi_n^{\pm}$ are the amplitudes of the two excitation fields. Expanding the condition $H|\psi_0\rangle = 0$ in orders of the relative interaction strength, we then obtain the perturbatively closed coupled equations

$$0 = (\phi_n^+ + \phi_n^-)h_{n+1} + (-\phi_n^+ + \phi_n^-)h_n + J, \tag{3.89}$$

$$0 = (\phi_n^+ + \phi_n^-)h_n + (-\phi_n^+ + \phi_n^-)h_{n+1}, \tag{3.90}$$

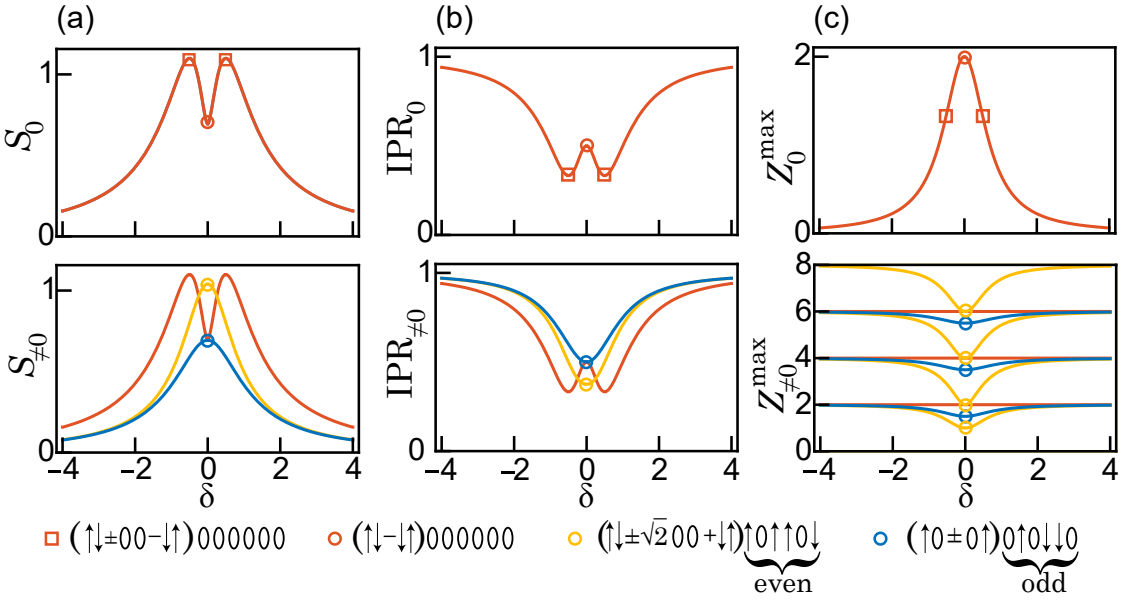

Figure 3.8: Analytical predictions for the localisation characteristics of zero modes (top) and nonzero modes (bottom) as a function of the hybridisation parameter δ from quasi-degenerate perturbation theory (see text). (a) Bipartite entanglement entropy, (b) inverse participation ratio, (c) leading Z spin-correlation eigenvalue $Z_k^{\max}$. Quantities arising from the zero-mode hybridisations (3.97) and (3.98) are given in medium-dark red. In the case of nonzero modes, these hybridisations can still appear when embedded into a state in which an even number of the remaining spins have a finite S^z component. For the nonzero modes, further configuration scenarios appear from the hybridisations (3.103) (again embedded into states with an even number of remaining nonzero spins, light yellow) and (3.107) (embedded into states with an odd number of remaining nonzero spins, dark blue). Examples of these hybridisation patterns are shown at the bottom of the figure.

whereupon

$$\phi_n^+ = \frac{J}{2(h_n - h_{n+1})}, \tag{3.91}$$

$$\phi_n^- = \frac{-J}{2(h_n + h_{n+1})}. \tag{3.92}$$

Thus, one of the two fields becomes large when $|h_n| \simeq |h_{n+1}|$, which agrees with the resonance conditions identified above.

3.5.3 Zero-Mode Hybridisation Patterns

To describe such resonant disorder configurations more accurately, we resort to quasi-degenerate perturbation theory in the subspace of the hybridising spins, taken without loss of generality as $(n, n+1) = (1, 2)$. We start with dimer hybridisations of even parity, assuming initially that they are embedded into a chain where the remaining spins are unhybridised,

$$|\psi_0\rangle = |\psi_0\rangle_{\text{dimer}} \otimes |\mathbf{0}\rangle. \tag{3.93}$$

We first consider the vicinity of the resonance condition (3.91), where we write $h_1 = \bar{h} + \delta/2$, $h_2 = \bar{h} - \delta/2$ while setting $J = 1$. Ordering the even-parity states as $|1,1\rangle$, $|1,-1\rangle$, $|0,0\rangle$, $|-1,1\rangle$, $|-1,-1\rangle$, the reduced Hamiltonian

$$H_{12}^{+} = [\bar{h}(S_1^z + S_2^z) + \delta/2(S_1^z - S_2^z) + JS_1^x S_2^x]_{+} \tag{3.94}$$

$$= \begin{pmatrix} 2\bar{h} & 0 & 1/2 & 0 & 0 \\ 0 & \delta & 1/2 & 0 & 0 \\ 1/2 & 1/2 & 0 & 1/2 & 1/2 \\ 0 & 0 & 1/2 & -\delta & 0 \\ 0 & 0 & 1/2 & 0 & -2\bar{h} \end{pmatrix} \tag{3.95}$$

then separates into three sectors, with states, $|1,1\rangle$ and $|-1,-1\rangle$, gapped out by an energy $\simeq \pm 2\bar{h}$, while the zero mode is contained in the quasi-degenerate sector

$$\tilde{H}_{12}^{+} = \begin{pmatrix} \delta & 1/2 & 0 \\ 1/2 & 0 & 1/2 \\ 0 & 1/2 & -\delta \end{pmatrix} \tag{3.96}$$

spanned by the states $|1,-1\rangle$, $|0,0\rangle$, $|-1,1\rangle$. Diagonalising this sector, we find two states of finite energy $\pm\sqrt{\delta^2 + 1/2}$, to which we will come back later, as well as a zero mode

$$|\psi_0\rangle_{\text{dimer}} = |1,-1\rangle - 2\delta|0,0\rangle - |-1,1\rangle \tag{3.97}$$

of vanishing energy, which we will call the dimer zero mode. Near the resonance condition (3.92), the same considerations apply upon writing $h_1 = \bar{h} + \delta/2$, $h_2 = -\bar{h} + \delta/2$ with the roles of the states, $(|1,1\rangle, |-1,-1\rangle)$ and $(|1,-1\rangle, |-1,1\rangle)$, interchanged, leading to zero-mode hybridisations

$$|\psi_0\rangle_{\text{dimer}} = |1,1\rangle - 2\delta|0,0\rangle - |-1,-1\rangle. \tag{3.98}$$

In both cases, the bipartite entanglement entropy of the dimer zero mode is given by

$$S_{0,\mathrm{dimer}} = \ln\bigl(2+4\delta^2\bigr) - \frac{2\delta^2 \ln\bigl(4\delta^2\bigr)}{1+2\delta^2}, \tag{3.99}$$

and the inverse participation ratio is given by

$$\mathrm{IPR}_{0,\mathrm{dimer}} = \frac{1+8\delta^4}{2(1+2\delta^2)^2}. \tag{3.100}$$

On the dimer, the Z correlation matrix has a single finite eigenvalue

$$Z^{\max}_{0,\mathrm{dimer}} = \frac{2}{1+2\delta^2}, \tag{3.101}$$

which we interpret as the maximal eigenvalue as for the remaining spins $Z_{0,nn} = 0$ vanishes [1].

The top row in Fig. 3.8 displays these characteristics of the dimer zero mode as a function of the detuning δ. The entropy has a stationary point at $\delta = 0$ with the value $S_0 = \ln 2$, where $\mathrm{IPR}_0 = 1/2$ and $Z^{\max}_0 = 2$, and two stationary points at $\delta = \pm 1/2$ with the value $S = \ln 3$, where $\mathrm{IPR}_0 = 1/3$ and $Z^{\max}_0 = 4/3$.

We note that several of these hybridisation patterns can be embedded along different positions of the zero mode. The entropy then arrives from the dimers spanning the bipartite partition point, and still adheres to Eq. (3.99). The resulting inverse participation ratio is the product of those of all hybridised dimers, so that Eq. (3.100) provides an upper bound for IPR_0. Furthermore, the Z correlation matrix decomposes into independent blocks, so that Eq. (3.101) provides a lower bound for the maximal Z correlation eigenvalue $Z^{\max}_0$.

3.5.4 Hybridisation Patterns of Nonzero Modes

We next identify the dominant hybridisation patterns of nonzero modes,

$$|\psi\rangle = |\psi\rangle_{\mathrm{dimer}} \otimes |\mathbf{s}'\rangle, \tag{3.102}$$

of which there is a much wider variety, each having its own characteristic signatures.

We start with dimer hybridisations of even parity, embedded into a chain where the remaining spins $|\mathbf{s}'\rangle$ also have even parity. Assuming again first $h_1 = \bar{h}+\delta/2$, $h_2 = \bar{h}-\delta/2$, the dimers of even parity are still described by the reduced Hamiltonian (3.95), but all

[1] In this regime this eigenvalue also determines the four-fold degenerate eigenvalue $\Delta_{0,\mathrm{dimer}} = (4 - Z^{\max}_{0,\mathrm{dimer}})/4$ of the Δ correlation matrix (with one eigenvalue per fragmented sector), while for the remaining spins $\Delta_{0,nn} = \mathbb{1}$.

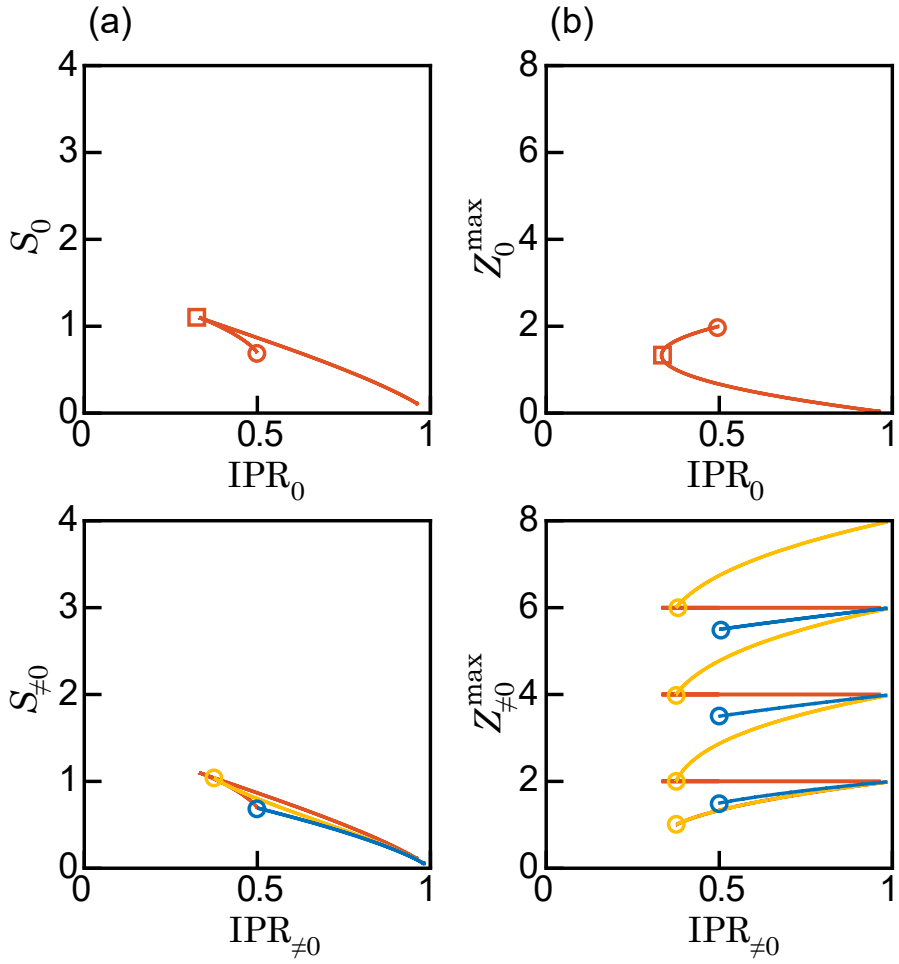

Figure 3.9: Analytical predictions for correlations between the localisation characteristics of zero modes (top) and nonzero modes (bottom), following from the results shown in Fig. 3.8.

five resulting dimer states have to be taken into account. Alongside the hybridisation pattern (3.97), this includes the gapped states $|1,1\rangle$ and $|-1,-1\rangle$, which remain separable, as well as the two finite-energy hybridisations

$$|\psi_{+,\pm}\rangle_{\text{dimer}} = (\delta \pm \sqrt{\delta^2 + \frac{1}{2}})|1,-1\rangle + |00\rangle + (-\delta \pm \sqrt{\delta^2 + \frac{1}{2}})|-1,1\rangle \tag{3.103}$$

from the sector (3.95). In the dimer subspace $|1,0\rangle$, $|0,1\rangle$, $|0,-1\rangle$, $|-1,0\rangle$ with odd parity,

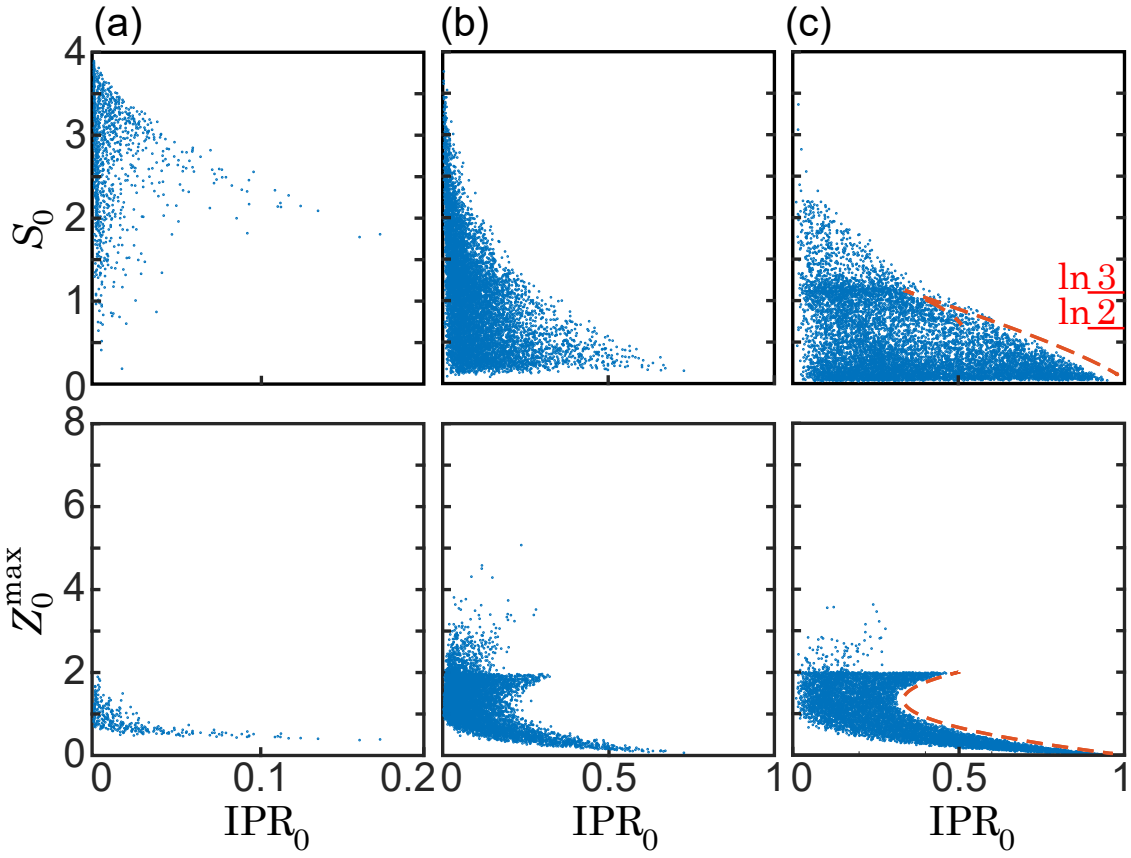

Figure 3.10: Scatter plot of localisation characteristics of the zero mode for disorder strengths (a) $W = 1$, (b) $W = 8$, (c) $W = 20$. In (c), the dashed lines indicate the predicted analytical bounds, see the top panels in Fig. 3.9(a,b). Note the different scale on the horizontal axis in panel (a).

the reduced Hamiltonian takes the form

$$H_{12}^{-} = [\bar{h}(S_1^z + S_2^z) + \delta(S_1^z - S_2^z) + JS_1^x S_2^x]_- \tag{3.104}$$

$$= \begin{pmatrix} \bar{h}+\delta/2 & 1/2 & 1/2 & 0 \\ 1/2 & \bar{h}-\delta/2 & 0 & 1/2 \\ 1/2 & 0 & -\bar{h}+\delta/2 & 1/2 \\ 0 & 1/2 & 1/2 & -\bar{h}-\delta/2 \end{pmatrix}, \tag{3.105}$$

leading to pairwise hybridisation

$$|\psi_{-,\pm,1}\rangle_{\text{dimer}} = (\delta \pm \sqrt{1+\delta^2})|1,0\rangle + |0,1\rangle, \tag{3.106}$$

$$|\psi_{-,\pm,2}\rangle_{\text{dimer}} = (\delta \pm \sqrt{1+\delta^2})|0,-1\rangle + |-1,0\rangle \tag{3.107}$$

only.

Overall, we therefore arrive at seven hybridisation patterns and two nonhybridised

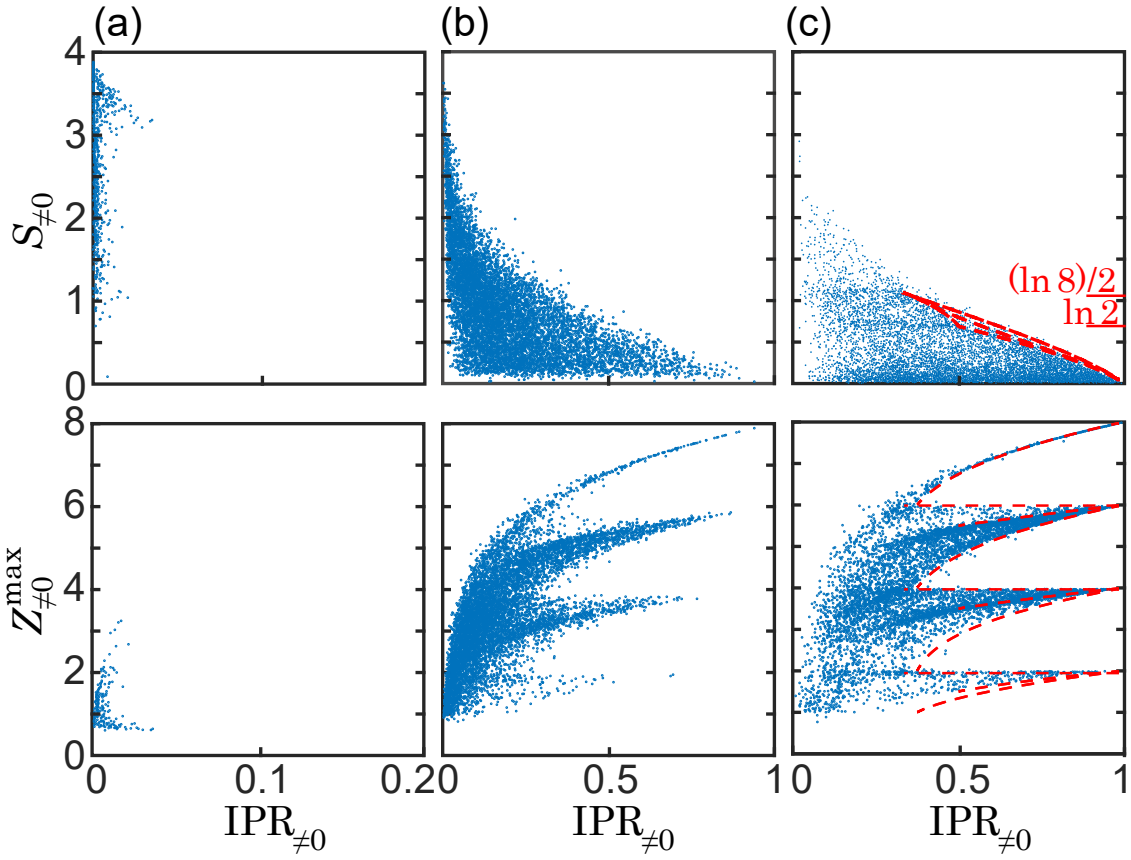

Figure 3.11: Scatter plot of localisation characteristics of nonzero modes in analogy to Fig. 3.10, with the analytical bounds in (c) taken from the bottom panels of Fig. 3.9(a,b).

states, reflecting the full dimensionality of the dimer subspace. For the second resonance case $h_1 = \bar{h} + \delta/2$, $h_2 = -\bar{h} + \delta/2$, the same considerations apply upon interchanging dimer basis states $|s, s'\rangle \leftrightarrow |s, -s'\rangle$.

The characteristic features of these finite-energy hybridisation patterns are shown in the bottom row of Fig. 3.8. hybridisations based on $|\psi_0\rangle_{\text{dimer}}$ still produce the same entropies and inverse participation ratios as for the zero mode, while the largest eigenvalue of the Z correlation matrix now arises from the remainder of the chain, where it counts the number of finite spins, thus giving rise to the straight lines at even integers. For the hybridisations $|\psi_{+,\pm}\rangle_{\text{dimer}}$ of even parity, the entropy is stationary around $\delta = 0$, where $S_k = (\ln 8)/2$ while the inverse participation ratio takes the value $\text{IPR}_k = 3/8$. For the hybridisations $|\psi_{-,\pm,k}\rangle_{\text{dimer}}$ of odd parity, a similar behavior is observed with stationary entropies $S_k = \ln 2$ and inverse participation ratios $\text{IPR}_k = 1/2$. In both these hybridisation patterns, the eigenvalue $Z_k^{\max}$ depends both on the hybridisation strength δ and the number of finite spins in the remainder of the chain. Considering that several

hybridised dimers can occur along the chain, we again interpret the predicted inverse participation ratios and Z correlation eigenvalues as upper bounds and lower bounds, respectively.

3.5.5 Summary and Numerical Verification

Summarising the results from this section, we arrive at the following detailed predictions.

For the zero mode, delocalisation occurs via dimer hybridisation patterns with typical entropies $S_0 \sim \ln 3$ or $S_0 \sim \ln 2$, as already observed numerically in the upper panels of Fig. 3.7. Entropies $S_0 \sim \ln 3$ are further expected to correlate with inverse participation ratios bounded as $\mathrm{IPR}_0 \lesssim 1/3$ and leading Z correlation eigenvalues bounded by $Z_0^{\max} \gtrsim 4/3$, while for entropies $S_0 \sim \ln 2$ we expect $\mathrm{IPR}_0 \lesssim 2$ and $Z_0^{\max} \sim 2$. More generally, these quantities should be correlated as shown in the upper panels of Fig. 3.9. These predictions are verified in Fig. 3.10, where we show scatter plots of the described quantities from 10^4 realisations for chains of length $N = 8$. The expected correlations are already well established for moderate values of disorder $W = 8$.

Furthermore, nonzero modes should predominantly display entropies around $S_k = \ln 2$, which can be achieved by the widest variety of hybridisation patterns, followed by $S_k = (\ln 8)/2$, while $S_k = \ln 3$ should occur relatively less frequently, as indeed observed in the lower panels of Fig. 3.7. The expected correlations with IPR_k and $Z_k^{\max}$ are depicted in the lower panels of Fig. 3.9. These predictions are verified in Fig. 3.11.

Comparing the results in Figs. 3.10 and 3.11, we find that the zero modes and nonzero modes are most clearly discriminated by their distinct correlations between the inverse participation ratio IPR_k and the leading Z-correlation eigenvalue $Z_k^{\max}$.

Having confirmed these key predictions, we return to Fig. 3.8 to observe that the dominant hybridisation patterns of the zero modes are appreciable over a larger range of detunings δ than for the nonzero mode. This verifies that the zero mode hybridises more readily than the nonzero modes, and then exhibits more delocalised Fock-space configurations, which provides the general explanation for the numerical observation of this effect in the previous section.

3.6 Discussion and Conclusions

In summary, in many-body systems zero modes protected by a chiral symmetry can localise, but they do so with distinctively different characteristics than nonzero modes. In particular, the zero modes are more delocalised both in terms of their real-space and Fock-space signatures. We explained these differences by the characteristic symmetry-restricted mechanisms allowing the localised basis states to hybridise. These symmetry constraints can be extended to all disorder strengths by considering the fragmentation of real-space correlations.

We developed and demonstrated these effects for the example of a disordered spin-1 Ising chain. For spin 1/2-chains, the chiral symmetry is already present, but symmetry-protected zero modes do not occur as the Hilbert space dimension is even in both parity sectors. In spin-1/2 chains, the nonzero modes are known to delocalise by a single dominant hybridisation pattern, involving dimers with bipartite entanglement entropy $S_k = \ln 2$ [109]. In contrast, in the spin-1 chain, the delocalisation mechanism of zero modes involves a dominant hybridisation pattern with entropy $S_0 = \ln 3$, while nonzero modes involve a competition of various hybridisation patterns, including such with entropy $S_k = (\ln 8)/2$. Even though the underlying hybridisations differ, these entanglement values are reminiscent to those encountered in the fragmented ground state of the spin-1 system by Affleck, Kennedy, Lieb, and Tasaki (AKLT model) [110], as well as for other spin-1 systems, where such entanglement entropy values can be found between a single spin and the remainder of the system [111, 112]. Furthermore, for the studied system the fragmentation of real-space correlations occurs both with respect to the spin orientation as well as with respect to the even and odd sublattices, where the latter is particularly noteworthy as statistically the system is translationally invariant.

A fundamental tenet for disordered interacting quantum systems is the expectation that many-body states close in energy share the same statistical signatures. The symmetry-protected zero-modes discussed here provide a mechanism to equip individual states with their own characteristic signatures. It would be interesting to explore whether the remarkable differences between zero modes and nonzero modes become further accentuated for larger integer spins, and whether these observations also extend to appropriately designed itinerant fermionic systems.

Chapter 4

Universal Entanglement Behaviour

4.1 Context and Background

We know that generic many-body systems are characterised by conformity to the eigenstate thermalisation hypothesis (ETH), which necessitates that the dynamics of such systems will eventually mimic thermal equilibrium in finite time. In a quantum setting, this means the observation of ergodic dynamics in local observables [13, 14, 113, 114], thus leading to highly entangled eigenstates. This entanglement is typically captured via a measure known as the entanglement entropy, which is known to scale extensively with the volume of a system; hence termed as a *volume-law*. However, conformity to the ETH is not necessarily guaranteed, and there exists a broad class of closed many-body quantum system that indeed violates this hypothesis, and is thus no longer subject to equilibrium dynamics. Amongst these are many-body localised systems [2, 3, 53, 115], which are characterised by a disorder-driven entanglement transition into a localised regime [7, 36, 105, 116], where the entanglement entropy scales subextensively according to an *area-law*. The fate of this transition in the context of open quantum systems is also the subject of intense investigation [117–121].

However, the paradigmatic case of many-body localisation is not the only pathway to area-law entanglement scaling—as we see in a recently-studied type of quantum system that exhibits a so-called *quantum Zeno effect* [122–124]. These systems offer an alternate mechanism towards entanglement transitions by considering a randomly-driven system in which the external environment acts as a quantum detector [38–41]. In this new setting, the unconstrained unitary evolution of the unobserved system leads to a ballistic growth of

entanglement in time [125–127], which eventually settles into a highly-entangled quasistationary state characterised by a volume law. The volume-to-area-law transition in these systems is driven, not by disorder, but by random local measurements—typically of a projective nature—which, when performed with a certain threshold frequency, will initiate an entanglement transition to a quasistationary state characterised by an area law [38–40]. For brevity, we will henceforth refer to these systems as quantum circuit models.

The two aforementioned entanglement transitions are clearly driven by different mechanisms, but they nonetheless share the common trait of a distinct volume-to-area-law transition. Therefore, one could rightfully question whether or not these two mechanisms are in any way analogous to each other. We approach this problem primarily using two measures: the bipartite entanglement entropy, and the tripartite mutual information. In conjunction, these two quantities allow us to map out many qualities of the relevant entanglement dynamics, and allow us to simply compare the similarities and differences of the two entanglement transitions. While there is recent debate over the existence of the many-body localised regime and its supposed transition point, the transition point of the quantum circuit model is—as of yet—uncontested at $p \approx 0.3$ [38]. Perhaps there is a relation between the two that is yet to be explored.

Finally, we provide more theoretical insight into the entanglement behaviour by considering how well these two types of entanglement transitions can be captured by random-matrix models—of which, we have significantly greater knowledge of from an analytical viewpoint. These models attempt to generalise Page's law [101]—a foundational concept in the description of entanglement in ergodic many-body systems—by incorporating a finite entanglement length scale, designed to be analogous to the localisation length in many-body localised systems [2, 3, 12, 53, 100]. We consider two types of random-matrix model in particular: structured and unstructured. The unstructured model is the simpler of the two; but we have wonderful insights into both, stemming from Ref. [1]. In this work, we also consider a generalisation of these random matrix models by considering the singular-value decomposition of the random matrices involved.

By providing detailed comparisons of these different models, we hope to establish some universal features of entanglement transitions in general; with an additional hope that some of the dynamics can be captured by more-understood random-matrix models.

4.2 The Models

4.2.1 The Heisenberg Model

We designate the one-dimensional random-field Heisenberg model as our representative model of many-body localisation, in large part due to both its ubiquity and generality, which is of the form

$$H = \sum_{i=1}^{L} \left(S_i^x S_{i+1}^x + S_i^y S_{i+1}^y + S_i^z S_{i+1}^z \right) - \sum_{i=1}^{L} h_i S_i^z, \tag{4.1}$$

where h represents onsite interactions which are randomly chosen from a uniform distribution, in the range $[-W, W]$, to introduce disorder into the model. We previously defined a more general extension of the Heisenberg model—the $S = 1/2$ XXZ model—in Eq. (2.43); however, we choose the special case of $\Delta = 1$ here as we are no longer investigating adiabatic continuity. We also impose periodic boundary conditions and set $t = 1$ for convenience.

The Heisenberg model is amongst the most paradigmatic when it comes to the exploration of the many-body localisation phase transition, and it is known to exhibit behaviour indicative of the many-body localised phase at disorder values of roughly $W > 3$ [36]. However, this is now somewhat contested with recent doubts about the many-body localisation transition in general (discussed in the introduction).

4.2.2 The Quantum Circuit Model

The quantum circuit setup is composed of a one-dimensional chain of L atomic sites, with a single qubit located at each. The dynamics of the system are governed entirely by a "brick-layer" structure of quantum gates, forming a quantum circuit—hence the eponymous choice of name—and is best explicated via a diagram (see Fig. 4.1). The quantum gates act on pairs of neighbouring qubits which are arranged periodically in temporal space. Each discrete time step of this quantum circuit contains two layers of "bricks", with $L/2$ gates acting on all the odd links in one layer and all the even links in the next. For this reason, any multipartite quantities must be calculated for each of these layers separately and averaged, in order to avoid biases introduced by the odd-even structure. Throughout this work, we will assume periodic boundary conditions.

Turning to Fig. 4.1, we see that each rectangular block represents the action of a ran-

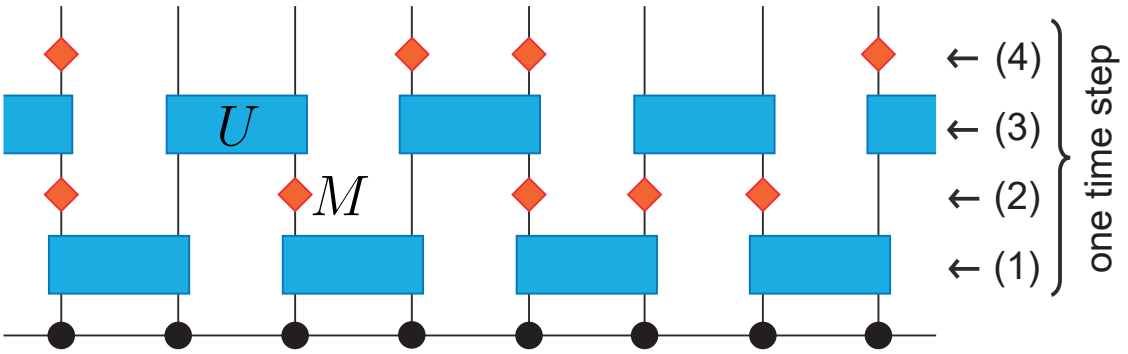

Figure 4.1: A diagrammatic representation of the evolution of a partially-measured quantum circuit over a single time step. The L black dots at the bottom each signify the location of a lone qubit with spin $S = 1/2$. The blue rectangular blocks correspond to unitary two-spin operators U that act on neighbouring pairs of qubits; whereas the orange diamonds correspond to projective measurements M of the form $|\uparrow\rangle\langle\uparrow|$ or $|\downarrow\rangle\langle\downarrow|$. The specific configuration of the measurements is arbitrary and is, in reality, chosen completely randomly—the probability of each individual measurement being denoted as p (and nonmeasurement as $1 - p$).

dom quantum gate on a pair of neighbouring qubits. This is mathematically equivalent to the action of a unitary two-spin operator U acting on each pair of qubits, with each operator being chosen randomly according to the *Haar measure* over the set of unitary two-spin operations. Numerically, this equates to a random matrix of dimension 2^2—each element of which is plucked randomly from the *Gaussian unitary ensemble* (GUE). In addition to this random unitary scrambling, we also subject a set of qubits—randomly chosen at each time step—to projective measurements $M \in [|\uparrow\rangle\langle\uparrow|, |\downarrow\rangle\langle\downarrow|]$ with a probability p. Over time, past a certain threshold probability, these successive projective measurements will drive the system into a quasistationary regime with entanglement that obeys an area law instead of a volume law [38–40]. Work has also been done concerning nonprojective measurements, where each operator M takes the form of a normalised Kraus operator associated with a positive operator-valued measure (POVM) [57, 128–132], and also for stroboscopic and continuous measurements [133]; however, we utilise only the more-standard projective measurements in this work.

4.2.3 The Random-Matrix Models

We adopt a random-matrix model designed to encapsulate the essence of ergodicity, while at the same time incorporating a finite entanglement length scale that mimics the localisation length found in many-body quantum systems. We begin by noting a key assumption of Page's law [101]; namely, that a typical many-body eigenstate $|\psi\rangle$ in the ergodic regime is well-represented by a random Fock-space vector with independently distributed Gaussian elements $\psi_m = \langle m|\psi\rangle$. If we bipartition such a vector as a tensor product $|m\rangle = |ab\rangle$—with indices $a = 1, 2, 3, \ldots, M_A$ for subsystem A, and $b = 1, 2, 3, \ldots, M_B$ for its complement B—then the reduced density matrix $\rho^{A|B}_{aa'}$ of subsystem A can be equivalently formulated as a matrix product

$$\rho^{A|B} = \frac{VV^\dagger}{\operatorname{tr} VV^\dagger}, \tag{4.2}$$

where $V_{ab} = \langle ab|\psi\rangle$ are the elements of a random Gaussian matrix of dimension $M_A \times M_B$[1]. Following through with these arguments allowed Page to arrive at a prediction for the ensemble-averaged bipartite entanglement entropy of the form

$$S(A|B) = -\operatorname{tr}\Big(\rho^{A|B} \ln \rho^{A|B}\Big) = \ln M_A - \frac{M_A}{2M_B}, \tag{4.3}$$

where it is assumed that $1 \ll M_A \leq M_B$ in order to make the result independent of any specific random-matrix-theory universality class.

These observations serve as the framework for the random-matrix-theory models that we will now introduce. We start by noting that the matrix V in Eq. (4.2), in a sense, captures the correlation amplitudes between adjacent subsystems, A and B, in a statistically invariant way; therefore leading to the notion that any independent superposition $V = \sum_{\alpha=1}^{N_\alpha} V^\alpha$ delivers the same statistics—provided that the $\{V^\alpha\}$ are all of the same Gaussian ensemble. Now, we explicate the setup of our system—we consider a system partitioned into a number of smaller ergodic patches $P_1, P_2, P_3, \ldots$ of equal dimension M_0, thus leading to a wavefunction with elements of the form

$$\psi_{abcd\ldots} = \sum_{\alpha=1}^{N_\alpha} V^{1|2,\alpha}_{ab} V^{2|3,\alpha}_{bc} V^{3|4,\alpha}_{cd} \ldots, \tag{4.4}$$

where the random Gaussian matrices $V^{k|k+1,\alpha}$ describe the correlations between neighbouring ergodic patches. We will henceforth refer to Eq. (4.4) as the structured RMT

[1] This formulation is therefore tied to the celebrated Wishart ensemble of random-matrix theory [134]—a central ensemble, at the core of much later work, which concerns positive-semidefinite Hermitian matrices of the form $VV^\dagger$.

model. We can also formulate a model under the assumption that the matrices V are separable, thus producing an unstructured RMT model that is equivalent to a superposition of completely separable states—the elements of which take the form

$$\psi_{abcd\ldots} = \sum_{\alpha=1}^{N_\alpha} \chi_a^{1,\alpha} \chi_b^{2,\alpha} \chi_c^{3,\alpha} \chi_d^{4,\alpha} \ldots, \tag{4.5}$$

where the random vectors $\chi^{k,\alpha}$ are blind to all other patches $n \neq k$. This blindness results in a model completely lacking in geometric features, such as dimensionality and boundary conditions, and thus cannot differentiate between any nonequivalent ordering of patches. Ref. [1] provides excellent details on the specific properties on these two variants of random-matrix model.

In addition to the previously defined structured and unstructured RMT models, we also consider a variant in which the *singular-value decomposition* (SVD) of V is considered. By definition, the SVD of the matrix V is defined as

$$V \equiv L\Lambda R^\dagger = \sum_{n=1}^{\operatorname{rank}(V)} \lambda_n \mathbf{l}_n \mathbf{r}_n^\dagger, \tag{4.6}$$

where Λ is a diagonal matrix with elements corresponding to the singular values λ_n. The final formulation in Eq. (4.6) is sometimes referred to as a "rank-1 decomposition" since each of the $\mathbf{l}_n \mathbf{r}_n^\dagger$ are easily verifiable as being of rank 1—since the columns of the outer product are all proportional to the first column, implying linear dependence on said column—provided that $\mathbf{l}_n$ and $\mathbf{r}_n$ are nonzero. We can therefore suppose a random-matrix model akin to Eq. (4.4), but with $V^{k|k+1,\alpha}$ not picked randomly from a Gaussian ensemble, but instead equal to

$$V^{k|k+1,\alpha} = \sum_{n=1}^{\dim(V^{k|k+1,\alpha})} \lambda_n^{k|k+1,\alpha} \mathbf{l}_n^{k|k+1,\alpha} \left(\mathbf{r}_n^{k|k+1,\alpha}\right)^\dagger, \tag{4.7}$$

where $\mathbf{l}_n^{k|k+1,\alpha}$ and $\mathbf{r}_n^{k|k+1,\alpha}$ are random vectors, and $\lambda_n^{k|k+1,\alpha}$ are values that we set arbitrarily. We will henceforth omit the superfluous superscripts when making general statements—that apply for all values of k and α—for brevity. This SVD-like definition of V allows us to continuously adjust the $\{\lambda_n\}$ between different "ranks" and, in theory, should produce unstructured behaviour when $\lambda_n = \delta_{n1}\ \forall\ n$, while becoming somewhat more structured as the $\{\lambda_n\}$ become more similar to each other, mimicking the full-rank nature of the typical Gaussian matrix. We are therefore primarily interested in the ratios between the various pairs in $\{\lambda_n\}$.

We end by noting that—due to our choice of spin-1/2 particles in both the Heisenberg and quantum circuit models—the dimension of our ergodic patches should be equal to the number of spin-degrees of freedom for the best direct comparisons, which is 2 in this case. This means that the dimension of V and χ, in Eqs. (4.4) and (4.5) respectively, is 2. This also has useful implications for our additional variant expressed in Eq. (4.7), in that there will only be two singular-value-like constants, λ_1 and λ_2, and thus we need only keep track of a single ratio

$$\frac{\lambda_{\min}}{\lambda_{\max}} \equiv \frac{\min(\lambda_1, \lambda_2)}{\max(\lambda_1, \lambda_2)}, \tag{4.8}$$

where all unique properties are definitively encapsulated in the range $\lambda_{\min}/\lambda_{\max} \in [0, 1]$.

4.3 Measures of Entanglement

4.3.1 Tripartite Mutual Information

We previously defined the bipartite entanglement entropy in section 3.4.1; however, let us now discuss generalisations of this entropy, alongside other related quantities; namely, the *tripartite mutual information* (TMI)—a type of so-called *interaction information*—which is defined as

$$\begin{aligned} \mathcal{I}_3(A:B:C) = S(A) + S(B) + S(C) + S(A \cup B \cup C) \\ - S(A \cup B) - S(A \cup C) - S(B \cup C), \end{aligned} \tag{4.9}$$

where each of the four subsystems—A, B, C and D—is defined to be of equal length $L/4$, thus necessitating that the number of particles, or patches, in our system must be a multiple of four. It should also be noted that we use the shorthand notation $S(A) \equiv S(A|B \cup C \cup D)$; in other words, the entropy $S(A)$ is a measure of entanglement between subsystem A and the rest of the system. This shorthand is trivially extended to all other possible bipartitions.

To explicate our notation fully, we can simply relabel the indices of Eq. (3.82) like so

$$|\psi\rangle = \sum_{\alpha\beta\gamma\delta} \psi_{ab} \, |\alpha\beta\rangle \otimes |\gamma\delta\rangle \,, \tag{4.10}$$

where α, β, γ, and δ are labels corresponding to each of the subsystems A, B, C, and D respectively. Note that each of the amplitudes $\{\psi_{ab}\}$ now has $a, b \in \{(x, y)\}$ (where $x, y \in \{\alpha, \beta, \gamma, \delta\}$); thus, we can assign natural-integer values to each ordered pair $(x, y) \in \mathbb{N}$ to allow us to, once again, treat the $\{\psi_{ab}\}$ as indices of some state matrix Ψ. We then

retrieve the Schmidt coefficients λ_α by performing SVD on this matrix Ψ, as detailed in the latter half of section 3.4.1.

Unlike the more well-known bipartite mutual information $S(A:B)$—which is always non-negative—the tripartite mutual information can be either positive or negative. They are both, in essence, a measure of information bound up in a given set of variables—information that is not present in any subset of those variables.

4.3.2 Partition Choice

From the equidimensional subsystems written down in Eq. (4.10), one could rightfully ask the question of how to define such subsystems. We can do so in a number of ways—the most intuitively obvious involving splitting the system into quarters like so

$$A_1 A_2 \dots A_{\frac{L}{4}} B_1 B_2 \dots B_{\frac{L}{4}} C_1 C_2 \dots C_{\frac{L}{4}} D_1 D_2 \dots D_{\frac{L}{4}}, \tag{4.11}$$

where each of $\{X_n\}$ represents an atomic site belonging to subsystem X. We can, however, "scramble" the subsystems such that their bipartite correlations become somewhat more chaotic like so

$$A'_1 B'_1 A'_2 B'_2 \dots A'_{\frac{L}{4}} B'_{\frac{L}{4}} C'_1 D'_1 C'_2 D'_2 \dots C'_{\frac{L}{4}} D'_{\frac{L}{4}}, \tag{4.12}$$

with the maximal scrambling taking the form

$$A''_1 B''_1 C''_1 D''_1 A''_2 B''_2 C''_2 D''_2 \dots A''_{\frac{L}{4}} B''_{\frac{L}{4}} C''_{\frac{L}{4}} D''_{\frac{L}{4}}. \tag{4.13}$$

Note that the more scrambled choices of subsystems are denoted as $\{X'_n\}$ and $\{X''_n\}$ in order to avoid ambiguity. We also employ periodic boundary conditions, thus assuming a ring-like structure of ergodic patches. Choosing different subsystem partitions will inevitably affect the behaviour of the tripartite mutual information, and we explore all three variants in order to ascertain if different subsystem definitions allows for more harmony—or more conflict—between the entanglement behaviour of our four different models.

4.4 Numerical Comparisons

We begin by first establishing the general nature of the TMI-entropy relationship between our four chosen models, which is depicted in Figs. 4.2 and 4.3—in particular, focusing on the RMT models first. We can immediately see quite clearly that the different choice of

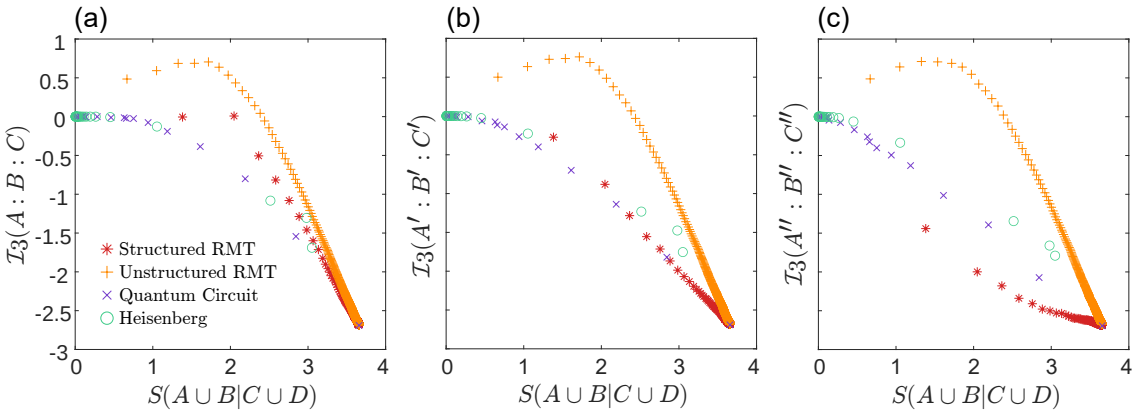

Figure 4.2: Scatter plot of the relationship between the tripartite mutual information $\mathcal{I}_3(A:B:C)$ and the bipartite entanglement entropy $S(A\cup B|C\cup D)$ for the three different partition choices discussed in section 4.3.2—(a) is nonscrambled, (b) is partially scrambled, and (c) is maximally scrambled, denoted by the usage of X, X', and X'' respectively. Data collected from the models defined in sections 4.2.1, 4.2.2, and 4.2.3 across the respective parameter ranges $W\in[0,12]$, $p\in[0,1]$, and $N_\alpha\in[1,\dim(M_{A\cup B})]$. Averaged over 10^3 realisations.

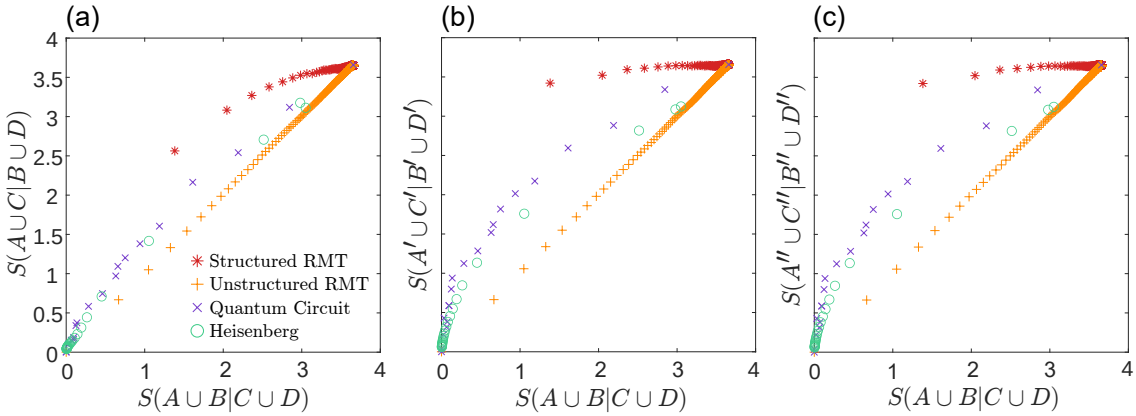

Figure 4.3: Scatter plot of the relationship between the bipartite entanglement entropy $S(A\cup C|B\cup D)$—concerning nonadjacent subsystems—and the bipartite entanglement entropy $S(A\cup B|C\cup D)$ for the three different partition choices discussed in section 4.3.2—(a) is nonscrambled, (b) is partially scrambled, and (c) is maximally scrambled, denoted by the usage of X, X', and X'' respectively. Data collected from the models defined in sections 4.2.1, 4.2.2, and 4.2.3 across the respective parameter ranges $W\in[0,12]$, $p\in[0,1]$, and $N_\alpha\in[1,\dim(M_{A\cup B})]$. Averaged over 10^3 realisations.

partitions in panels (a), (b), and (c) has zero effect on the entropies of the unstructured RMT model. This is as expected since, by definition, Eq. (4.5) makes no reference to the

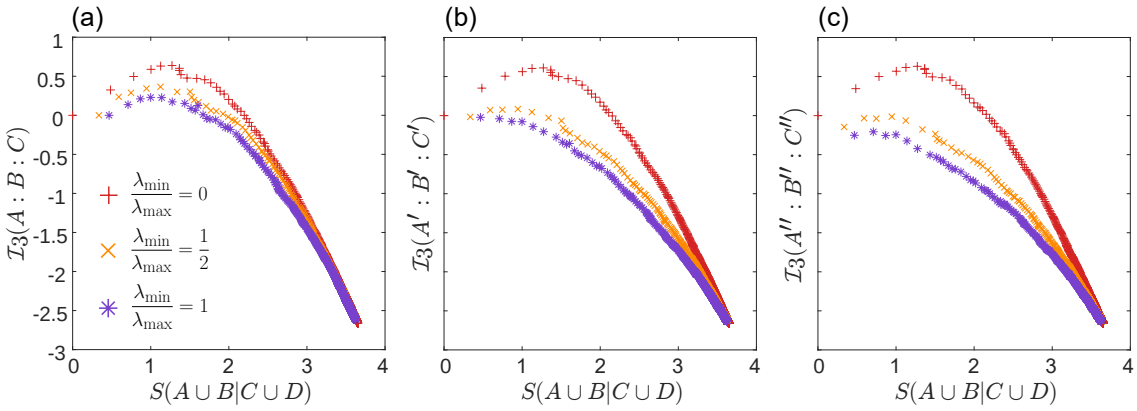

Figure 4.4: Scatter plot of the relationship between the tripartite mutual information $\mathcal{I}_3(A:B:C)$ and the bipartite entanglement entropy $S(A\cup B|C\cup D)$ for the three different partition choices discussed in section 4.3.2—(a) is nonscrambled, (b) is partially scrambled, and (c) is maximally scrambled, denoted by the usage of X, X', and X'' respectively. Data collected from the SVD-like model defined in section 4.2.3 for different representative values of the ratio $\lambda_{\min}/\lambda_{\max}$. Averaged over 10^3 realisations.

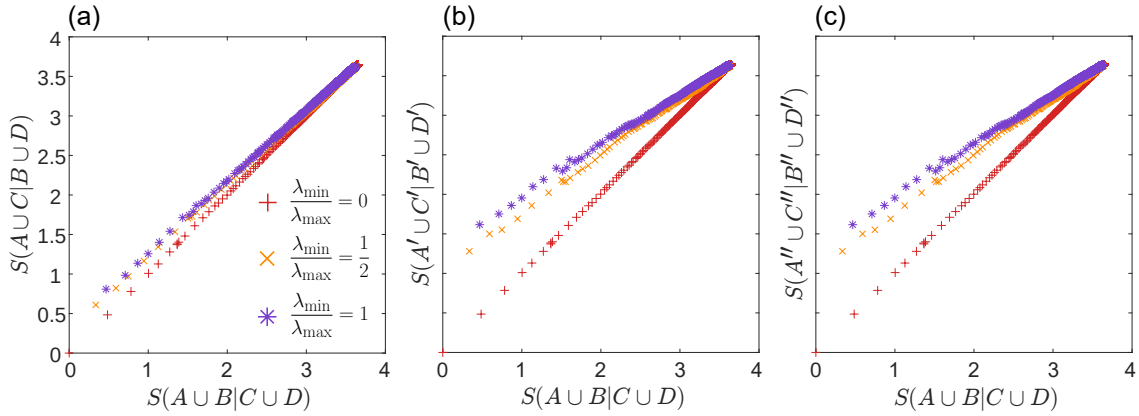

Figure 4.5: Scatter plot of the relationship between the bipartite entanglement entropy $S(A\cup C|B\cup D)$—concerning nonadjacent subsystems—and the bipartite entanglement entropy $S(A\cup B|C\cup D)$ for the three different partition choices discussed in section 4.3.2—(a) is nonscrambled, (b) is partially scrambled, and (c) is maximally scrambled, denoted by the usage of X, X', and X'' respectively. Data collected from the SVD-like model defined in section 4.2.3 for different representative values of the ratio $\lambda_{\min}/\lambda_{\max}$. Averaged over 10^3 realisations.

ordering of our ergodic patches, so any scrambled permutation of patches will produce exactly the same data for any multipartite quantity. The scrambling of ergodic patches, however, has very notable effects on the other three models, with the most extreme dif-

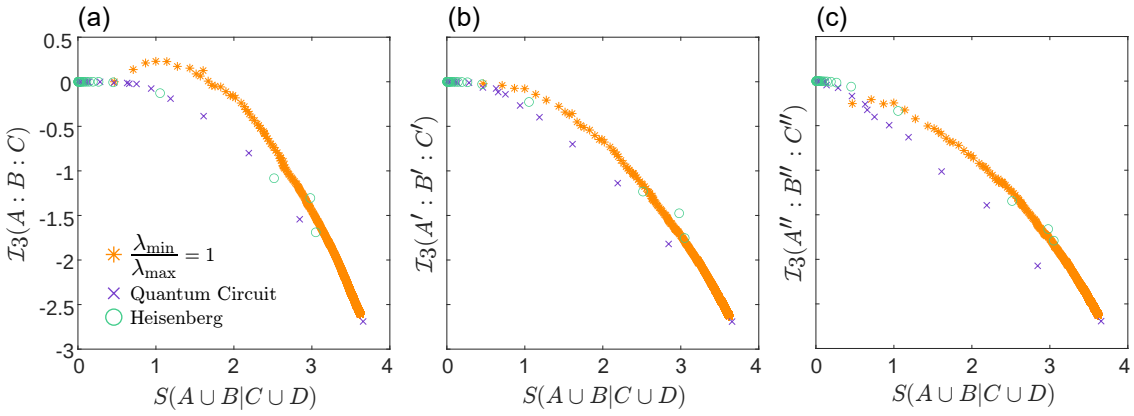

Figure 4.6: Scatter plot of the relationship between the tripartite mutual information $\mathcal{I}_3(A : B : C)$ and the bipartite entanglement entropy $S(A \cup B|C \cup D)$ for the three different partition choices discussed in section 4.3.2—(a) is nonscrambled, (b) is partially scrambled, and (c) is maximally scrambled, denoted by the usage of X, X', and X'' respectively. Data collected from the models defined in sections 4.2.1, 4.2.2, and the SVD-like model defined in section 4.2.3 across the respective parameter ranges $W \in [0, 12]$, $p \in [0, 1]$, and $N_\alpha \in [1, \dim(M_{A\cup B})]$. Averaged over 10^3 realisations.

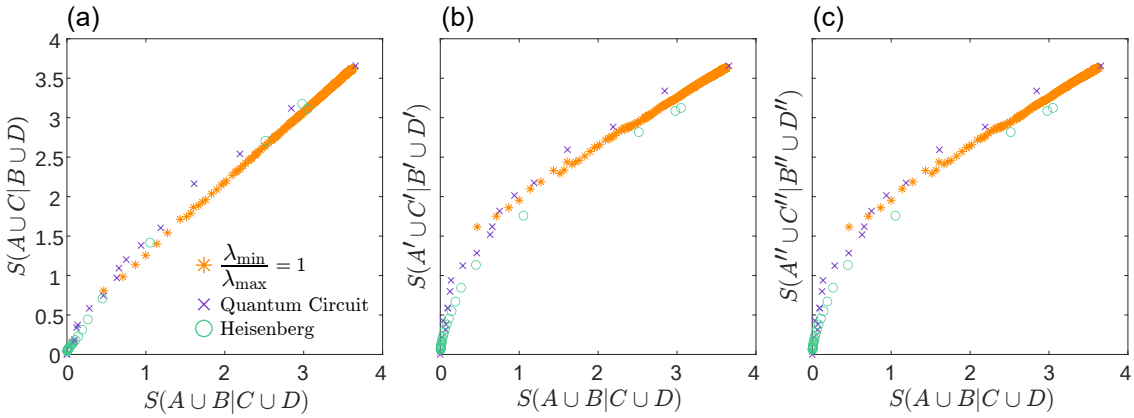

Figure 4.7: Scatter plot of the relationship between the bipartite entanglement entropy $S(A \cup C|B \cup D)$—concerning nonadjacent subsystems—and the bipartite entanglement entropy $S(A \cup B|C \cup D)$ for the three different partition choices discussed in section 4.3.2—(a) is nonscrambled, (b) is partially scrambled, and (c) is maximally scrambled, denoted by the usage of X, X', and X'' respectively. Data collected from the models defined in sections 4.2.1, 4.2.2, and the SVD-like model defined in section 4.2.3 across the respective parameter ranges $W \in [0, 12]$, $p \in [0, 1]$, and $N_\alpha \in [1, \dim(M_{A\cup B})]$. Averaged over 10^3 realisations.

ferences being found in the structured RMT model. This is also somewhat expected, since Eq. (4.4) makes very explicit reference to the ordering of the ergodic patches in the construction of the wavefunction. However, we note that as the number of ergodic product-state-like terms N_α increases, all partition scramblings converge towards the same values of both entropy and TMI. This is very much in keeping with the nature of true ergodicity, as a fully ergodic system would eventually become agnostic to qualities such as patch ordering—in a sense, the patches become indistinguishable from each other. It can also be seen that the TMI of the structured RMT becomes negative—while the entropy $S(A \cup C|B \cup D)$ increases in magnitude—much faster for the more scrambled partitions; it is as if the scrambling of the partitions increases the initial ergodicity.

Additionally, one could also make the observation that panels (b) and (c) in Fig. 4.3 appear to be identical. This is not a trick of the light—the data in these two panels are indeed identical. This can be quite simply explained by considering the way in which we have defined our partitions (4.12) and (4.13). Note the placement of the constituent elements of subsystems, A and C, in the aforementioned equations: they differ only in ordering. If we therefore consider the composite subsystem $A \cup C$, then we quickly realise that $A' \cup C' = A'' \cup C''$. The same is trivially true also for the complement subsystem, in that $B' \cup D' = B'' \cup D''$.

It is now time to turn to the behaviour of the more physical Heisenberg and quantum circuit models in Figs. 4.2 and 4.3. The impact of partition choice on these two models lies somewhere in between that of the two RMT models. They are both mildly affected by the partition scrambling; however, the difference becomes less and less significant as one approaches the respective entanglement transitions in the two models, the three scramblings eventually becoming equivalent deep into the area-law regime. On top of this, we see that the majority of data points for the two physical models densely populate the origin of the plots; whereas, for the two RMT models, we see the majority of data points densely populating the high-entropy regions. From this, we can draw the conclusion that the two RMT models are of little use in capturing the behaviour of nonergodic regimes. In fact, one could question whether or not true ergodicity is well captured at all in the Heisenberg model. If one draws their attention to the high-entropy region of the two physical models, we see that the quantum circuit model has a single data point at $S(A \cup B|C \cup D) \approx 3.7$ that aligns with the maximum entropy exhibited in the two RMT models. However, the

Heisenberg model has no such data point—the highest-entropy data point the Heisenberg model possesses is at $S(A \cup B|C \cup D) \approx 3$. This implies that, even at low finite values of disorder, the Heisenberg model is never truly ergodic—at least, not to the same extent as a typical Gaussian ensemble. Outside the high-entropy region, however, one notes that the Heisenberg and quantum circuit models actually share starkly similar characteristics. It is therefore instructive to ask the question of whether or not we can find a relationship between the two entanglement transitions based solely on the behaviour of entropy-like quantities. Indeed, this could be an enlightening direction were one to extend this work further.

Since we have noted that the structured and unstructured variants of the RMT model fail to capture the characteristics of the two physical models in the area-law regime, let us see if the SVD-like form defined in Eq. (4.7) can do any better. We begin by comparing the different entropy curves for different representative values of $\lambda_{\min}/\lambda_{\max} \in [0, 1]$, defined in Eq. (4.8). These comparisons are depicted in Figs. 4.4 and 4.5. We can immediately see that, as predicted in section 4.2.3, that $\lambda_{\min}/\lambda_{\max} = 0$ is extremely similar to the unstructured RMT curve seen in Figs. 4.2 and 4.3. It even shares the quality of invariance under partition scramblings, as panels (a), (b), and (c) depict near-identical curves for $\lambda_{\min}/\lambda_{\max} = 0$. Also, we do indeed see that the curves take on more-structured behaviour as $\lambda_{\min}/\lambda_{\max} \to 1$; however, they do not become overly similar to the structured RMT curves seen in Figs. 4.2 and 4.3. This is most dramatically seen when comparing Fig. 4.3 to Fig. 4.5—the former depicts a distinctly curved scatter, whereas the latter maintains the form of a straight line. However, this difference does allow for the possibility of better agreement when compared to the curves of the two physical models, to which we now turn.

Figs. 4.6 and 4.7 show direct comparisons between the two, more physical, Heisenberg and quantum circuit models and the SVD-like RMT model with $\lambda_{\min}/\lambda_{\max} = 1$. While the SVD-like RMT model still struggles to capture behaviour deep in the area-law regime—especially in Fig. 4.7—it does a much better job of approximating the lower-entropy regions, and even offers improvement in the higher-entropy regions too. Overall, the shape of the curves seem to match well, despite the apparent limitations, and could perhaps be used to understand the transition region in terms of random matrix theory with further study.

4.5 Discussion of Initial Results

The main results of this initial foray into comparing the different types of entanglement transition can be summarised as follows. The Heisenberg and quantum circuit models share stunningly similar behaviour when we study the relationship between the well-known bipartite entanglement entropy and the lesser-known tripartite mutual information. Further work could illuminate areas of the debate concerning the recent uncertainty of the transition location in many-body localised systems [44, 45]—namely, in theory, one could attempt to map the entropy from the Heisenberg model (as a function of disorder strength W) to the entropy of the quantum circuit model (as a function of measurement probability p). Since the location of the quantum circuit model's entanglement transition has yet to be hotly debated, such a mapping would allow one to potentially estimate the localisation transition in the Heisenberg model. However, it does not resolve arguments concerning the nature of the transition itself, and whether or not many-body localisation is a "true" quantum phase.

Additionally, we have some promising results that random-matrix models could prove to be a valuable diagnostic tool for obtaining a deeper understanding of the mechanisms involved in entanglement transitions. While they struggle with approximations of physical models deep in area-law regimes, they provide much better approximations in higher-entropy regions i.e. volume-law regimes. In particular, a certain type of random-matrix model—based on the structure of the rank-1 decomposition of a matrix—seems to better approximate the behaviour of entropy-like quantities than the more simple structured and unstructured variants. Despite much further work being required, comparison to random-matrix models highlights an interesting feature of the Heisenberg model; namely, that—unlike the quantum circuit model, which does seem to be truly ergodic for measurement probability $p = 0$—it does not appear to be fully ergodic, even for a low disorder strength of $W = 1$. This implies that there is some structure to the Heisenberg model, even in its so-called ergodic regime.

Hopefully, these interesting initial results can be extended further to provide us with more insight into the rapidly-blossoming study of entanglement transitions—in both many-body localised systems, "brick-layer" quantum circuit systems, and beyond.

Epilogue

The world-changing potential of nanotechnology cannot be understated; it radically shifts the paradigms of many problems that plague us today, ranging from the biological all the way to the industrial. In particular, the stunning concept of quantum computation falls under the vast umbrella of nanotechnology, and is very relevant to the systems we have explored in this work—systems that possess robust emergent integrability and memory of initial conditions, both of which are invaluable in the pursuit of quantum computation. The pursuit of reliable quantum computers is, in many ways, a deeply ironic endeavour—the very quantum phenomena we throw vast computational power at today, in order to glean shreds of insight into the quantum world, would be easily solved by a quantum computer. Not only does God throw dice where we cannot see them, he also writes a map to their location on the dice themselves.

The first few chapters of this work focus primarily on explicating some of the mysterious phenomena produced by many-body localised systems. The first chapter provides a brief theoretical background before leading into the second chapter, which attacks a very clearly formulated question: can emergent conserved quantities, central to many-body localisation, truly be constructed via perturbative methods? By constructing the Brueckner orbitals for the eigenstates of the spinless fermion model—a paradigmatic model of many-body localisation—we show that such eigenstates cannot necessarily be constructed from a single basis of single-particle orbitals. This directly implies that at least some of the conserved quantities are of a many-body-like nature, and are thus fundamentally nonperturbative. This finding holds true even for states that have unity-approaching overlap with a single Slater determinant, which we numerically confirm are common in the many-body localised regime. This is invaluable knowledge concerning further study into the explicit construction of single-quasiparticle bases for integrable systems.

The third chapter tackles a different aspect of many-body localisation; namely, the effect of global symmetries—in this case, chiral symmetry—on the nature of many-body

localised eigenstates. We study this in the context of the spin-1 transverse-field Ising model, as the chiral symmetry operators in this model are easily explicated in closed form due to their simple alternating structure. The reason for our choice of spin-1 particles arises from the realisation that the joint constraints of chiral symmetry and an odd-dimensioned Hilbert space necessarily produce a zero mode that is robust to all parameter variation. We find that this model indeed localises—albeit at very large disorder strengths of $W \sim 20$—which is a seminal finding in this field. Also, inspired by the one-particle density matrices used in fermionic models, we formulate a spin-1 analogue that captures distinct fragmented correlations in the zero mode. These correlations indicate that the zero mode—while it clearly localises to some degree, in that its entropy obeys area-law scaling—is significantly less localised than typical nonzero modes. We capture this behaviour numerically, and provide an astoundingly accurate analytical explanation using quasiperturbation theory.

Finally, the fourth chapter considers the nature of entanglement transitions in general, pondering the potential relationship between different models that exhibit transitions into an area-law regime. We choose the Heisenberg model as our representative model of many-body localisation, and compare this to a model of intense recent interest—the "brick-layer" quantum circuit model with random measurements. We also make use of three variants of random-matrix model, with which we try to capture the key characteristics of the aforementioned more-physical models. In order to compare these models, we look at the commonly-utilised bipartite entanglement entropy, along with the tripartite mutual information. By producing scatter plots of these two quantities for the various different models—across various parameter ranges—we find good agreement between the Heisenberg and quantum circuit models in many ways. We also manage to, partially successfully, approximate these two models using a novel formulation of one of the random-matrix models. A key difference to note is that the Heisenberg model is never truly ergodic (to the same extent as the random-matrix models), even at low disorder; whereas the quantum circuit model very clearly is. This preliminary research offers hope for reconciliation between two different types of entanglement transition, and suggests that random-matrix theory could be useful in this context.

In the final analysis, this work constitutes a substantial advancement in our understanding of low-dimensional disordered quantum systems; particularly in the context of emergent conserved quantities, robust zero modes, and random-matrix theory. The emer-

gence of spontaneous order out of disorder is a fascinating concept, and miraculously reflects the words of Carl Jung—"In all chaos there is a cosmos, in all disorder a secret order." Despite his lack of physical background, I can think of no words that summarise many-body localisation better than these, and it is our hope that this research will help shine a light on the rich, hidden cosmos within disordered quantum systems.

Appendix A

Orbital Structure

A.1 The Slater Determinant

It is well known that a given fermionic wavefunction must be antisymmetric, and thus it should obey the *Pauli exclusion principle*, which states that two fermions cannot occupy the same quantum state. To phrase this more mathematically, it is to say that any given fermionic wavefunction must be subject to

$$\psi(\ldots, x_i, \ldots, x_j, \ldots) = -\psi(\ldots, x_j, \ldots, x_i, \ldots), \tag{A.1}$$

which directly leads to the original statement of the Pauli exclusion principle:

$$|\psi(\ldots, x_i, \ldots, x_i, \ldots)|^2 = 0. \tag{A.2}$$

In the two-fermion case where $N = 2$, the construction of an antisymmetric wavefunction is somewhat trivial, and will take the form:

$$\psi(x_1, x_2) = \chi_1(x_1)\chi_2(x_2) - \chi_1(x_2)\chi_2(x_1), \tag{A.3}$$

where the $\{\chi_i(x_j)\}$ are obtained from the relevant single-particle orbitals. It is easy enough to see that this wavefunction obeys the antisymmetry condition; however, a natural question arises at this point: can the construction of an antisymmetric wavefunction be generalised to the N-fermion case? It turns out that this concept is indeed generalisable to an arbitrary number of fermions, and the process by which this is done is known as the *Slater determinant*.

Using the previously defined self-consistent ordering $x_1 < x_2 < \ldots < x_N$, we can define

the Slater determinant as

$$S(x_1, x_2, \ldots, x_N) = \frac{1}{\sqrt{N!}} \begin{vmatrix} \chi_1(x_1) & \chi_2(x_1) & \ldots & \chi_N(x_1) \\ \chi_1(x_2) & \chi_2(x_2) & \ldots & \chi_N(x_2) \\ \vdots & \vdots & \ddots & \vdots \\ \chi_1(x_N) & \chi_2(x_N) & \ldots & \chi_N(x_N) \end{vmatrix} \equiv |\chi_1, \chi_2, \ldots, \chi_N\rangle \,, \tag{A.4}$$

where $\chi_i(x_j)$ represents the amplitude of the ith orbital evaluated at site j, and $\boldsymbol{\chi}_i$ is defined as the ith fermion orbital subject to $\boldsymbol{\chi}_n^\dagger \boldsymbol{\chi}_m = \delta_{nm}$. Due to the properties of the matrix determinant, if any two rows are identical within the matrix of orbitals, then the determinant is automatically equal to zero, which is in accordance with the antisymmetry condition conveyed by Eq. (A.1). The explicit determinant in Eq. (A.4) is a useful tool for the numerical construction of an antisymmetrised wavefunction; however, using the ordering of states we established previously, it can also be written as a sum of product states

$$S(x_1, x_2, \ldots, x_N) = \frac{1}{\sqrt{N!}} \sum_{x_1 < x_2 < \ldots < x_N} \chi_1(x_1)\chi_2(x_2)\ldots\chi_N(x_N) \equiv q_{x_1}^\dagger q_{x_2}^\dagger \ldots q_{x_N}^\dagger \, |\text{vac}\rangle \,. \tag{A.5}$$

Therefore, if a given eigenstate can be written as a product state of single-particle operators, then it can be expressed as an exact Slater determinant. In the case of a noninteracting system, each many-body eigenstate will be an exact Slater determinant built from some set of single-particle orbitals via Eq. (A.4). As interactions are introduced, these single-particle orbitals may change, and the many-body eigenstates will likely depart from exact Slater determinants.

A.2 The Iterative Algorithm

Brueckner orbitals are the name given to a set of N single-particle orbitals, each with dimension L, which maximise the overlap between a Slater determinant constructed from these orbitals (optimal Slater determinant), and a given many-body eigenstate of our system. To phrase this more mathematically, the Brueckner orbitals maximise the quantity $\mathcal{I}_n \equiv |\langle \psi_n | S_n \rangle|^2$. Therefore, the construction of Brueckner orbitals for our model will allow us to quantify the answer to the first key question in section 2.2 more convincingly.

while it may be possible to utilise analytical methods to construct these orbitals for

smaller systems with fewer fermions, this becomes an impossibly difficult task for even slightly larger systems (such as $L = 8$, $N = 4$). There is more than one way to construct these orbitals numerically; however, we should turn our attention to methods for which the overlap increases monotonously with the number of iterations in order to be sure that the Brueckner orbitals are at least close to optimal. One possible way of doing this involves the optimisation of one single-particle orbital at a time, thus ensuring monotonous improvement of the overlap as the number of iterations is increased[1].

A detailed review of a generalised process for constructing M orbitals, which maximise the overlap $\mathcal{I}_n$, can be found in Ref. [71]; however, since we are dealing with the special case of $M = N$, the method simplifies greatly. We begin by first defining the overlap explicitly in terms of the orbital ϕ_1, which is to be optimised, which can be written as

$$\begin{aligned}\mathcal{I}_n &\equiv |\langle\psi_n|S_n\rangle|^2 \\ &= \left|\sqrt{N!}\sum_{x_1<x_2<\ldots<x_N}\psi^*(x_1,x_2,\ldots,x_N)\phi_1(x_1)\phi_2(x_2)\ldots\phi_N(x_N)\right|^2 \\ &= |\langle g|\phi_1\rangle|^2,\end{aligned} \tag{A.6}$$

where the single-particle function is defined as

$$\begin{aligned}g(X) \equiv \sqrt{N!}\sum_{x_1<x_2<\ldots<x_N}&\psi(x_1,x_2,\ldots,x_N) \\ &\times\phi_2^*(x_2)\phi_3^*(x_3)\ldots\phi_N^*(x_N).\end{aligned} \tag{A.7}$$

Previously, we argued that if any two rows (or columns) in the Slater determinant are identical, then it will be zero due to the properties of the matrix determinant, which is in accordance with the Pauli exclusion principle. In addition to this, $\psi(x_1,x_2,\ldots,x_N)$ is assuredly antisymmetric due to the form of the Hamiltonian (2.44). Due to these properties, it can be seen that if $\phi_1 \to \phi_{1<i\leq N}$, then this will result in $\langle g|\phi_{1<i\leq N}\rangle = 0$, and thus $|g\rangle$ is orthogonal to $|\phi_{1<i\leq N}\rangle$ by definition[2]. Therefore, the optimal ϕ_1, with respect to $\{\phi_{1<i\leq N}\}$, is simply proportional to the g which maximises $\mathcal{I}_n = |\langle g|\phi_1\rangle|^2$. It is important to note that ϕ_1 being optimal with respect to $\{\phi_{1<i\leq N}\}$ does not ensure that the other orbitals are optimal with respect to each other; however, a cyclic shift of $\phi_i \to \phi_{(i\mathrm{mod}L)+1}$, can be performed after each iteration before optimising again. This process can be repeated an arbitrary number of times to increase $\mathcal{I}_n$ to its maximal value; however, we expect

[1] See Ref. [70] for a detailed review of a similar method which optimises the full set of Brueckner orbitals simultaneously. This is a perfectly valid algorithm, but the overlap will not increase monotonously.

[2] $\phi_{1<i\leq N}$ is simply shorthand for an element of the set $\{\phi_{1<i\leq N}\} \equiv \{\phi_i | i \in \mathbb{Z}, 1 < i \leq N\}$.

states in the localised phase to be well approximated by Slater determinants (indicated by previous data), so this process should converge to the maximum $\mathcal{I}_n$ very quickly.

To perform this iterative process, the program must first be initialised with a matrix composed of an orthogonal set of N orbitals. In order to initialise the process with an unbiased initial matrix, we can fill an $L \times L$ matrix A with arbitrary values plucked from some random distribution (either gaussian or uniform). This matrix can then be decomposed via the QR-decomposition[3] as $A = QR$, where Q is an orthogonal matrix, and R is an upper-triangular matrix. The orthogonal matrix Q is then used as the initial set of N orthogonal orbitals, and will take the form:

$$\begin{aligned} Q &= \begin{bmatrix} \phi_1(1) & \phi_2(1) & \dots & \phi_N(1) \\ \phi_1(2) & \phi_2(2) & \dots & \phi_N(2) \\ \vdots & \vdots & \ddots & \vdots \\ \phi_1(L) & \phi_2(L) & \dots & \phi_N(L) \end{bmatrix} \\ &\equiv [\boldsymbol{\phi}_1, \boldsymbol{\phi}_2, \dots, \boldsymbol{\phi}_N] \,. \end{aligned} \tag{A.8}$$

The primary problem with numerically evaluating $g(X)$ is the distribution of minus signs; however, this can be handled via the use of a determinant [71], and this will take the form:

$$\begin{aligned} g(X) \equiv & \sqrt{N!} \sum_{x_1 < x_2 < \ldots < x_N} \psi(x_1, x_2, \dots, x_N) \\ & \times \sum_{m=1}^{N} (-1)^{m-1} \delta_{x,x_m} \det{}^* \{Y_m\} \,, \end{aligned} \tag{A.9}$$

where $Y_m \in \mathbb{C}^{(N-1)\times(N-1)}$ is formed by taking the rows from $Q \in \mathbb{C}^{L\times N}$ corresponding to $\{x_1, x_2, \dots, x_N\}$ excluding the x_mth row. By using this iterative algorithm, a full set of Brueckner orbitals can be generated for each many-body eigenstate. These Brueckner orbitals will be the best possible approximation of a given many-body eigenstate as an exact Slater determinant, thus allowing us to quantify the exact relationship between the purity of a state and its closeness to a Slater determinant.

[3] See the documentation for "numpy.linalg.qr(...)" in Python 3.x for details on this.

Appendix B

Chiral Symmetry

B.1 Level statistics

The results in this work firmly indicate that all states in the spin-1 Ising chain (3.1) become many-body localised when the disorder becomes sufficiently strong, irrespective of whether they are zero modes or nonzero modes (see, e.g., Fig. 3.5). As this specific model has not been considered before, we here provide further supporting evidence based on the statistics of the standard level-spacing ratio r_k, defined as [5, 6, 36]

$$r_k = \min\left(\frac{E_{k+1}-E_k}{E_k-E_{k-1}}, \frac{E_k-E_{k-1}}{E_{k+1}-E_k}\right), \tag{B.1}$$

where the energies E_k are ordered by magnitude. In an ergodic system, the averaged ratio is expected to be large due to level repulsion, with $\overline{r_k} \approx 0.5307(1)$ if modelled via the Gaussian orthogonal ensemble, while in a many-body localised system it is expected to drop to a smaller value, approaching $\overline{r_k} = 2\ln 2 - 1 \approx 0.38629$ corresponding to Poissonian level statistics [135].

We restrict our attention to the parity sector including the zero mode. Given the chiral symmetry, we arrange the indices k so that $E_0 = 0$ denotes the zero mode and $E_k = -E_{-k}$ denotes the levels paired by the spectral symmetry. Due to this pairing, $r_0 \equiv 1$ in each realisation, so we instead resort to r_1 to characterise the zero mode (which is involved via the spacing $E_1 - E_0$). We contrast this with the statistics of r_k with $k \geq 1$ for the nonzero modes, which we constrain to the middle 10% of the spectrum (note that the chiral symmetry furthermore implies $r_k = r_{-k}$).

In Fig. B.1, the disorder-averaged spacing ratios are shown as a function of disorder

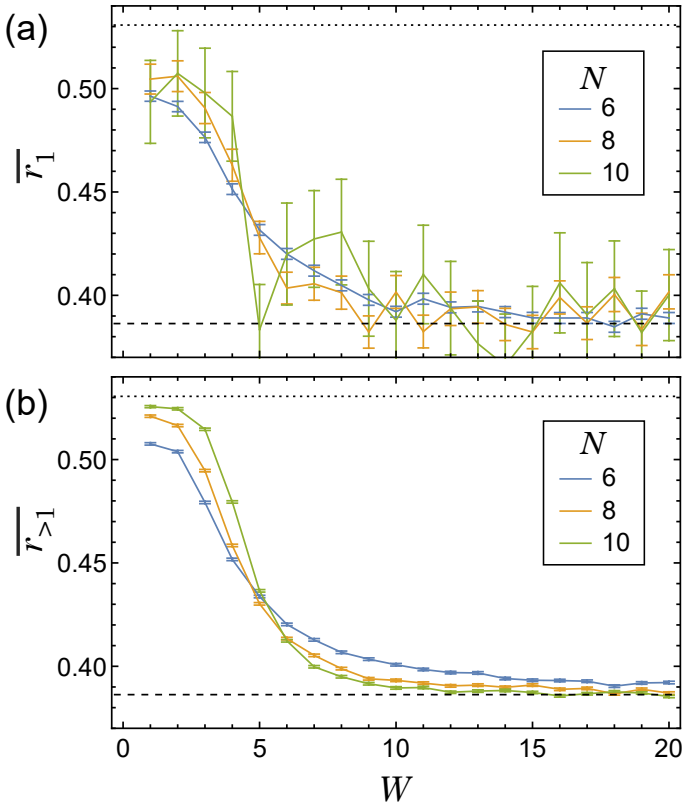

Figure B.1: Disorder-averaged level-spacing ratio (B.1) as a function of disorder strength W, for (a) r_1 (including the spacing of the zero mode to its next neighbour) and (b) r_k with $k > 1$ (only involving spacing between nonzero modes, which are furthermore restricted to the middle 10% of the spectrum). The dotted line indicates the value expected for an ergodic system modelled by the Gaussian orthogonal ensemble of random matrix theory, while the dashed line indicates the value for a localised system with Poissonian level statistics. For the three system sizes $N = 6, 8, 10$, the data shown is obtained from $\sim 10^4, 10^3, 10^2$ realisations, respectively.

strength for three system sizes $N = 6, 8, 10$. The statistical fluctuations for r_1 are large as only a single value is obtained for each realisation. Nonetheless, both figures consistently point towards states becoming localised at about the same strength of disorder, with the averaged ratios of different system size crossing near a point of inflection at around $W \simeq 5$.

In Fig. B.2, we show the full statistical distribution of the spacing ratios for the smallest system size $N = 6$, where enough data can be collected, for representative values of the disorder strength $W = 1, 5, 20$. The results for r_1 and $r_{>1}$ resemble each other closely in all three cases, being consistent with ergodic behavior for $W = 1$ as well as many-body localised behavior for $W = 20$, and displaying similar intermediate statistics for $W = 5$.

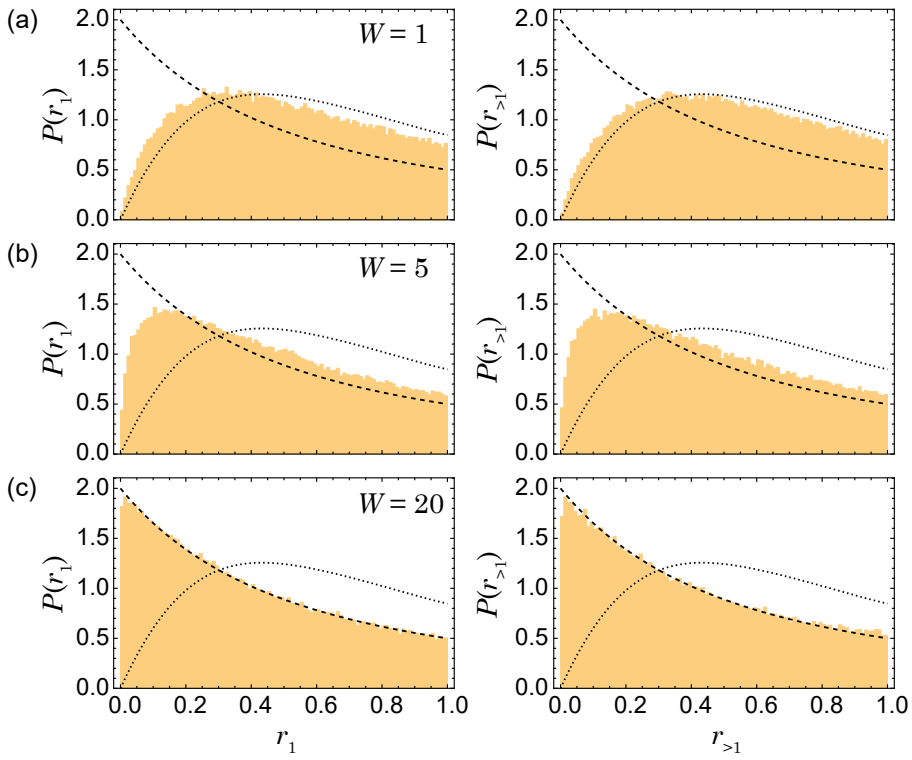

Figure B.2: Distribution of level-spacing ratios corresponding to Fig. B.1, with the system size fixed at $N = 6$ and the disorder strength set to (a) $W = 1$, (b) $W = 5$, and (c) $W = 20$, using 2×10^5 realisations. The curves indicate the expected distribution for an ergodic system modelled by the Gaussian orthogonal ensemble of random matrix theory (dotted), as well as a localised system with Poissonian level statistics (dashed).

Bibliography

[1] Marcin Szyniszewski and Henning Schomerus. Random-matrix perspective on many-body entanglement with a finite localization length. *Physical Review Research*, 2(3):032010, 2020.

[2] Rahul Nandkishore and David A Huse. Many-body localization and thermalization in quantum statistical mechanics. *Annu. Rev. Condens. Matter Phys.*, 6(1):15–38, 2015.

[3] Ehud Altman and Ronen Vosk. Universal dynamics and renormalization in many-body-localized systems. *Annu. Rev. Condens. Matter Phys.*, 6(1):383–409, 2015.

[4] Dmitry A Abanin, Ehud Altman, Immanuel Bloch, and Maksym Serbyn. Colloquium: Many-body localization, thermalization, and entanglement. *Reviews of Modern Physics*, 91(2):021001, 2019.

[5] Arijeet Pal and David A Huse. Many-body localization phase transition. *Physical review b*, 82(17):174411, 2010.

[6] Vadim Oganesyan and David A Huse. Localization of interacting fermions at high temperature. *Physical review b*, 75(15):155111, 2007.

[7] Marko Žnidarič, Tomaž Prosen, and Peter Prelovšek. Many-body localization in the heisenberg x x z magnet in a random field. *Physical Review B*, 77(6):064426, 2008.

[8] Philip W Anderson. Absence of diffusion in certain random lattices. *Physical review*, 109(5):1492, 1958.

[9] Jan Šuntajs, Janez Bonča, Tomaž Prosen, and Lev Vidmar. Quantum chaos challenges many-body localization. *Physical Review E*, 102(6):062144, 2020.

[10] Maksym Serbyn and Joel E Moore. Spectral statistics across the many-body localization transition. *Physical Review B*, 93(4):041424, 2016.

[11] Corentin L Bertrand and Antonio M García-García. Anomalous thouless energy and critical statistics on the metallic side of the many-body localization transition. *Physical Review B*, 94(14):144201, 2016.

[12] Fabien Alet and Nicolas Laflorencie. Many-body localization: An introduction and selected topics. *Comptes Rendus Physique*, 19(6):498–525, 2018.

[13] Josh M Deutsch. Quantum statistical mechanics in a closed system. *Physical review a*, 43(4):2046, 1991.

[14] Mark Srednicki. Chaos and quantum thermalization. *Physical review e*, 50(2):888, 1994.

[15] David A Huse, Rahul Nandkishore, and Vadim Oganesyan. Phenomenology of fully many-body-localized systems. *Physical Review B*, 90(17):174202, 2014.

[16] Maksym Serbyn, Zlatko Papić, and Dmitry A Abanin. Local conservation laws and the structure of the many-body localized states. *Physical review letters*, 111(12):127201, 2013.

[17] Valentina Ros, Markus Müller, and Antonello Scardicchio. Integrals of motion in the many-body localized phase. *Nuclear Physics B*, 891:420–465, 2015.

[18] John Z Imbrie. On many-body localization for quantum spin chains. *Journal of Statistical Physics*, 163(5):998–1048, 2016.

[19] John Z Imbrie. Diagonalization and many-body localization for a disordered quantum spin chain. *Physical review letters*, 117(2):027201, 2016.

[20] John Z Imbrie, Valentina Ros, and Antonello Scardicchio. Local integrals of motion in many-body localized systems. *Annalen der Physik*, 529(7):1600278, 2017.

[21] Louk Rademaker, Miguel Ortuno, and Andres M Somoza. Many-body localization from the perspective of integrals of motion. *Annalen der Physik*, 529(7):1600322, 2017.

[22] KA Brueckner and CA Levinson. Approximate reduction of the many-body problem for strongly interacting particles to a problem of self-consistent fields. *Physical Review*, 97(5):1344, 1955.

[23] KA Brueckner and W Wada. Nuclear saturation and two-body forces: Self-consistent solutions and the effects of the exclusion principle. *Physical Review*, 103(4):1008, 1956.

[24] RK Nesbet. Brueckner's theory and the method of superposition of configurations. *Physical Review*, 109(5):1632, 1958.

[25] Soumya Bera, Henning Schomerus, Fabian Heidrich-Meisner, and Jens H Bardarson. Many-body localization characterized from a one-particle perspective. *Physical review letters*, 115(4):046603, 2015.

[26] Soumya Bera, Thomas Martynec, Henning Schomerus, Fabian Heidrich-Meisner, and Jens H Bardarson. One-particle density matrix characterization of many-body localization. *Annalen der Physik*, 529(7):1600356, 2017.

[27] Benjamin Villalonga, Xiongjie Yu, David J Luitz, and Bryan K Clark. Exploring one-particle orbitals in large many-body localized systems. *Physical Review B*, 97(10):104406, 2018.

[28] Sheng-Hsuan Lin, Björn Sbierski, Florian Dorfner, Christoph Karrasch, and Fabian Heidrich-Meisner. Many-body localization of spinless fermions with attractive interactions in one dimension. *SciPost Physics*, 4(1):002, 2018.

[29] Wouter Buijsman, Vladimir Gritsev, and Vadim Cheianov. Many-body localization in the fock space of natural orbitals. *SciPost Physics*, 4(6):038, 2018.

[30] Nicolas Macé, Nicolas Laflorencie, and Fabien Alet. Many-body localization in a quasiperiodic fibonacci chain. *SciPost Physics*, 6(4):050, 2019.

[31] Christian P Chen, Marcin Szyniszewski, and Henning Schomerus. Many-body localization of zero modes. *Physical Review Research*, 2(2):023118, 2020.

[32] Takahiro Orito, Yoshihito Kuno, and Ikuo Ichinose. Effects of power-law correlated disorders in xxz spin chain: Many-body localized to thermal phase transition and its critical regime. *arXiv preprint arXiv:2002.12575*, 2020.

[33] Miroslav Hopjan and Fabian Heidrich-Meisner. Many-body localization from a one-particle perspective in the disordered one-dimensional bose-hubbard model. *Physical Review A*, 101(6):063617, 2020.

[34] Talía LM Lezama, Soumya Bera, Henning Schomerus, Fabian Heidrich-Meisner, and Jens H Bardarson. One-particle density matrix occupation spectrum of many-body localized states after a global quench. *Physical Review B*, 96(6):060202, 2017.

[35] Miroslav Hopjan, Fabian Heidrich-Meisner, and Vincenzo Alba. Scaling properties of a spatial one-particle density-matrix entropy in many-body localized systems. *Physical Review B*, 104(3):035129, 2021.

[36] David J Luitz, Nicolas Laflorencie, and Fabien Alet. Many-body localization edge in the random-field heisenberg chain. *Physical Review B*, 91(8):081103, 2015.

[37] Andrea De Luca and Antonello Scardicchio. Ergodicity breaking in a model showing many-body localization. *EPL (Europhysics Letters)*, 101(3):37003, 2013.

[38] Yaodong Li, Xiao Chen, and Matthew PA Fisher. Quantum zeno effect and the many-body entanglement transition. *Physical Review B*, 98(20):205136, 2018.

[39] Amos Chan, Rahul M Nandkishore, Michael Pretko, and Graeme Smith. Unitary-projective entanglement dynamics. *Physical Review B*, 99(22):224307, 2019.

[40] Brian Skinner, Jonathan Ruhman, and Adam Nahum. Measurement-induced phase transitions in the dynamics of entanglement. *Physical Review X*, 9(3):031009, 2019.

[41] Yaodong Li, Xiao Chen, and Matthew PA Fisher. Measurement-driven entanglement transition in hybrid quantum circuits. *Physical Review B*, 100(13):134306, 2019.

[42] DA Abanin, Jens H Bardarson, G De Tomasi, S Gopalakrishnan, V Khemani, SA Parameswaran, F Pollmann, AC Potter, Maksym Serbyn, and R Vasseur. Distinguishing localization from chaos: Challenges in finite-size systems. *Annals of Physics*, 427:168415, 2021.

[43] Andrew C Potter, Romain Vasseur, and SA Parameswaran. Universal properties of many-body delocalization transitions. *Physical Review X*, 5(3):031033, 2015.

[44] Alan Morningstar, Luis Colmenarez, Vedika Khemani, David J Luitz, and David A Huse. Avalanches and many-body resonances in many-body localized systems. *arXiv preprint arXiv:2107.05642*, 2021.

[45] Philipp T Dumitrescu, Anna Goremykina, Siddharth A Parameswaran, Maksym Serbyn, and Romain Vasseur. Kosterlitz-thouless scaling at many-body localization phase transitions. *Physical Review B*, 99(9):094205, 2019.

[46] Linda E Reichl. A modern course in statistical physics, 1999.

[47] Marcos Rigol and Mark Srednicki. Alternatives to eigenstate thermalization. *Physical review letters*, 108(11):110601, 2012.

[48] Marcos Rigol, Vanja Dunjko, and Maxim Olshanii. Thermalization and its mechanism for generic isolated quantum systems. *Nature*, 452(7189):854–858, 2008.

[49] Mark Srednicki. The approach to thermal equilibrium in quantized chaotic systems. *Journal of Physics A: Mathematical and General*, 32(7):1163, 1999.

[50] Ferdinand Evers and Alexander D Mirlin. Anderson transitions. *Reviews of Modern Physics*, 80(4):1355, 2008.

[51] Alan J Bray and Michael A Moore. Chaotic nature of the spin-glass phase. *Physical review letters*, 58(1):57, 1987.

[52] Maksym Serbyn, Zlatko Papić, and Dmitry A Abanin. Universal slow growth of entanglement in interacting strongly disordered systems. *Physical review letters*, 110(26):260601, 2013.

[53] Denis M Basko, Igor L Aleiner, and Boris L Altshuler. Metal–insulator transition in a weakly interacting many-electron system with localized single-particle states. *Annals of physics*, 321(5):1126–1205, 2006.

[54] VP Michal, BL Altshuler, and GV Shlyapnikov. Delocalization of weakly interacting bosons in a 1d quasiperiodic potential. *Physical review letters*, 113(4):045304, 2014.

[55] Christian P Chen and Henning Schomerus. Fock-space geometry and strong correlations in many-body localized systems. *Physical Review B*, 104(20):205411, 2021.

[56] Elliott H Lieb and Derek W Robinson. The finite group velocity of quantum spin systems. In *Statistical mechanics*, pages 425–431. Springer, 1972.

[57] Michael A Nielsen and Isaac Chuang. Quantum computation and quantum information, 2002.

[58] Jens H Bardarson, Frank Pollmann, and Joel E Moore. Unbounded growth of entanglement in models of many-body localization. *Physical review letters*, 109(1):017202, 2012.

[59] Anushya Chandran, Isaac H Kim, Guifre Vidal, and Dmitry A Abanin. Constructing local integrals of motion in the many-body localized phase. *Physical Review B*, 91(8):085425, 2015.

[60] Anjan Kundu. Quantum integrable systems: basic concepts and brief overview. *arXiv preprint hep-th/9708114*, 1997.

[61] Anastasia Doikou, Stefano Evangelisti, Giovanni Feverati, and Nikos Karaiskos. Introduction to quantum integrability. *International Journal of Modern Physics A*, 25(17):3307–3351, 2010.

[62] Maksym Serbyn, Michael Knap, Sarang Gopalakrishnan, Zlatko Papić, Norman Ying Yao, Chris R Laumann, Dmitry A Abanin, Mikhail D Lukin, and Eugene A Demler. Interferometric probes of many-body localization. *Physical review letters*, 113(14):147204, 2014.

[63] Yasaman Bahri, Ronen Vosk, Ehud Altman, and Ashvin Vishwanath. Localization and topology protected quantum coherence at the edge of hot matter. *Nature communications*, 6(1):1–6, 2015.

[64] R Vasseur, SA Parameswaran, and JE Moore. Quantum revivals and many-body localization. *Physical Review B*, 91(14):140202, 2015.

[65] Giuseppe De Tomasi, Soumya Bera, Jens H Bardarson, and Frank Pollmann. Quantum mutual information as a probe for many-body localization. *Physical Review Letters*, 118(1):016804, 2017.

[66] Xiao Chen, Tianci Zhou, David A Huse, and Eduardo Fradkin. Out-of-time-order correlations in many-body localized and thermal phases. *Annalen der Physik*, 529(7):1600332, 2017.

[67] Maksym Serbyn and Dmitry A Abanin. Loschmidt echo in many-body localized phases. *Physical Review B*, 96(1):014202, 2017.

[68] Sthitadhi Roy and David E Logan. Fock-space correlations and the origins of many-body localization. *Physical Review B*, 101(13):134202, 2020.

[69] Sthitadhi Roy and David E Logan. Fock-space landscapes across the many-body localisation transition. *arXiv preprint arXiv:2106.09036*, 2021.

[70] Sven Larsson and Vedene H Smith Jr. Analysis of the s 2 ground state of lithium in terms of natural and best overlap (brueckner) spin orbitals with implications for the fermi contact term. *Physical Review*, 178(1):137, 1969.

[71] JM Zhang and Marcus Kollar. Optimal multiconfiguration approximation of an n-fermion wave function. *Physical Review A*, 89(1):012504, 2014.

[72] JM Zhang and Norbert J Mauser. Optimal slater-determinant approximation of fermionic wave functions. *Physical Review A*, 94(3):032513, 2016.

[73] CWJ Beenakker. Random-matrix theory of majorana fermions and topological superconductors. *Reviews of Modern Physics*, 87(3):1037, 2015.

[74] Carlo WJ Beenakker. Random-matrix theory of quantum transport. *Reviews of modern physics*, 69(3):731, 1997.

[75] Fritz Haake, Marek Kus, Hans-Jürgen Sommers, Henning Schomerus, and Karol Zyczkowski. Secular determinants of random unitary matrices. *Journal of Physics A: Mathematical and General*, 29(13):3641, 1996.

[76] Henning Schomerus and Jakub Tworzydło. Quantum-to-classical crossover of quasi-bound states in open quantum systems. *Physical review letters*, 93(15):154102, 2004.

[77] J Tworzydło, A Tajic, H Schomerus, and CWJ Beenakker. Dynamical model for the quantum-to-classical crossover of shot noise. *Physical review B*, 68(11):115313, 2003.

[78] Alexander L Fetter and John Dirk Walecka. *Quantum theory of many-particle systems*. Courier Corporation, 2012.

[79] Felix Andraschko, Tilman Enss, and Jesko Sirker. Purification and many-body localization in cold atomic gases. *Physical review letters*, 113(21):217201, 2014.

[80] Baoming Tang, Deepak Iyer, and Marcos Rigol. Quantum quenches and many-body localization in the thermodynamic limit. *Physical Review B*, 91(16):161109, 2015.

[81] Serge Aubry and Gilles André. Analyticity breaking and anderson localization in incommensurate lattices. *Ann. Israel Phys. Soc*, 3(133):18, 1980.

[82] Shankar Iyer, Vadim Oganesyan, Gil Refael, and David A Huse. Many-body localization in a quasiperiodic system. *Physical Review B*, 87(13):134202, 2013.

[83] Piero Naldesi, Elisa Ercolessi, and Tommaso Roscilde. Detecting a many-body mobility edge with quantum quenches. *SciPost Physics*, 1(1):010, 2016.

[84] F Setiawan, Dong-Ling Deng, and JH Pixley. Transport properties across the many-body localization transition in quasiperiodic and random systems. *Physical Review B*, 96(10):104205, 2017.

[85] Hermann Weyl. *The classical groups: their invariants and representations*, volume 1. Princeton University Press, 1946.

[86] F. Haake, Sven Gnutzmann, and Marek Kuś. *Quantum Signatures of Chaos*. Springer, Berlin, Heidelberg, 4 edition, 2019.

[87] M. L. Mehta. *Random Matrices*. Elsevier Science, Amsterdam, 3 edition, 2004.

[88] Eugene P. Wigner. Characteristic vectors of bordered matrices with infinite dimensions. *Ann. Math.*, 62(3):548–564, 1955.

[89] Freeman J Dyson. The threefold way. algebraic structure of symmetry groups and ensembles in quantum mechanics. *Journal of Mathematical Physics*, 3(6):1199–1215, 1962.

[90] Alexander Altland and Martin R Zirnbauer. Nonstandard symmetry classes in mesoscopic normal-superconducting hybrid structures. *Physical Review B*, 55(2):1142, 1997.

[91] Ching-Kai Chiu, Jeffrey CY Teo, Andreas P Schnyder, and Shinsei Ryu. Classification of topological quantum matter with symmetries. *Reviews of Modern Physics*, 88(3):035005, 2016.

[92] JJM Verbaarschot and I Zahed. Spectral density of the qcd dirac operator near zero virtuality. *Physical Review Letters*, 70(25):3852, 1993.

[93] M Titov, PW Brouwer, A Furusaki, and C Mudry. Fokker-planck equations and density of states in disordered quantum wires. *Physical Review B*, 63(23):235318, 2001.

[94] Freeman J Dyson. The dynamics of a disordered linear chain. *Physical Review*, 92(6):1331, 1953.

[95] PW Brouwer, C Mudry, BD Simons, and A Altland. Delocalization in coupled one-dimensional chains. *Physical review letters*, 81(4):862, 1998.

[96] Yasuhiro Hatsugai, Xiao-Gang Wen, and Mahito Kohmoto. Disordered critical wave functions in random-bond models in two dimensions: Random-lattice fermions at e= 0 without doubling. *Physical review B*, 56(3):1061, 1997.

[97] Shi-Jie Xiong and SN Evangelou. Power-law localization in two and three dimensions with off-diagonal disorder. *Physical Review B*, 64(11):113107, 2001.

[98] M Kappus and Franz Wegner. Anomaly in the band centre of the one-dimensional anderson model. *Zeitschrift für Physik B Condensed Matter*, 45(1):15–21, 1981.

[99] Henning Schomerus and Mikhail Titov. Band-center anomaly of the conductance distribution in one-dimensional anderson localization. *Physical review B*, 67(10):100201, 2003.

[100] Dmitry A Abanin and Zlatko Papić. Recent progress in many-body localization. *Annalen der Physik*, 529(7):1700169, 2017.

[101] Don N Page. Average entropy of a subsystem. *Physical review letters*, 71(9):1291, 1993.

[102] E. P. Wigner. Results and theory of resonance absorption. In *Proceedings of the Conference on Neutron Physics by Time-of-Flight, ORNL-2309*, pages 59–70, Gatlinburg, Tenn, USA, 1956. Academic Press.

[103] Xiao-Gang Wen. *Quantum field theory of many-body systems: from the origin of sound to an origin of light and electrons*. OUP Oxford, 2004.

[104] David A Huse, Rahul Nandkishore, Vadim Oganesyan, Arijeet Pal, and Shivaji L Sondhi. Localization-protected quantum order. *Physical Review B*, 88(1):014206, 2013.

[105] Jonas A Kjäll, Jens H Bardarson, and Frank Pollmann. Many-body localization in a disordered quantum ising chain. *Physical review letters*, 113(10):107204, 2014.

[106] Romain Vasseur, Aaron J Friedman, SA Parameswaran, and Andrew C Potter. Particle-hole symmetry, many-body localization, and topological edge modes. *Physical Review B*, 93(13):134207, 2016.

[107] Giuseppe De Tomasi, Daniele Trapin, Markus Heyl, and Soumya Bera. Anomalous diffusion in particle-hole symmetric many-body localized systems. *arXiv preprint arXiv:2001.04996*, 2020.

[108] Luigi Amico, Rosario Fazio, Andreas Osterloh, and Vlatko Vedral. Entanglement in many-body systems. *Reviews of modern physics*, 80(2):517, 2008.

[109] Nicolas Laflorencie. Scaling of entanglement entropy in the random singlet phase. *Physical review b*, 72(14):140408, 2005.

[110] Ian Affleck, Tom Kennedy, Elliott H Lieb, and Hal Tasaki. Rigorous results on valence-bond ground states in antiferromagnets. In *Condensed Matter Physics and Exactly Soluble Models*, pages 249–252. Springer, 2004.

[111] Heng Fan, Vladimir Korepin, and Vwani Roychowdhury. Entanglement in a valence-bond solid state. *Physical review letters*, 93(22):227203, 2004.

[112] Zhibing Li, Yimin Liu, Wei Zheng, and Chengguang Bao. Entanglement entropy of the spin-1 condensates at zero temperature. *Entropy*, 20(1):80, 2018.

[113] Luca D'Alessio, Yariv Kafri, Anatoli Polkovnikov, and Marcos Rigol. From quantum chaos and eigenstate thermalization to statistical mechanics and thermodynamics. *Advances in Physics*, 65(3):239–362, 2016.

[114] Fausto Borgonovi, Felix M Izrailev, Lea F Santos, and Vladimir G Zelevinsky. Quantum chaos and thermalization in isolated systems of interacting particles. *Physics Reports*, 626:1–58, 2016.

[115] Igor V Gornyi, Alexander D Mirlin, and Dmitry G Polyakov. Interacting electrons in disordered wires: Anderson localization and low-t transport. *Physical review letters*, 95(20):206603, 2005.

[116] Bela Bauer and Chetan Nayak. Area laws in a many-body localized state and its implications for topological order. *Journal of Statistical Mechanics: Theory and Experiment*, 2013(09):P09005, 2013.

[117] Henrik P Lüschen, Pranjal Bordia, Sean S Hodgman, Michael Schreiber, Saubhik Sarkar, Andrew J Daley, Mark H Fischer, Ehud Altman, Immanuel Bloch, and Ulrich Schneider. Signatures of many-body localization in a controlled open quantum system. *Physical Review X*, 7(1):011034, 2017.

[118] Xiansong Xu, Chu Guo, and Dario Poletti. Interplay of interaction and disorder in the steady state of an open quantum system. *Physical Review B*, 97(14):140201, 2018.

[119] M-T Rieder, Lukas M Sieberer, Mark H Fischer, and Ion C Fulga. Localization counteracts decoherence in noisy floquet topological chains. *Physical review letters*, 120(21):216801, 2018.

[120] J Marino and RM Nandkishore. Many-body localization proximity effects in platforms of coupled spins and bosons. *Physical Review B*, 97(5):054201, 2018.

[121] I Vakulchyk, I Yusipov, M Ivanchenko, Sergej Flach, and S Denisov. Signatures of many-body localization in steady states of open quantum systems. *Physical Review B*, 98(2):020202, 2018.

[122] A Degasperis, L Fonda, and GC Ghirardi. Does the lifetime of an unstable system depend on the measuring apparatus? *Il Nuovo Cimento A (1965-1970)*, 21(3):471–484, 1974.

[123] Baidyanath Misra and EC George Sudarshan. The zeno's paradox in quantum theory. *Journal of Mathematical Physics*, 18(4):756–763, 1977.

[124] Asher Peres. Zeno paradox in quantum theory. *American Journal of Physics*, 48(11):931–932, 1980.

[125] Adam Nahum, Jonathan Ruhman, Sagar Vijay, and Jeongwan Haah. Quantum entanglement growth under random unitary dynamics. *Physical Review X*, 7(3):031016, 2017.

[126] CW Von Keyserlingk, Tibor Rakovszky, Frank Pollmann, and Shivaji Lal Sondhi. Operator hydrodynamics, otocs, and entanglement growth in systems without conservation laws. *Physical Review X*, 8(2):021013, 2018.

[127] Adam Nahum, Sagar Vijay, and Jeongwan Haah. Operator spreading in random unitary circuits. *Physical Review X*, 8(2):021014, 2018.

[128] Kurt Jacobs. *Quantum measurement theory and its applications*. Cambridge University Press, 2014.

[129] Asher Peres. *Quantum theory: concepts and methods*. Springer, 2002.

[130] Todd A Brun. A simple model of quantum trajectories. *American Journal of Physics*, 70(7):719–737, 2002.

[131] Andrew N Jordan and Alexander N Korotkov. Qubit feedback and control with kicked quantum nondemolition measurements: A quantum bayesian analysis. *Physical Review B*, 74(8):085307, 2006.

[132] Marcin Szyniszewski, Alessandro Romito, and Henning Schomerus. Entanglement transition from variable-strength weak measurements. *Physical Review B*, 100(6):064204, 2019.

[133] Marcin Szyniszewski, Alessandro Romito, and Henning Schomerus. Universality of entanglement transitions from stroboscopic to continuous measurements. *Physical review letters*, 125(21):210602, 2020.

[134] John Wishart. The generalised product moment distribution in samples from a normal multivariate population. *Biometrika*, pages 32–52, 1928.

[135] YY Atas, Eugene Bogomolny, O Giraud, and G Roux. Distribution of the ratio of consecutive level spacings in random matrix ensembles. *Physical review letters*, 110(8):084101, 2013.